Model Analysis of Plasma-Surface Interactions during Silicon Oxide Etching in Fluorocarbon Plasmas

Hiroshi Fukumoto

2012

Abstract

This thesis presents analyses of silicon oxide etching in fluorocarbon plasmas. The silicon oxide etching by using fluorocarbon plasmas are difficult to be controlled owing to a number of reactions concerned in the processes. The two models have been developed for a plasma gas phase domain and a plasma-surface interface domain. The former or macroscopic model consists of a inductively coupled CF_4 plasma source, gas-phase reactions in the chamber, reactions between plasma and substrate surfaces or chamber wall, taking into account transport of ions and radicals. The latter or microscopic model consists of particle transport inside microstructure and surface reactions. The microscopic model clarifies effects of pattern geometries on etching profiles and potential distribution in the microstructure by calculating from fluxes of chemical species and electrons in the plasma.

Fluorocarbon plasmas are employed for etching of silicon oxide insulating layers. This plasma-surface combination generates a number of species consisting of carbon, oxygen, fluorine, and silicon through the plasma-surface interactions. Therefore, identification of species to contribute to etching promotion or inhibition is significantly important. The macroscopic model contains not only gas-phase reactions, but also reactions between plasma and surfaces, and succeeded to clarify two-dimensional distributions of etch products in a chamber. On the other hand, the microscopic plasma-surface interaction model has been developed focusing on pattern geometries of a hole and a trench. The results obtained from the model analysis are effective for the other chemical combinations of plasma gases and etched materials.

This thesis consists of five chapters. In Chapter 1, the requirements for the plasma etching technology in the fabrication of advanced ultralarge-scale integrated (ULSI) devices are presented. The plasma-surface interactions are then explained along with their effects on the formation of undesired profile irregularities. The scope of this thesis is given after introducing the previous studies of the SiO_2 etching by using fluorocarbon plasmas.

In Chapter 2, a two-dimensional fluid model has been developed to study plasma chemical

behavior of etch products as well as reactants during SiO_2 etching by using inductively coupled CF_4 plasmas. The plasma fluid model consisted of Maxwell's equations, continuity equations for neutral and charged species including gas-phase and surface reactions, and energy balance equations for electrons. The surface reaction model assumed Langumiur adsorption kinetics with the coverage of fluorine atoms, fluorocarbon radicals, and polymers on SiO_2 surfaces. Numerical results indicated that etch product species occupy a significant fraction of reactive ions as well as neutrals in the reactor chamber during etching, which in turn led to a change of plasma and surface chemistry underlying the processing. In practice, the density of SiF_4 was typically about 10% of that of the feedstock CF_4, being comparable to that of the most abundant fluorocarbon radical CF_2; moreover, the density of SiF_3^+ was typically about 5% of that of the most abundant fluorocarbon ion CF_3^+. The density and the distribution of such product species in the reactor chamber were changed by varying the ion bombardment energy on substrate surfaces, gas pressure, mass flow rate, and coil configuration, which arose in part from gas-phase reactions depending on plasma electron density and temperature. Surface reactions on the chamber walls and on substrate also affected the product density and distribution in the reactor; in particular, the surface reactions on the SiO_2 dielectric window as well as substrate surfaces were found to largely affect the product density and distribution.

In Chapter 3, two-dimensional etching profile evolution in two different geometries, namely an axisymmetric hole and an infinitely long trench, has been simulated with the cellular algorithm, to clarify the effects of geometrically different structures on etching profile evolution. The simulation assumed SiO_2 etching using CF_4 plasmas, owing to the widely employed fluorocarbon plasmas for the fabrication of contact and via holes. Numerical results indicated that the two mask pattern geometries gave some differences in profile evolution, depending on condition parameters such as ion energy, mask pattern size, mask height, and reflection probability on mask surfaces. The profile evolution was slower and more anisotropic in a hole than in a trench; in practice, the profile of a trench tended to have prominent lateral etches such as an undercut and a bowing on sidewalls. Moreover, the reactive ion etching lag was less significant for a hole than for a trench. These differences were ascribed to the geometrical shadowing effects of the structure for neutrals, where the incident flux of neutrals was more significantly reduced in a hole than in a trench. The differences were also attributed to the anisotropy of the velocity distribution of neutrals; in effect, the velocity distribution was more anisotropic in a hole, be-

cause more particles interact with mask sidewalls to adsorb or reflect thereon in a hole, so that more anisotropic neutrals were transported onto bottom surfaces after passing mask features.

In Chapter 4, the effects of mask pattern geometry on potential distribution and ion trajectories were investigated on the basis of the previous etching profile model described in Chapter 3, incorporating surface charge continuity and Poisson's equation. Two geometrical mask patterns of a hole and a trench were considered to clarify the effects of geometrically different structures on potential distribution and ion trajectories. Charging effects and the resulting potential changed flux of ions and electrons incident to surfaces. Ion flux incident to the structure bottom were significantly reduced under charging condition compared to the ion flux under the non-charging condition. Moreover, numerical results showed that the difference of potential distribution inside the structure between the hole and trench; the potential drop at the structure bottom was observed in the trench, while no significant potential drop was observed in the hole. The potential difference derived from mask pattern geometry also changed ion trajectories. The results indicates that etched feature profile is affected by mask pattern geometry.

Chapter 5 concludes this study.

Acknowledgment

I would like to express my gratitude to all people who have supported this thesis in Propulsion Engineering Laboratory, Department of Aeronautics and Astronautics, Kyoto University for five years from April, 2004 to March, 2009 and additional three years.

First of all, I am deeply grateful to my supervisor, Prof. Kouichi Ono, for his patience and advices providing me with knowledge in the area of plasma processing. In particular, his support to train me for my English writing skills has been most precious. I would also like to thank Prof. Kazuo Aoki and Prof. Takaji Inamuro for their careful review of this thesis and valuable comments.

I gratefully acknowledge Associate Prof. Koji Eriguchi and Project Scientist Hiroaki Ohta at University of California, Santa Barbara (the former assistance professor) for giving me useful knowledge and valuable suggestions on my research. I am again grateful to Prof. Yuichi Setsuhara at Osaka University (the former associate professor) and Associate Prof. Kazuo Takahashi at Kyoto Institute of Technology (the former assistance professor) for teaching me basic manner and knowledge for my earlier research.

It would not have been possible to write this thesis without member in the laboratory. In particular, thanks must go to Dr. Hiroyuki Kousaka, Dr. Yugo Osano, Dr. Yoshinori Takao, Mr. Isao Fujikake, Mr. Keisuke Nakamura, Mr. Naoki Kusaba, Mr. Tomohiro Kitagawa, Mr. Norifumi Hamaya, Mr. Shousei Hou, Mr. Kazushi Osari, Mr. Masahito Mori, and Mr. Masayuki Kamei for giving me fruitful advices and nice experiences, and Dr. Takeshi Takahashi for his preparation of my computing environment.

Finally, I would like to thank again all persons who advised me, supported me, and cheered me up in my each research stage.

Contents

Chapter 1

Introduction

1.1 Semiconductor industries and plasma etching

The semiconductor device industry is a fast-growing and fundamental industry. The driving principle of the growing semiconductor industry has been Moore's law, which was proposed by Gordon Moore in 1965 [1]; it is stated as follows: the number of transistors and resistors on an IC chip doubles every 18 months. Moore's law has been realized by technology innovations aimed at increasing the number of components on a miniaturized chip. International Technology Roadmap for Semiconductor (ITRS) gives views that these technology innovations typically involve scaling-down of the technology node, as shown in Fig. 1.1 [2]; in this figure, the half-pitches of the dynamic random access memory (DRAM), micro-processing unit (MPU), and application specific integrated circuit (ASIC) is shown as a function of the year.

All products involving large scale integration (LSI) and also some compound semiconductor devices are manufactured by utilizing core plasma processes such as plasma etching technology and plasma ashing technology. The capabilities of plasma processes were first demonstrated by the oxygen plasma ashing of a polymer-based photoresist film by Irving in 1968 [3, 4]. In 1971, he disclosed experimental data pertaining to the plasma etching of silicon using CF_4 plasma [5]. In the early 1970s, both O_2 plasma ashing technology and plasma isotropic etching technology were successfully used to manufacture a 16K DRAM based on a 5 mm node [6–9]. As the first industrial application of isotropic etching, 13.56 MHz rf discharge plasma in a barrel-type

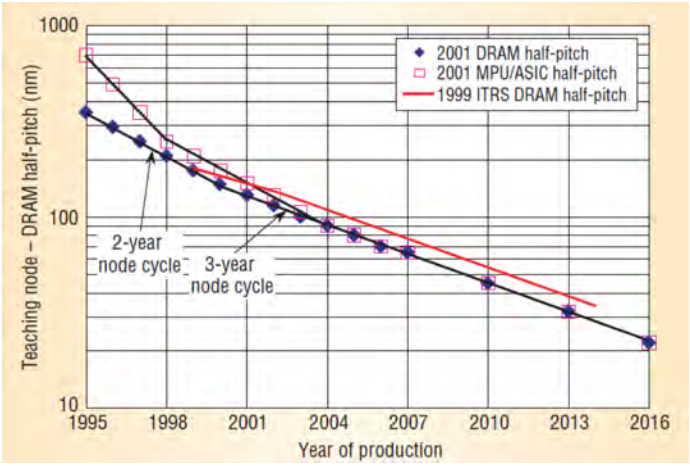

Fig. 1.1: 2001 ITRS Roadmap of DRAM half-pich and MPU/ASIC half-pich [2].

chamber with CF_4 or CF_4/O_2 gas was applied to remove silicon nitride films to form a local oxidation of silicon (LOCOS) isolation structure. Plasma stripping of the masking photoresist film was also applied in this manufacturing process. The successful application of plasma etching as well as plasma ashing technologies induced drastic changes in the manufacturing process of LSIs from the conventional liquid-based wet processes within a fairly short period. These changes reduced the number of steps in the manufacturing process and clearly enhanced the chip yields, therefore the changes reduced the manufacturing cost of the devices.

There are two main methods of etching used in the semiconductor industry: wet etching, and dry or plasma etching. In the early days of the industry, wet etching was used exclusively. It was well-established, simple, and inexpensive technology. Wet etching can also be very selective. Eventually, however, the need for smaller line widths and more vertical structures required new techniques. Plasma etching methods were developed for integrated circuit fabrication and are used for most etching steps today.

The significant disadvantages of wet etching are as follows: (1) poor accuracy of the etched patterns due to inherent undercutting, (2) poor stability and reproducibility of the etching process because of the difficulty in controlling the chemical composition during hot processing, (3) the danger involved in handling during the wet etching and stripping processes, (4) waste chemicals are a serious issue from the viewpoint of pollution, (5) wet processes are handled manually by operators, and this causes a strong dependence of the pattern yield on an operator's skills, (6) wet processes are difficult to automate, and (7) the total cost of wet processes is high [10].

The plasma etching process has played a key role in integrated circuit manufacture for many years, and it becomes even more important nowadays as we enter the era of ultra-large scale integration (ULSI). However, the low etch rate and profile irregularities of the small features were found to depend on the structure geometry and process conditions. The etch rate dependence on the feature size results in the necessity to do some, sometimes significant, overetching to achieve equal depths of the features with different sizes. This in turn increases the cost of manufacturing and makes the chips vulnerable to damage due to overetching or failure to clear. Deviations from the desired profile can also lead to considerable yield reduction. As a result the dependence of the etch rate and profile on both the feature size and the process conditions has been widely discussed in the literature [11–19] and several attempts have been made to develop the models of the etching process [13–15, 18, 19].

1.2 Plasma generation

Discharges excited and sustained by high-frequency electromagnetic fields are of increasing interest for technical and industrial applications. The power absorption P_{abs} per volume V by a plasma in a high-frequency field is given by [20–22]

$$\frac{P_{\text{abs}}}{V} = \frac{1}{2} n_{\text{e}} \frac{e^2}{m_{\text{e}} \nu} \frac{\nu^2}{\nu^2 + \omega^2} E_0^2, \tag{1.1}$$

where n_{e} is the electron density, e and m_{e} are the electron charge and mass, ν is the electron-neutral collision frequency, and ω refers to the angular frequency of the electromagnetic field whose amplitude is E_0.

Rf discharges are usually operated in the frequency range $f = \omega/2\pi \simeq 1{-}100$ MHz. The corresponding wavelengths ($\lambda = 300{-}3$ m) are large compared to the dimensions of the plasma reactor. For microwaves the most commonly used wavelength is 12.24 cm, corresponding to a frequency of 2.45 GHz. This wavelength is roughly comparable to the dimensions of a typical microwave reactor. For lower frequencies, the ions accelerated in the field move towards the electrodes and produce secondary electrons, similar to what happens in a dc discharge. As the frequency increases, the ions and subsequently also the electrons can no longer reach the electrode surface during the acceleration phase of the exciting external field. Capacitively coupled discharges will be discussed first, followed by high-density plasmas such as electron cyclotron

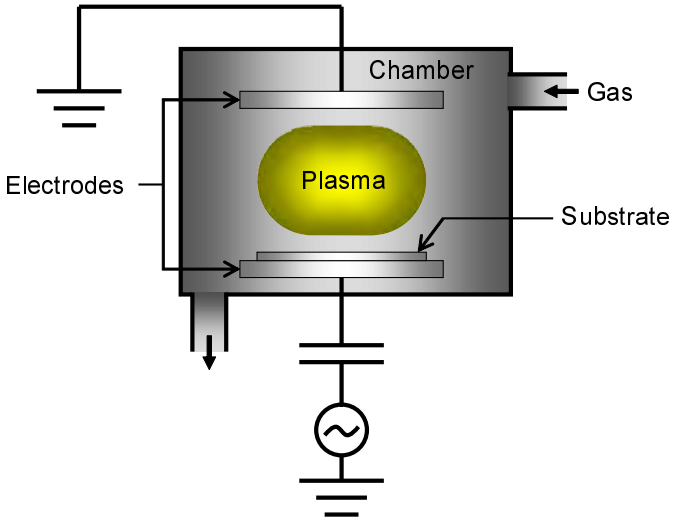

Fig. 1.2: Schematic of a CCP plasma reactor.

resonance (ECR) plasma and inductively coupled plasma (ICP).

1.2.1 Capacitively coupled plasmas (CCP)

The vessel of a capacitively coupled discharge [23–28] may have interior circular disc-shaped parallel electrodes which are separated by a distance of a few centi meters as shown in Fig. 1.2. The electrodes may be in contact with the discharge or they be insulated from discharge by a dielectric. Gas pressures are typically in the range $1-10^3$ Pa ($7.5-7.5 \times 10^3$ mTorr). A conventional rf system for sustaining a discharge consists of a generator, usually combined with an impedance matching network, and the reactor with the electrodes. The generator type has to be licensed in terms of the frequency band for commercial use. The electrodes in the rf discharge are covered by sheath regions, which are similar to the cathode dark space in a dc glow discharge. The space between the electrodes is filled with the bulk plasma.

In a capacitively coupled rf discharge, the electron density is in the range $n_e = 10^9$–10^{10} cm^{-3} and densities of up to 10^{11} cm^{-3} are possible at higher frequencies [29]. The ion energy near the powered electrode can reach energies of a few hundred electron-volts due to the self-bias. Such discharges are successfully applied to thin-film deposition and plasma etching as well as to the sputtering of insulating materials.

1.2.2 Electron cyclotron resonance (ECR) plasmas

Plasma generation using microwaves is widely employed in many applications [22, 30–35]. Characteristic features of microwaves are the wavelength, which is comparable to the dimensions of the plasma apparatus (2.45 GHz: $\lambda = 12.24$ cm), and the short period of the exciting microwave field. The amplitude of the oscillations of the electrons in the microwave field is very small. For an excitation frequency $f = 2.45$ GHz and an amplitude $E_0 = 500$ V cm^{-1}, it is 3.5×10^{-3} cm. The power absorption (eq. (1.1)) depends on the electron-neutral collision frequency, i.e. on the gas pressure and the gas composition. The absorption efficiency in a 2.45 GHz discharge is high for He in the region between 10^3 and 10^4 Pa (7.5×10^3 and 7.5×10^4 mTorr), whereas the maximum efficiency for Ar is reached for 200 Pa (1.5×10^3 mTorr) [36]. However, microwave discharges can be operated at higher pressures as well, even at atmospheric pressure. The corresponding cut-off density of the electrons at 2.45 GHz is about 10^{11} cm^{-3}. Waves of this frequency can penetrate into plasmas with higher densities only up to the thickness of the skin sheath, which equals a few centimeters under these conditions. The microwave power absorption inside the skin sheath transfers energy into the plasma via waves with a frequency below the cut-off frequency. A microwave plasma reactor consists in principle of a microwave power supply, a circulator, the applicator, and the plasma load. The transmission lines are rectangular waveguides or, at lower powers, coaxial cables. The applicator should optimize the energy transfer into the plasma and minimize the power reflection. The circulator protects the power supply from reflected power.

An ECR plasma is a typical example of a microwave plasma in magnetic fields. Figure 1.3 shows a schematic of an ECR plasma reactor. The discharge tube is located at the point of maximum electric field, the distance between tube and stubs is $\lambda/4$. This principle can also be used for the excitation of rf plasmas. The excitation of surface waves [31] is another way of generating plasmas by microwaves. The surface wave propagates along the boundary between the plasma column and the dielectric vessel. The wave energy is absorbed by the plasma. A technical application of this type of plasma excitation is realized in a surfatron.

ECR plasmas have often been used for material processing, because it enables production of high-electron-temperature and low-ion-temperature plasma at low gas pressures. In many cases, some magnetic coils are used to generate the magnetic field (875 gauss for 2.45 GHz) for ECR [37–41]. The cost of the magnet system becomes quite high when we generate an

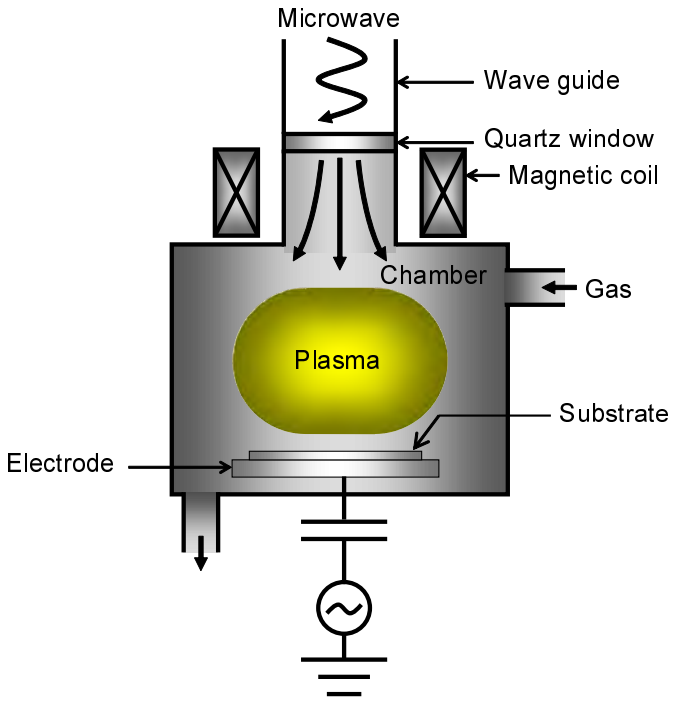

Fig. 1.3: Schematic of an ECR plasma reactor.

ECR plasma of large diameter. The surface magnetic fields are easily obtained by permanent magnets, and they are useful for plasma production by ECR and also for plasma confinement. Among the various arrangements of permanent magnets, the multi-ring-cusp-type field is expected to show high performance because of the closed orbit of the electron drift motion.

1.2.3 Inductively coupled plasmas (ICP)

An ICP [23,24,42] is excited by an electric field generated by a transformer from a rf current in a conductor. The changing magnetic field of this conductor induces an electric field in which the plasma electrons are accelerated. A typical example of ICP reactor and a photograph of plasma generated in an ICP plasma reactor are shown in Figs. 1.4 and 1.5, respectively. The current-carrying coil or wire can either be outside or inside the plasma volume. ICPs can achieve high electron densities ($n_e = 10^{12}$ cm^{-3}) at low ion energies. Several applications are reported such as thin-film deposition, plasma etching, and ion sources in mass spectrometric analysis [43].

ICP etching offers an attractive alternative dry etching technique. The general belief is that ICP sources are easier to scale up than ECR plasma sources, and are more economical in terms

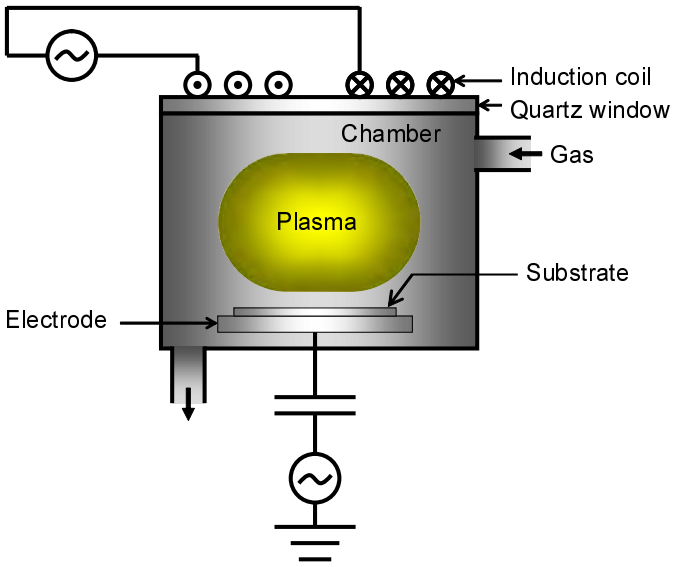

Fig. 1.4: Schematic of an ICP plasma reactor.

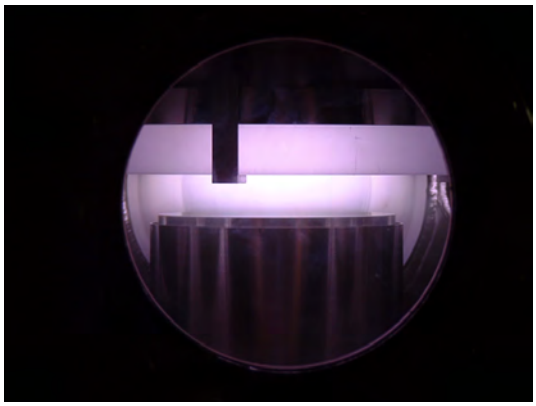

Fig. 1.5: A photograph of plasma generated in an ICP plasma reactor.

of cost and power requirements. ICP plasmas are formed in a dielectric vessel encircled by an inductive coil into which rf power is applied. A strong magnetic field is induced in the center of the chamber which generates a high-density plasma due to the circular region of the electric field that exists concentric to the coil. At low pressures ($\leq$ 10 mTorr), the plasma diffuses from the generation region and drifts to the substrate at relatively low ion energy. Thus, ICP etching is expected to produce low damage while achieving high etch rates. Anisotropic profiles are obtained by superimposing an rf bias on the sample to independently control ion energy.

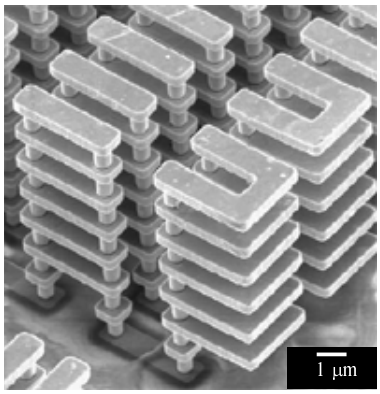

Fig. 1.6: An SEM micrograph of multi-layer metal interconnect structure of Cu dual damascene process [44].

1.3 Fluorocarbon plasma and SiO_2 etching

Silicon oxide (SiO_2) is employed for insulating films between wirings or between wirings and devices. Figure 1.6 shows of an image of multi-layer metal interconnect structure of Cu dual damascene process by using a scanning electron microscope (SEM) [44]. As damascene processes spreads in the formation of a multilayer wiring structure and wiring in semiconductor devices, the number of process steps of SiO_2 etching continues to increase in the future. Diffusion layer and the polycrystalline Si gate electrode formed in the Si substrate has been placed under the SiO_2 layer. This configuration is a typical example of high aspect ratio etching, therefore SiO_2 is required to be etched at high selectivity against Si substrate or polycrystalline Si.

The highly selective etching of SiO_2 against Si requires fluorocarbon etching gases such as CF_4, CHF_3, C_2F_6, and C_4F_8, and additive gases such as H_2, CO, CO_2, and Ar. The possible mechanism of the selective etching is attributed to the competition between etching reaction of F atoms on the surface of SiO_2 and Si, and deposition of fluorocarbon polymer consisting of CF and CF_2 radicals. However, the detailed mechanism of ion-assisted reaction in SiO_2 etching by fluorocarbon plasma is not well understood owing to complexity of competition of polymer film deposition from CF_x ($x = 1-3$) radicals and ion etching from CF_x^+ ($x = 1-3$) ions.

Plasma etching involves the ionization of chemical gas into ions and neutrals. For silicon oxide (SiO_2) etching, the initial gas is usually a carbon fluorine molecule such as carbon tetraflouride (CF_4). The ionized plasma within the chamber is accelerated towards the wafer holding chuck through the rf bias on the chuck which creates a strong electric field with the

plasma. The ions pick up most of their energy when they enter the sheath and are accelerated by the electric field. The neutrals diffuses from the plasma through the sheath towards the wafer and the chamber walls.

Rf discharges in low-pressure fluorocarbon gases are widely used for the etching of SiO_2 layers in microelectronics circuit fabrication. By careful adjustment of the gas composition (using mixtures of CF_4, H_2, CHF_3, C_2F_6, C_4F_8, *etc.*), it is possible to etch sub-micron features in SiO_2 with vertical side-walls and without etching the underlying silicon. This etch selectivity occurs due to the selective formation of a protective fluorocarbon polymer film on the Si surface. A number of studies have stressed the importance of CF_x radicals in the polymer deposition process. In particular, numerous groups have reported a strong correlation between the gas-phase CF_2 radical concentration and the polymer deposition rate (and thus to the etch selectivity) [45–51]. It has therefore been suggested that the film is formed simply by the sticking of CF_2 radicals on the silicon surface, forming a polytetrafluoroethylene (PTFE)-like $(CF_2)_n$ film [45, 52]. However, several other neutral molecules (for example CF [53], CF_3 [54], C_2F_5 [54] and C_4F_2 [53]) have also been proposed as the polymer precursors. In general, conditions which give high selectivity and polymer deposition rate always coincide with low fluorine atom concentration and high CF_x radical concentrations.

It is thus desirable to monitor and control the CF_x radical concentration in the gas phase to optimize the etching process, and this has stimulated numerous studies of the CF_x radical kinetics. Several studies have shown the importance of reactor wall catalyzed processes for CF_x radical destruction [55–58], and recently use has been made of the effect of varying the reactor wall temperature and chemical composition (e.g. using a hot silicon wall) on the gas chemistry and thus the etch characteristics.

Models of fluorocarbon plasma chemistry have generally assumed that CF_x radicals are only produced by electron-impact induced dissociation of the fluorocarbon feedstock gas [59–67], either directly or by sequential fragmentation. However, several studies in capacitively-coupled plasmas [47, 56, 68–75] have indicated that the CF_2 concentration is often maximal at, or close to, the powered electrode, suggesting a surface production mechanism. This phenomenon leads to observed CF_x radical concentrations that are orders of magnitude higher than those predicted by models.

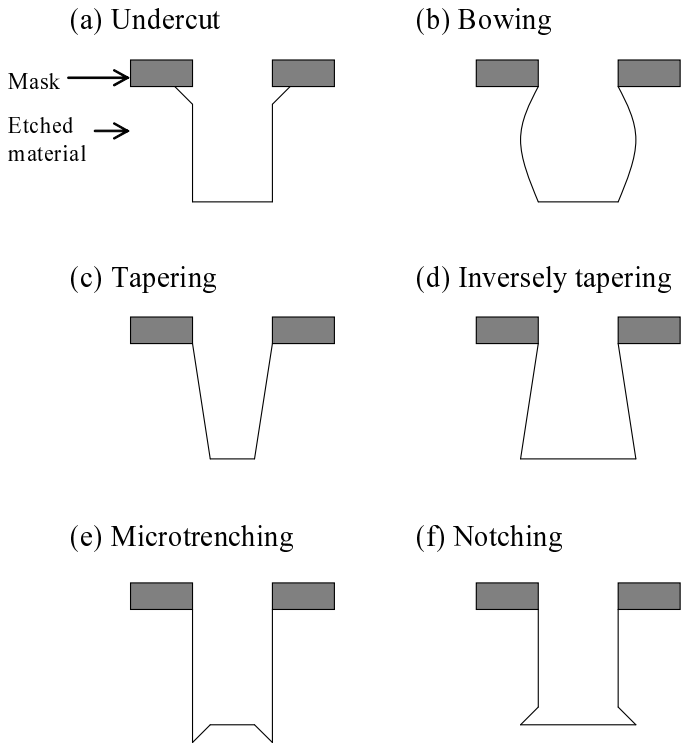

Fig. 1.7: Irregular etched profiles.

1.4 Etching profile irregularities

As illustrated in Figs. 1.7(a)−1.7(f), however, the complex plasma-surface interactions also cause undesired profile irregularities, such as undercutting, sidewall bowing, sidewall tapering, microtrenching, and notching. There are general assumptions to explain the mechanisms for the formation of these feature irregularities as follows. The lateral etching or undercutting beneath the mask is enhanced by spontaneous chemical etching at higher substrate temperatures [76]. In contrast, surface oxidation and inhibitor deposition suppress the lateral etching, resulting in sidewall tapering. The energetic ions reflected from feature sidewalls cause the etching to be enhanced at the corner of the feature bottom, resulting in microtrenches thereat. The microstructural feature surfaces of insulating materials are differentially charged up, owing to the difference in angular distribution of ions and electrons incident onto substrates [77, 78]. This surface charging leads to etch profile distortion, because the trajectory of incoming charged ions are deflected by the Coulomb force. In practice, the ions attracted by the negative charging on insulating mask surfaces enhance the formation of microtrenches at the corner of the feature

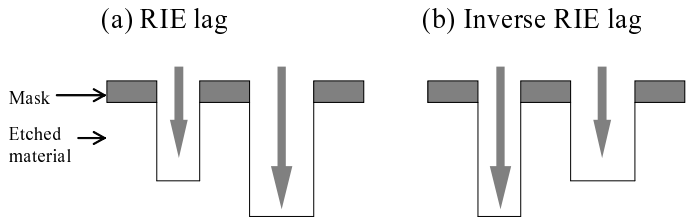

Fig. 1.8: Microscopic ununiformity in etch rate.

bottom [79]; on the other hand, the ions deflected by the positive charging on insulating SiO_2 films underlying Si enhance the notching during overetch step for gate electrode etching [80]. The geometrical shadowing for ions and neutrals cause microscopically non-uniform etch rate, which is usually enhanced for features of higher aspect ratios [81]. The dependence of etch rate on the feature geometry is referred to as a reactive ion etching (RIE) lag and microloading [82]. In contrast, the etch rate is reduced for lower aspect ratio features or wider space patterns in the presence of oxygen or etch inhibitor, being called an inverse RIE lag [81]. Figures 1.8(a) and 1.8(b) illustrate schematic of a RIE lag and inverse RIE lag, respectively. Moreover, there are profile irregularities which rely on aspect ratio of features. In practical etching processes, it is still difficult to suppress these feature irregularities because they are caused by the complex plasma-surface interactions.

1.5 Charging damage

1.5.1 The origin of differential charging

The mechanism that allows one to successfully explain both the decrease in SiO_2 etch rate with increasing aspect ratio and the microtrenching phenomenon is differential charging [14]. Differential charging has been proposed to occur as a result of the difference in angular distribution for ions and electrons. The ion angular distribution is highly anisotropic, whereas the electron angular distribution is nearly isotropic. On microscopic features electrons will mainly arrive at the surface portions near the top of the feature, and are prevented from reaching the bottom, whereas ions will reach the bottom of the feature. This differential charging produces local electric fields inside the feature, which will lead to changes in ion and electron trajectories un-

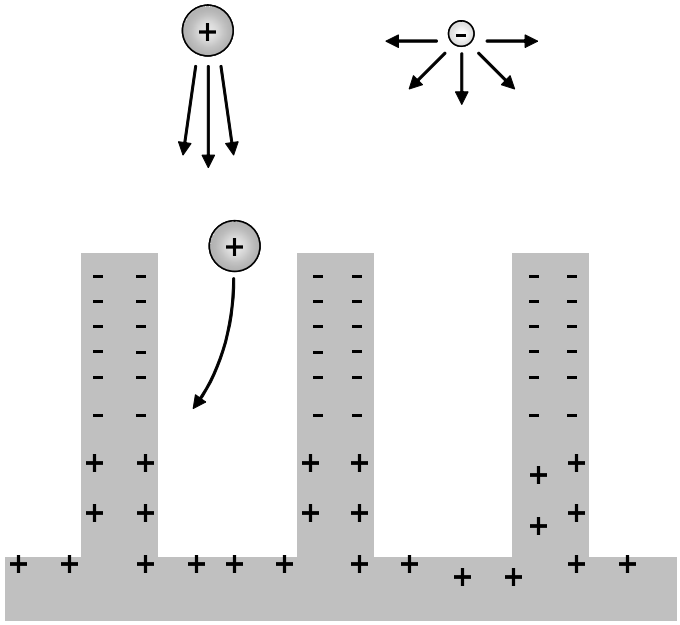

Fig. 1.9: Schematic cross section of insulating microstructures, which shows the mechanism of differential charging with anisotropic ion and isotropic electron incidents.

til electron and ion currents eventually are balanced everywhere along the surface as shown in Fig. 1.9. Surface discharge mechanisms have also been suggested to play a role in the balancing of ion and electron currents [83]. As a result of the suggested differential charging effect, the ion flux to the bottom of features is reduced. This mechanism could therefore explain the decrease in SiO_2 etch rate with increasing aspect ratio. Further, in the differential charging mechanism microtrenching can directly result from ion deflection by negatively charged sidewalls. Differential charging is an important effect in microstructure fabrication using high-density plasmas and could be an important root cause for other microstructure etching phenomena, such as the decrease in the etch rate with increasing aspect ratio [11, 16].

Plasma-induced charging damage exemplifies a formidable challenge that lies ahead as critical dimensions break the 0.25-μm barrier (transistor gate length) and gate-oxides become thinner ($\leq$ 5 nm). Charging damage during plasma etching manifests itself in at least two forms: a) sidewall profile irregularities, such as notching [84, 85] and sidewall bowing, which are readily observable by scanning electron microscopy, and b) electrical degradation and/or breakdown of thin gate-oxides [86–88], induced by tunneling current injection. The latent nature of the latter form of damage is particularly aggravating, requiring special on-wafer charge monitors to

detect its occurrence and, thus, avoid further processing of the damaged wafer. The literature abounds with conflicting reports on how charging damage occurs and what is the influence of various plasma parameters [88]. Some of the confusion originates in the separation between the *observable* and *latent* forms of damage, in spite of their common origin in pattern-dependent charging. Indeed, notching is usually studied in line-and-space (L&S) patterns formed on thick ($\geq$ 100 nm) oxide [84,85], where electron tunneling barely occurs; likewise, tunneling damage is studied in antenna structures, where notching is seldom seen [87]. However, both effects can occur simultaneously in L&S patterns, provided that thin gate oxides are used to facilitate electron tunneling; then, tunneling currents can even help reduce notching. To establish a common nomenclature, we propose to define as charging damage any undesirable effect of pattern-dependent charging, occurring during plasma processing.

Generally, charging damage is a result of differential microstructure charging brought about by the directionality difference between ions and electrons at the wafer [80, 85, 87, 89]. There seems to be some confusion in the literature about what the angular distributions of ions and electrons at the wafer are like, so we shall discuss them in detail.

1.5.2 Charging reduction methodology

Notching can be reduced by decreasing the energy and/or flux of the deflected ions to the sidewalls. Sidewall passivation or changes in the etch chemistry can also be employed, but these methods effectively increase the energy threshold for etching [80]. The root of the problems is the differential charging of the microstructure and only by attacking it notching can be completely eliminated. Making the electron angular distribution more anisotropic would prevent sidewall charging, while it would also neutralize very effectively the bottom surface potentials. This approach is, however, not compatible with continuous plasma operation. Broadening the ion angular distribution is also, obviously, not an option, although it could effectively decrease sidewall charging. Given the existence of the positive sheath and the difference between the ion and electron anisotropies, how can surface charging be reduced?

A significant reduction in charging damage has been reported when etching in pulsed plasmas [90–92]. The neutralization in charging potentials implied by these improvements has been attributed to the lower sheath potential in the afterglow [90], negative ions [91], more directional electrons in the afterglow [92], less anisotropic ions in the afterglow [93,94] more electrons than

ions in the early stages of the active glow [95], more electrons than ions in the late stages of the after glow [94, 96], just to mention a few of the proposed mechanisms. The apparent controversy suggests gaps in the understanding of sheath dynamics in pulsed plasmas; the reader is referred to a companion article [97], where the reduction in differential microstructure charging by pulsing the plasma is further elucidated upon and a new theory is set forth that consistently explains the results.

1.6 Structure of the thesis

This thesis integrates the macroscopic and microscopic studies of SiO_2 etching by using CF_4 plasma described in the following chapters.

Chapter 2 describes that a two-dimensional fluid model has been developed to study plasma chemical behavior of etch products as well as reactants during inductively coupled CF_4 plasma etching of SiO_2. The plasma fluid model consists of Maxwell's equations, continuity equations for neutral and charged species including gas-phase and surface reactions and an energy balance equation for electrons. Etched products from the substrates to the gas phase is focused on this model. In particular, the dependence on ion bombardment energy, gas pressure, mass flow rate, and coil configuration was investigated.

Chapter 3 describes two-dimensional etching profile evolution in an axisymmetric hole and an infinitely long trench has been simulated with the cellular algorithm, to clarify the effects of geometrically different structures on etching profile evolution. The simulation assumed SiO_2 etching using CF_4 plasmas, owing to the widely employed fluorocarbon plasmas for the fabrication of contact and via holes.

Chapter 4 describes effects of mask pattern geometry on potential distribution and ion trajectories based on the etching profile simulation model with Poisson's equation. Two geometrical mask patterns of a hole and a trench is considered to clarify the effects of geometrically different structures on potential distribution and ion trajectories. The simulation assumed SiO_2 etching using CF_4 plasmas, owing to the widely employed fluorocarbon plasmas for the fabrication of contact and via holes.

Chapter 5 concludes this study and discusses recommendation for future work.

References

[1] G. E. Moore: Electronics **38** (1965) 114.

[2] A. Allan, D. Edenfeld, W. H. Joyner Jr., A. B. Kahng, M. Rodgers, and Y. Zorian: Computer **35** (2002) 35.

[3] S. M. Irving: Proc. Kodak Photoresist Seminar 2, 1968, p. 26.

[4] S. M. Irving: Solid State Technol. **14** (1971) 47.

[5] S. M. Irving: U.S. Patent 3615956 (1971).

[6] S. Uematsu, H. Abe, and A. Nara: Mitsubishi Denki Giho **45** (1971) 740 [in Japanese].

[7] H. Abe, H. Matsui, K. Demizu, and H. Komiya: Jpn. J. Appl. Phys. **12** (1973) 767.

[8] H. Komiya, H. Abe, Y. Sonobe, and H. Matsui: IEDM Tech. Dig., 1973, p. 459.

[9] H. Abe, Y. Sonobe, and T. Enomoto: Jpn. J. Appl. Phys. **12** (1973) 154.

[10] H. Abe, M. Yoshida, and N. Fujiwara: Jpn. J. Appl. Phys. **47** (2008) 1435.

[11] R. A. Gottscho, C. W. Jurgensen, and D. J. Vitkavage: J. Vac. Sci. Technol. B **10** (1992) 2133.

[12] S. Kato, M. Sato, and Y. Arita: J. Vac. Sci. Technol. A **12** (1994) 1204.

[13] O. Joubert, G. S. Oehrlein, M. Sarendra, and Y. Zhang: J. Vac. Sci. Technol. A **12** (1994) 1957.

[14] J. C. Arnold and H. H. Sawin: J. Appl. Phys. **70** (1991) 5314.

[15] D. J. Economou and R. C. Alkire: J. Electrochem. Soc. **135** (1988) 941.

[16] O. Joubert, G. S. Oehrlein, and M. Surenda: J. Vac. Sci. Technol. A **12** (1994) 665.

[17] K. Nojiri and E. Iguchi: J. Vac. Sci. Technol. B **13** (1995) 1451.

[18] M. Ardehali: J. Vac. Sci. Technol. A **12** (1994) 3242.

[19] T. E. Sheridan: J. Phys. D.: Appl. Phys.: **28** (1995) 1094.

[20] A. Grill: *Cold Plasma in Material Fabrication, From Fundamental to Applications* (IEEE Press, 1994, New York, NY).

[21] S. M. Rossnagel, J. J. Cuomo, and W. D. Westwood (eds): *Handbook of Plasma Processing Technology* (Noyes, 1990, Park Ridge).

[22] D. Korzec, F. Werner, R. Winter, and J. Engemann: Plasma Sources Sci. Technol. **5** (1996) 216.

[23] M. Lieberman and A. Lichtenberg: *Principles of Plasma Discharges and Materials Processing* (Wiley, 1994, New York, NY).

[24] G. G. Lister: J. Phys. D: Appl. Phys. **25** (1992) 1649.

[25] J. R. Hollahan and A. T. Bell: *Techniques and Applications of Plasma Chemistry*, (Wiley, 1974, New York). Chemical Rubber Company)

[26] M. Hirose: *Plasma-deposited films: kinetics of formation, composition, and microstructure Plasma Deposited Films*, ed. J. Mort and F. Jansen (Chemical Rubber Company, 1986, Boca Raton, FL).

[27] Y. P. Raizer: *Gas Discharge Physics* (Springer, 1991, Berlin).

[28] Y. P. Raizer, M. N. Shneider, and N. A. Yatsenko: *Radio-Frequency Capacitive Discharges* (Chemical Rubber Company, 1995, Boca Raton).

[29] O. Popov: *High Density Plasma Sources* (Noyes, 1995, Park Ridge).

[30] C. M. Ferreira and M. Moisan: *Microwave Discharges, Fundamentals and Applications (NATO ASI Series, Series B: Physics vol 302)* (Plenum, 1993, New York).

[31] J. Marec and P. Leprince: *Microwave Discharges, Fundamentals and Applications (NATO ASI Series, Series B: Physics vol 302)*, ed. C. M. Ferreira and M. Moisan (Plenum, 1993, New York).

[32] M. Konuma: *Film Deposition by Plasma Techniques* (Springer, 1992, Berlin).

[33] A. Ohl: *Microwave Discharges, Fundamentals and Applications (NATO ASI Series, Series B: Physics vol 302)*, ed. C. M. Ferreira and M. Moisan (Plenum, 1993, New York).

[34] A. Ohl: J. Physique IV **8** (1998) Pr7-83.

[35] A. v Keudell: Report IPP Garching, 1996, 9/110.

[36] H. Conrads and M. Schmidt: Plasma Sources Sci. Technol. **9** (2000) 441.

[37] K. Suzuki, S. Okudaira, N. Sakudo, and I. Kanomata: Jpn. J. Appl. Phys. **16** (1977) 1979.

[38] S. Matsuo and Y. Adachi: Jpn. J. Appl. Phys. **21** (1982) L4.

[39] S. Matsuo and M. Kiuchi: Jpn. J. Appl. Phys. **22** (1983) L210.

[40] T. Ono, C. Takahashi, and S. Matsuo: Jpn. J. Appl. Phys. **23** (1934) L534.

[41] K. Suzuki, K. Ninomiya, S. Nishimatsu, and S. Okudaira: J. Vac. Sci. Technol. B **3** (1985) 1025.

[42] J. Hopwood: Plasma Sources Sci. Technol. **1** (1992) 109.

[43] G. Holland and A. N. Eaton: *Applications of Plasma Source Mass Spectrometry* (Royal Society of Chemistry, 1991, Cambridge).

[44] The Electronic Device Failure Analysis Society (EDFAS): http://edfas.asminternational.org/portal/site/edfas/Photo2002, (Mar. 18, 2012).

[45] R. d'Agostino, F. Cramarossa, V. Colaprico, and R. d'Ettole: J. Appl. Phys. **54** (1983) 1284.

[46] S. Pang and S.R.J. Brueck: Mat. Res. Soc. Symp. Proc. **17** (1983) 161.

[47] M. Kitamura, H. Akiya, and T. Urisu: J. Vac. Sci. Technol. B **7** (1989) 14.

[48] S. Samukawa and S. Furuoya: Jpn. J. Appl. Phys. **32** (1993) L1289.

[49] K. Takahashi, M. Hori, S. Kishimoto, and T. Goto: Jpn. J. Appl. Phys. **33** (1994) 4181.

[50] J. A. O'Neill and J. Singh: J. Appl. Phys. **77** (1995) 497.

[51] T. Goto and M. Hori: Jpn. J. Appl. Phys. **35** (1996) 6521.

[52] M. M. Millard and E. Kay: J. Electrochem. Soc. **129** (1982) 160.

[53] H.-H. Doh, J.-H. Kim, S.-H. Lee, and K.-W. Whang: J. Vac. Sci. Technol. A **14** (1996) 2827.

[54] K. Siozawa, K. Tabaru, T. Maruyama, N. Fujiwara, and M. Yoneda: Jpn. J. Appl. Phys. **35** (1996) 2483.

[55] J. P. Booth, G. Hancock, and N. D. Perry: Appl. Phys. Lett. **50** (1987) 318.

[56] J. P. Booth, G. Hancock, N. D. Perry, and M. J. Toogood: J. Appl. Phys. **66** (1989) 5251.

[57] Y. Hikosaka, H. Toyoda, and H. Sugai: Jpn. J. Appl. Phys. **32** (1993) L690.

[58] J. P. Booth, G. Hancock, N. Perry, D. C. W. Blaikely, J. A. Cairns, and R. Smailes: Mat. Res. Soc. Symp. Proc. **98** (1987) 135.

[59] D. Edelson and D. L. Flamm: J. Appl. Phys. **56** (1984) 1522.

[60] I. C. Plumb and K. R. Ryan: Plasma Chem. Plasma Proc. **6** (1986) 205.

[61] N. V. Mantzaris, A. Bouvoudis, and E. Gogolides: J. Appl. Phys. **77** (1995) 6169.

[62] R. d'Agostino, F. Cramarossa, S. de Benedictis, and G. Ferraro. J. Appl. Phys. **52** (1981) 1259.

[63] R. d'Agostino, F. Cramarossa, and S. de Benedictis: Plasma Chem. Plasma Proc. **2** (1982) 214.

[64] S. G. Hansen and G. Luckman: Appl. Phys. Lett. **53** (1988) 1588.

[65] L. M. Buchmann, F. Heinrich, P. Hoffmann, and J. Janes: J. Appl. Phys. **67** (1990) 3635.

[66] C. J. Mogab, A. C. Adams, and D. L. Flamm: J. Appl. Phys **49** (1978) 3796.

[67] L. D. B. Kiss and H. H. Sawin: Plasma Chem. Plasma Proc. **12** (1992) 523.

[68] J. P. Booth, G. Cunge, P. Chabert, N. Sadeghi, and J. Derouard: Proc. IUVSTA International Workshop on Plasma Sources and Surface Intercation in Material Processing, Fuji-Yoshida, 1995, p. 28.

[69] J. P. Booth: Proc. Frontiers in Low Temperature Plasma Diagnostics, Les Houches, 1995, p. 44.

[70] S. G. Hansen, G. Luckman, G. C. Nieman, and S. D. Colson: J. Appl. Phys. **68** (1990) 2013.

[71] K. Maruyama, K. Ohkouchi, Y. Ohtsu, and T. Goto: Jpn. J Appl. Phys. **33** (1994) 4298.

[72] M. Haverlag, E. Stoffels, W. W. Stoffels, G. M. W. Kroesen, and F. J. de Hoog: J. Vac. Sci. Technol. A **12** (1994) 3102.

[73] M. Haverlag, W. W. Stoffels, E. Stoffels, J. H. W. G. den Boer, G. M. W. Kroesen, and F. J. de Hoog: Plasma Sources Sci. Technol. **4** (1995) 260.

[74] M. Haverlag, E. Stoffels, W. W. Stoffels, G. M. W. Kroesen, and F. J. de Hoog: J. Vac. Sci. Technol. A **14** (1996) 384.

[75] J. P. Sucksmith: D. Phil. Thesis, Oxford University, Oxford, 1993.

[76] D. L. Flamm: Pure. Appl. Chem. **62** (1990) 1709.

[77] T. Kinoshita, M. Hane, and J. P. McVittie: J. Vac. Sci. Technol. B **14** (1996) 560.

[78] K. P. Cheung: *Plasma Charging Damage* (Springer, 2000, London).

[79] K. P. Giapis and G. S. Hwang: Thin Solid Films **374** (2000) 175.

[80] G. S. Hwang and K. P. Giapis: J. Vac. Sci. Technol. B **15** (1997) 70.

[81] A. D. Bailey III and R.A. Gottscho: Jpn. J. Appl. Phys. **34** (1995) 2083.

[82] N. Fujiwara, H. Sawai, M. Yoneda, K. Nishioka, and H. Abe: Jpn. J. Appl. Phys. **29** (1990) 2223.

[83] G. S. Hwang and K. P. Giapis: Appl. Phys. Lett. **71** (1997) 458.

[84] T. Nozawa, T. Kinoshita, T. Nishizuka, A. Narai, T. Inoue, and A. Nakaue: Jpn. J. Appl. Phys. **34** (1995) 2107.

[85] N. Fujiwara, T. Maruyama, and M. Yoneda: Jpn. J. Appl. Phys. **34** (1995) 2095.

[86] S. Wolf: *Silicon Processing for the VLSI Era* (Lattice Press, 1995, Sunset Beach, CA) vol. 3.

[87] K. Hashimoto: Jpn. J. Appl. Phys. **32** (1993) 6109.

[88] K. P. Cheung and C. P. Chang: J. Appl. Phys. **75** (1994) 4415, and references cited therein.

[89] T. Kinoshita, M. Hane, and J. P. McVittie: J. Vac. Sci. Technol. B **14** (1996) 560.

[90] S. Samukawa and K. Terada: J. Vac. Sci. Technol. B **12** (1994) 3300.

[91] S. Samukawa: Appl. Phys. Lett. **64** (1994) 3398.

[92] T. H. Ahn, K. Nakamura, and H. Sugai: Plasma Sources Sci. Technol. **5** (1996) 139.

[93] T. H. Ahn, K. Nakamura, and H. Sugai: Jpn. J. Appl. Phys **34** (1995) L1405.

[94] T. Kinoshita, T. Nozawa, M. Hane, and J. P. McVittie: Proc. 18th Dry Process Symp., Tokyo, 1996, P. 37.

[95] M. Tuda, K. Ono, M. Tsuchihashi, M. Hanazaki, and T. Komemura: Proc. 19th Dry Process Symp., Tokyo, 1997, p. 57.

[96] T. Maruyama, N. Fujiwara, S. Ogino, and M. Yoneda: Jpn. J. Appl. Phys. **36** (1997) 2526.

[97] G. S. Hwang and K. P. Giapis: Jpn. J. Appl. Phys. **37** (1998) 2291.

Chapter 2

Plasma Gas Phase

2.1 Introduction

During plasma etching, several different kinds of reactive ions and neutrals occur in the plasma, which are incident onto the substrate surfaces being etched: feedstock gas species and their fragments (or reactants), reaction products (or etch products) desorbed from the substrate, impurities from chamber walls, and mask materials eroded [1]. In high-density plasmas such as electron cyclotron resonance (ECR) plasmas and inductively coupled plasmas (ICP), high etch rates often lead to a buildup of etch products, and hence to a reduction of the concentration of reactants. In these situations, the plasma chemical behavior of products as well as reactants is important, because the products desorbed from the substrate participate in gas-phase reactions and some of them return onto substrate surfaces, which in turn significantly influence the etching characteristics such as etch rate, profile, and their microscopic as well as macroscopic uniformity [2]. Thus, the behavior of etch products must also be taken into account in both experiments and numerical models, to gain a better understanding of the physics and chemistry underlying the process.

Coburn and Winters studied etch products desorbed from Si substrates during simultaneous exposure of Ar^+ ion beams and F_2 gases, using threshold ionization mass spectroscopy [3]. Van Veldhuizen *et al.* investigated the etching of quartz in ICP CF_4 plasmas by infrared absorption spectroscopy, to estimate the density of etch products SiF_4 and CO [4]. O'Neill *et al.* investi-

gated gas-phase reactant and product species during Si etching in ICP CF_2Cl_2 plasmas by using Fourier transform infrared (FTIR) absorption spectroscopy, to observe the generation of etch product SiF_4 [5]. Ono *et al.* found that the density of etch product $SiCl_4$ was comparable to that of feedstock gases during Si etching in ECR Cl_2 plasmas, by using laser-induced fluorecence (LIF) and FTIR absorption spectroscopy [6–8]. Cunge *et al.* observed SiF_2 radicals by LIF during Si and SiO_2 etching in capacitively coupled plasmas (CCP) with CF_4 [9]. Hebner measured the spatially resolved density of etch products SiF and SiF_2 by LIF during Si etching in ICP C_2F_6 and C_4F_8 plasmas [10, 11]. Rao *et al.* detected a significant amount of etch products SiF_x/COF_x ($x = 0-3$) by quadrupole mass spectrometry, which originated from the quartz window in ICP CF_4 plasmas [12]. Cruden *et al.* observed etch products of SiF_4, COF_2, and CO originating from the quartz window in ICP CF_4 plasmas by FTIR absorption spectroscopy, which occurred in approximately equal ratios and together account for $6-19$ % of the feedstock gases [13].

Plasma reactor simulations range from zero to three dimensional. The improvement of computer performance has recently enabled us to predict the distribution of plasma species in the reactor chamber in two and three dimensions [14–77]: 2D fluid [15, 19, 20, 22, 25, 26, 28, 36–38, 40, 42, 45, 49, 50, 52, 54, 56, 57, 59, 60, 66, 70, 71], particle [21, 35, 43], and hybrid [23, 24, 27, 29, 30, 32–34, 41, 44, 46, 47, 55, 58, 61–63, 65, 67–69, 73] models, and 3D fluid [53, 72] and hybrid [31] models. Some of these are two-dimensional simulations of ICP Ar and Cl_2 plasmas [14, 17, 20, 24–30, 32, 37, 47, 49, 56, 58, 59, 68, 69], and there are a few three-dimensional ICP models [31, 53, 72]. Some of the other work focus on two-dimensional simulations of ICP and CCP with N_2, O_2, C_2F_6, and C_4F_8 [15, 16, 23, 33, 34, 50, 55, 57, 61–63, 66, 67, 70].

In particular, several numerical studies have been concerned with the role of etch products during Si etching in ICP Cl_2 plasmas, based on two-dimensional fluid [74], particle [75, 76], and hybrid [77] models of the plasma in combination with a simple surface kinetics model, with emphasis being placed on the spatial distribution of products in the plasma reactor. Lee *et al.* investigated the role of etch products during Si etching in ICP Cl_2 plasmas using the so-called global model of zero dimension [78].

Fluorocarbon plasmas have been widely used in the etching of dielectric SiO_2 layers for interconnection of microelectronic devices [79]. The number of SiO_2 etching processes is increasing in manufacturing, with the prevalence of multi-level interconnections and the Damascene

process [80]. A number of plasma models have been reported for CF_4 [16,21,37,39,44,81–96]. Some of these are concerned with two-dimensional simulations [16, 21, 37, 86–88, 90], and some of these are with one- [89, 94, 96] and zero-dimensional ones [91]. Moreover, some models focus exclusively on gas-phase reactions and do not include etching or surface reactions [21, 89, 90, 93, 94, 96], while others include simple [16, 37, 39, 81, 82, 86, 87, 91] and detailed [44] treatments of surface reactions. Owing to the complex gas and surface chemistry in fluorocarbon plasma etching of SiO_2, which includes a number of reactive ions and neutrals, experiments are often required to be coupled with a numerical analysis to gain a better understanding of the fundamental processes underlying the etching. Thus, it is also important for SiO_2 etching in fluorocarbon plasmas that the model incorporates etch products as well as reactants in a self-consistent manner. Zhang and Kushner combined the hybrid plasma equipment and surface kinetics models for ICP fluorocarbon plasma etching of Si [41] and SiO_2 [97]. However, little analysis has been done taking into account the gas-phase as well as surface chemistry of etch products in fluorocarbon plasma etching.

In this paper, we present a two-dimensional fluid model for CF_4 plasma etching of SiO_2 in ICP, taking into account the plasma and surface chemistry of etch product species in a self-consistent manner. The next section describes the plasma fluid model used in this study, together with gas-phase chemistry in the plasma and surface chemistry on substrate surfaces and chamber walls. The numerical procedure is then given in § 2.3, and numerical results are given in § 2.4, showing that the density of etch products significantly affects plasma properties and thus etching characteristics. We discuss the plasma and surface properties as a function of externally controllable parameters such as pressure, mass flow rate, and rf coil configuration. Finally, our concluding remarks are given in § 2.5.

2.2 Model

A schematic of the ICP plasma reactor presently studied is shown in Fig. 2.1, where the reactor is a cylindrical metal chamber with a dielectric window of SiO_2 at the top, having a radius and height of $R = 15$ cm and $H = 9$ cm, respectively. The plasma is generated by 13.56-MHz rf powers fed through a multi-turn planar coil on the dielectric window. The sum of the dielectric thickness and coil radius is 2 cm, and the most inner coil is located 1.3 cm away from the

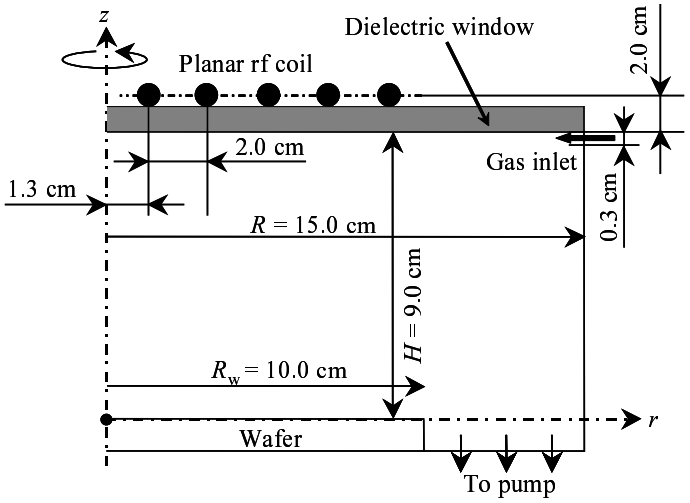

Fig. 2.1: Schematic of the ICP reactor studied in the simulation. The reactor is a cylindrical metal chamber with a dielectric window of SiO_2 at the top, having a radius and height of $R = 15$ cm and $H = 9$ cm, respectively. Plasma is generated by 13.56-MHz rf powers fed through a multi-turn coil on the dielectric window. Feedstock gases are supplied through a gas inlet ring located just under the dielectric window, being pumped away through an annular ring vacuum port at the bottom.

center with the others being placed concentrically each separated by 2 cm. The rf current in the coil produces a time-varying magnetic field, which in turn induces the azimuthal electric field that couples rf powers to plasma electrons within a skin depth layer near the plasma-dielectric interfaces. A wafer stage 10 cm in radius is located at the bottom of the chamber, which can be biased by a separate rf power supply to control the ion energy bombarding the substrate. The rf bias contributes little to ionization in the plasma, but directly affects the acceleration of positive ions through the ion sheath towards substrate surfaces. Feedstock gases are supplied through a gas inlet ring located just under the dielectric window, being pumped away through an annular ring vacuum port at the bottom. We investigate CF_4 plasmas with SiO_2 substrates for etching, at incident ion energies of 100−500 eV, pressures of 10 and 50 mTorr, mass flow rates of 100−300 sccm, and three coil configurations.

2.2.1 Inductive electric field

The electromagnetic fields are obtained by solving Maxwell's equations, with the rf spiral coil being approximated by concentric coils. Assuming the azimuthal symmetry of the system, we consider only the azimuthal component of the inductive electric field $E_\theta = \tilde{E}_\theta \exp(j\omega t)$, where ω is the angular frequency of the coil current, $I_{\rm rf} = \tilde{I}_{\rm rf} \exp(j\omega t)$, and j is the imaginary unit. The equation for the complex amplitude $\tilde{E}_\theta$ in the plasma is then expressed as

$$\frac{\partial^2 \tilde{E}_\theta}{\partial r^2} + \frac{1}{r}\frac{\partial \tilde{E}_\theta}{\partial r} + \frac{\partial^2 \tilde{E}_\theta}{\partial z^2} + \left(\omega^2 \epsilon_{\rm p} \mu_0 - \frac{1}{r^2}\right)\tilde{E}_\theta = 0, \tag{2.1}$$

where μ_0 is the permeability of vacuum. The plasma dielectric constant $\epsilon_{\rm p}$ is given by [98]

$$\epsilon_{\rm p} = \left[1 - \frac{\omega_{\rm pe}^2}{\omega(\omega - j\nu_{\rm m})}\right]\epsilon_0, \tag{2.2}$$

where $\omega_{\rm pe} = (e^2 n_{\rm e}/\epsilon_0 m_{\rm e})^{1/2}$ is the electron plasma frequency, ϵ_0 the dielectric constant of vacuum, and $\nu_{\rm m} = \nu_{\rm en} + \nu_{\rm ei}$ the sum of the momentum transfer collision frequencies between electrons and neutrals $\nu_{\rm en}$ and between electrons and ions $\nu_{\rm ei}$. Here, e is the elementary charge, $n_{\rm e}$ the electron density, and $m_{\rm e}$ the mass of electron. The boundary condition at the plasma-dielectric window interfaces is derived from Biot-Savart's law [99],

$$\tilde{E}_\theta(r_{\rm B}, z_{\rm B}) = \frac{\mu_0 \omega}{2\pi}\left[-j\tilde{I}_{\rm rf}\sum_n^{\rm coil}\left(\frac{r_n}{r_{\rm B}}\right)^{1/2} H(k_n) + \sum_{i,j}^{\rm plasma} \sigma_p(r_i, z_j)\tilde{E}_\theta(r_i, z_j)\left(\frac{r_i}{r_{\rm B}}\right)^{1/2} H(k_{ij})\Delta r \Delta z\right], \tag{2.3}$$

where $\sigma_{\rm p} = \epsilon_0 \omega_{\rm pe}^2/(j\omega + \nu_{\rm m})$ is the plasma conductivity, and Δr and Δz are the spatial grids in the radial and axial directions, respectively. Moreover, k_n and k_{ij} are given by

$$k_n^2 = \frac{4 r_{\rm B} r_n}{(z_{\rm B} - z_n)^2 + (r_{\rm B} + r_n)^2}, \tag{2.4}$$

$$k_{ij}^2 = \frac{4 r_{\rm B} r_i}{(z_{\rm B} - z_j)^2 + (r_{\rm B} + r_i)^2}, \tag{2.5}$$

where $(r_{\rm B}, z_{\rm B})$, (r_i, z_j), and (r_n, z_n) are the coordinates of the boundary points, coordinates in the simulation domain of the plasma, and coordinates of the nth turn rf coil from the center, respectively. The function $H(k)$ is given by [100]

$$H(k) = \frac{2}{k}[K(k) - E(k)] - kK(k), \tag{2.6}$$

where $K(k)$ and $E(k)$ are the complete elliptic integrals of the first and second kinds, respectively. In equation (2.3), the first sum is over all the coil current loops concerned, and the second one is over the plasma currents induced in the plasma region.

The power deposition per unit volume into the plasma averaged over an rf cycle is given by

$$W = \frac{1}{2}\mathrm{Re}\left(\sigma_\mathrm{p}|\tilde{E}_\theta|^2\right), \tag{2.7}$$

where the model assumes all the power deposited collisionally, although the collisionless heating may be important especially at low pressures [101]. The total power deposition into the chamber or into the plasma is expressed as

$$W_\mathrm{t} = 2\pi \int_0^H \int_0^R W r dr dz. \tag{2.8}$$

In practice, given the coil current $\tilde{I}_\mathrm{rf}$ and plasma conductivity σ_p, we obtain $\tilde{E}_\theta$ at the plasma-dielectric interfaces according to equation (2.3). Then, $\tilde{E}_\theta$ in the plasma is calculated by using equation (2.1), giving the power deposition W according to equation (2.7).

2.2.2 Electron energy balance

The electron energy balance is expressed as

$$\begin{aligned}\frac{\partial}{\partial t}\left(\frac{3}{2}n_\mathrm{e}k_\mathrm{B}T_\mathrm{e}\right) = W - \nabla\cdot\mathbf{q}_\mathrm{e} - \sum_n \nu_{\mathrm{en},n}\frac{3m_\mathrm{e}}{M_n}n_\mathrm{e}k_\mathrm{B}(T_\mathrm{e}-T_\mathrm{n}) \\ - \sum_i \nu_{\mathrm{ei},i}\frac{3m_\mathrm{e}}{M_i}n_\mathrm{e}k_\mathrm{B}(T_\mathrm{e}-T_\mathrm{i}) - \sum_j R_{\mathrm{e}j}\triangle H_{\mathrm{e}j},\end{aligned} \tag{2.9}$$

The electron energy flux $\mathbf{q}_\mathrm{e}$ consists of heat conduction and convection as

$$\mathbf{q}_\mathrm{e} = -\kappa_\mathrm{e}\nabla T_\mathrm{e} + \frac{5}{2}k_\mathrm{B}T_\mathrm{e}\mathbf{\Gamma}_\mathrm{e}, \tag{2.10}$$

where $\mathbf{\Gamma}_\mathrm{e}$ is the electron flux, and κ_e is the electron thermal conductivity given by [53, 74]

$$\kappa_\mathrm{e} = \frac{3}{2}k_\mathrm{B}D_\mathrm{e}n_\mathrm{e}, \tag{2.11}$$

where $D_\mathrm{e} = k_\mathrm{B}T_\mathrm{e}/m_\mathrm{e}\nu_\mathrm{m}$ is the electron diffusion coefficient. We further assume that $\mathbf{q}_\mathrm{e} = 0$ on the axis of symmetry, and that $\nabla T_\mathrm{e} = 0$ at the plasma-surface boundaries; the latter implies that the electron thermal energy transferred to substrate surfaces and reactor chamber walls is negligible.

2.2.3 Charged particle transport

The continuity equation for the ith ion species (positive and negative ions) is described as

$$\frac{\partial n_i}{\partial t} = -\nabla\cdot\mathbf{\Gamma}_i + \sum_j R_{ij}, \tag{2.12}$$

where n_i is the ith ion density, $\mathbf{\Gamma}_i$ the ith ion flux, R_{ij} the production/destruction rate for the ith ion species due to the reaction event j in the plasma, and the sum is over all the reactions that produce/destroy the ith ion. The ion flux is given by

$$\mathbf{\Gamma}_i = \mu_i n_i \mathbf{E} - D_i \nabla n_i, \tag{2.13}$$

where $\mathbf{E}$ is the electrostatic field having two components of E_r and E_z, which are independent of the inductive electric field $\tilde{E}_\theta$. Equation (4.1) assumes the drift-diffusion approximation, since the pressure of interest is high enough for gas-phase collisions to dominate the ion transport. Here, the mobility and diffusion coefficient are given by

$$\mu_i = \frac{q_i}{M_i \nu_{\mathrm{in},i}}, \qquad D_i = \frac{k_\mathrm{B} T_i}{M_i \nu_{\mathrm{in},i}}, \tag{2.14}$$

respectively, where q_i and $\nu_{\mathrm{in},i}$ are the charge and ion-neutral momentum transfer collision frequency for the ith ion. The boundary conditions are zero gradient of the density on the axis of symmetry ($\partial n_i / \partial r = 0$). Moreover, at the plasma-surface boundaries, the ith positive ion flux normal to surfaces is set equal to the Bohm flux $\Gamma_{i\perp} = 0.61 n_i \sqrt{k_\mathrm{B} T_\mathrm{e} / M_i}$; on the other hand, the negative ion density is set to zero thereat, because negative ions are repelled by the sheath potential.

Further assuming the ambipolar diffusion of ions and electrons or the flux balance of charged species in the plasma,

$$\sum_+ \mathbf{\Gamma}_+ = \sum_- \mathbf{\Gamma}_-, \tag{2.15}$$

the electrostatic field that causes the drift is given by [56]

$$\mathbf{E} = \frac{\sum_+ D_+ \nabla n_+ - \sum_- D_- \nabla n_-}{\sum_+ \mu_+ n_+ + \sum_- \mu_- n_-}. \tag{2.16}$$

Here, the subscript '+' indicates positive ions, and '−' indicates negative ions and electrons. It is noted that the electron flux $\mathbf{\Gamma}_\mathrm{e}$ is obtained from equation (2.15), and that the mobility μ_e and diffusion coefficient D_e are given by equations similar to (2.14). The electron density n_e is obtained assuming the quasi-neutrality,

$$\sum_+ n_+ = \sum_- n_-, \tag{2.17}$$

which implies that the sheath at plasma-surface boundaries is not included in the simulation.

2.2.4 Neutral species transport

The flux of the nth neutral species is given by

$$\mathbf{\Gamma}_n = -D_n \nabla n_n, \tag{2.18}$$

taking the mobility set equal to zero in equation (4.1). Here, n_n and $D_n = k_B T_n / M_n \nu_{nn,n}$ are the density and diffusion coefficient for the nth neutral, respectively, and $\nu_{nn,n}$ is the neutral-neutral momentum transfer collision frequency for the nth neutral. The corresponding continuity equation is expressed as

$$\frac{\partial n_n}{\partial t} = -\nabla \cdot \mathbf{\Gamma}_n + \sum_j R_{nj}, \tag{2.19}$$

similarly to equation (2.12), where R_{nj} is the production/destruction rate for the nth neutral species due to the reaction event j in the plasma.

Feedstock gases are taken to flow into the discharge through a gas inlet as depicted in Fig. 2.1, and to flow out of the discharge as a result of pumping. The flux of feedstock gases entering the reactor chamber is proportional to the flow rate S_{in} (sccm) at the inlet,

$$\Gamma_{\text{in}} = \frac{n_0 S_{\text{in}}}{A_{\text{in}}}, \tag{2.20}$$

where $n_0 = 2.6868 \times 10^{19}$ cm^{-3} is the Loschmidt number (or the number density at standard pressure and temperature), and A_{in} is the inlet area. The particle loss due to pumping is given by the flux Γ_{out} at the exit boundary, which is adjusted to maintain a given pressure in the chamber through auto pressure control. The boundary conditions are zero gradient of the density on the axis of symmetry ($\partial n_n / \partial r = 0$). Moreover, at the plasma-surface boundaries, the nth neutral flux normal to surfaces is set to be the thermal flux $\Gamma_{n\perp} = (1/4) n_n \sqrt{8 k_B T_n / \pi M_n}$.

2.2.5 Gas-phase and surface chemistry

Plasma etching involves various kinds of physical and chemical steps. Radicals and ions generated in the plasma diffuse to chamber walls and substrate surfaces, and then adsorb thereon. The species adsorbed on substrates react with substrate atoms to form products or etch products, which then desorb and diffuse back into the plasma. The model takes into account three chemical reaction systems: gas-phase reactions, surface reactions on chamber walls, and etching

reactions on substrate surfaces. The model contains feedstock CF_4, its fragments CF_x and CF_x^+ ($x = 1-3$), etch product SiF_4, its fragments SiF_x and SiF_x^+ ($x = 1-3$), and oxygen-containing species O, O_2, CO, CO_2, COF, COF_2, O^+, O_2^+, O^-, and CO^+ also originating from SiO_2 surfaces being etched. It should be noted here that the present plasma reactor shown in Fig. 2.1 consists of a cylindrical metal chamber with a dielectric SiO_2 window at the top; thus, surface chemistries on SiO_2 are taken into account on the dielectric window at the top as well as on substrate surfaces at the bottom of the reactor.

Gas-phase reactions in CF_4 plasmas considered in this study are listed in Table I [102–109]. Feedstock CF_4 molecules are dissociated into fluorocarbon radicals CF_x ($x = 1-3$) by electron impact (reactions G1–G3), which are then further dissociated into smaller radicals also by electron impact (G4 and G5). Moreover, fluorocarbon radicals CF_x ($x = 1-3$) recombine with fluorine atoms to form CF_{x+1} (G6–G8). The primary processes for generating positive ions CF_x^+ ($x = 1-3$) are assumed to be electron-impact dissociative ionization of feedstock CF_4 (G9–G11) and electron-impact direct ionization of their fragments CF_x (G12–G14), while the loss of positive ions is due to ion-electron and ion-ion recombination in the plasma (G16–G18). Negative ions F^- are generated primarily by electron-impact dissociative attachment to CF_4 (G15), being lost by ion-ion recombination (G17, G18) and electron detachment (G19). The reactions including oxygen-containing species are included in this study (G20–G50). Moreover, the etch product SiF_4 and its fragments SiF_x and SiF_x^+ ($x = 1-3$) are taken to react similarly to fluorocarbon species (G51–G66).

The electron-impact rate coefficients k_j for the reaction event j are calculated from the known cross section $\sigma_j(\epsilon)$ as

$$k_j = \int_0^\infty \sigma_j(\epsilon)\left(\frac{2\epsilon}{m_e}\right)^{1/2} f(\epsilon)d\epsilon, \tag{2.21}$$

where ϵ is the electron energy and $f(\epsilon)$ is the electron energy distribution function. Assuming the Maxwellian distribution for electrons, equation (2.21) becomes

$$k_j = \left(\frac{8}{\pi m_e}\right)^{1/2}\left(\frac{1}{k_B T_e}\right)^{3/2}\int_0^\infty \epsilon\sigma_j(\epsilon)\exp\left(-\frac{\epsilon}{k_B T_e}\right)d\epsilon. \tag{2.22}$$

In practice, a modified Arrhenius form $k_j = AT_e^B \exp(-C/T_e)$ is employed in this study, where A, B, and C are constants determined through fitting to the calculated k_j.

Surface chemistries considered on metal chamber walls are summarized in Table II [102, 105, 106], along with the specified reaction probabilities γ_j, where the wall temperature is as-

Table I: Gas-phase reactions considered in the simulation, where p is the gas pressure in mTorr and T_e is the electron temperature in eV.

No.	Reaction j [a,b]	Rate coefficient k_j (m^3s^{-1})	ΔH_{ej} (eV)	Ref.
	Reactions for fluorocarbons			
G1	$CF_4 + e \rightarrow CF_3 + F + e$	$2 \times 10^{-15} \exp(-13/T_e)$	12.5	[102, 103]
G2	$CF_4 + e \rightarrow CF_2 + 2F + e$	$5 \times 10^{-15} \exp(-13/T_e)$	15.0	[102, 104]
G3	$CF_4 + e \rightarrow CF + 3F + e$	$4.8 \times 10^{-17} T_e^{0.5} \exp(-20/T_e)$	20.0	[102, 104]
G4	$CF_3 + e \rightarrow CF_2 + F + e$	3.3×10^{-16}	3.0	[102, 104]
G5	$CF_2 + e \rightarrow CF + F + e$	3.3×10^{-16}	4.55	[102, 104]
G6	$CF_3 + F \rightarrow CF_4$	$2.3 \times 10^{-19} \times p$		[102]
G7	$CF_2 + F \rightarrow CF_3$	$9 \times 10^{-22} \times p$		[102]
G8	$CF + F \rightarrow CF_2$	$9.6 \times 10^{-24} \times p$		[102]
G9	$CF_4 + e \rightarrow CF_3^+ + F + 2e$	$7 \times 10^{-14} \exp(-17.4/T_e)$	15.9	[102, 103]
G10	$CF_4 + e \rightarrow CF_2^+ + 2F + 2e$	$7 \times 10^{-15} \exp(-24.7/T_e)$	22.0	[102, 103]
G11	$CF_4 + e \rightarrow CF^+ + 3F + 2e$	$9 \times 10^{-15} \exp(-30/T_e)$	27.0	[102, 104]
G12	$CF_3 + e \rightarrow CF_3^+ + 2e$	$8 \times 10^{-15} \exp(-12.2/T_e)$	8.5	[102, 104]
G13	$CF_2 + e \rightarrow CF_2^+ + 2e$	$2.5 \times 10^{-14} \exp(-12.2/T_e)$	11.4	[102, 104]
G14	$CF + e \rightarrow CF^+ + 2e$	$2.5 \times 10^{-14} \exp(-15.3/T_e)$	9.1	[102, 104]
G15	$CF_4 + e \rightarrow F^- + CF_3$	$4.6 \times 10^{-15} T_e^{-1.5} \exp(-7/T_e)$	4.8	[102, 104]
G16	$CF_3^+ + e \rightarrow CF_3$	4×10^{-14}	−8.5	[102, 104]
G17	$X^+ + F^- \rightarrow X + F$	4×10^{-13}		[102]
G18	$CF_3^+ + F^- \rightarrow CF_4$	5×10^{-14}		[102]
G19	$CF_3 + F^- \rightarrow CF_4 + e$	5×10^{-16}	−4.8	[102, 104]
	Reactions for oxygen-containing species			
G20	$O + e \rightarrow O^+ + 2e$	$9.0 \times 10^{-15} T_e^{0.7} \exp(-13.6/T_e)$	13.6	[104, 105]
G21	$O_2 + e \rightarrow O_2^+ + 2e$	$2.13 \times 10^{-14} \exp(-14.5/T_e)$	12.1	[105, 106]
G22	$O_2 + e \rightarrow O^- + O$	$8.8 \times 10^{-17} \exp(-4.4/T_e)$	3.64	[105] [c]
G23	$O^- + O^+ \rightarrow O + O$	2.7×10^{-13}		[105]
G24	$O^- + O_2^+ \rightarrow O + O_2$	1.5×10^{-13}		[105]

G25 $O^- + e \rightarrow O + 2e$	$2.0 \times 10^{-13} \exp(-5.5/T_e)$	1.53	[105] [c]
G26 $O_2 + e \rightarrow 2O + e$	$4.2 \times 10^{-15} \exp(-5.6/T_e)$	5.17	[105] [c]
G27 $O_2 + e \rightarrow O + O(^1D) + e$	$5.0 \times 10^{-14} \exp(-8.4/T_e)$	7.13	[105] [c]
G28 $O_2 + e \rightarrow O^+ + O^- + e$	$7.1 \times 10^{-17} T_e^{0.5} \exp(-17/T_e)$	17.32	[105] [c]
G29 $O_2 + e \rightarrow O^+ + O + 2e$	$5.3 \times 10^{-16} T_e^{0.9} \exp(-20/T_e)$	18.84	[105] [c]
G30 $O_2^+ + e \rightarrow O + O$	$5.2 \times 10^{-15}/T_e$	-6.97	[105] [c]
G31 $O^- + O \rightarrow O_2 + e$	3×10^{-16}	−3.64	[105] [c]
G32 $O_2 + e \rightarrow O_2(a^1\Delta_g) + e$	$1.7 \times 10^{-15} \exp(-3.1/T_e)$	0.977	[105, 107]
G33 $O_2(a^1\Delta_g) + e \rightarrow O_2^+ + 2e$	$9.0 \times 10^{-16} T_e^{2.0} \exp(-11.6/T_e)$	11.16	[105, 107] [c]
G34 $O_2(a^1\Delta_g) + e \rightarrow O^- + O$	$2.28 \times 10^{-16} \exp(-2.29/T_e)$	2.66	[105, 107] [c]
G35 $O_2(a^1\Delta_g) + e \rightarrow O_2 + e$	$5.6 \times 10^{-15} \exp(-2.2/T_e)$	−0.977	[105, 107] [c]
G36 $O_2(a^1\Delta_g) + e \rightarrow O + O + e$	$4.2 \times 10^{-15} T_e^{2.0} \exp(-4.6/T_e)$	4.19	[105, 107] [c]
G37 $CF_3 + O \rightarrow COF_2 + F$	3.1×10^{-17}		[108]
G38 $CF_2 + O \rightarrow COF + F$	1.4×10^{-17}		[108]
G39 $CF_2 + O \rightarrow CO + 2F$	4×10^{-18}		[108]
G40 $COF + O \rightarrow CO_2 + F$	9.3×10^{-17}		[108]
G41 $COF + F \rightarrow COF_2$	8×10^{-19}		[108]
G42 $COF + CF_2 \rightarrow CF_3 + CO$	3×10^{-19}		[108]
G43 $COF + CF_2 \rightarrow COF_2 + CF$	3×10^{-19}		[108]
G44 $COF + CF_3 \rightarrow CF_4 + CO$	1×10^{-17}		[108]
G45 $COF + CF_3 \rightarrow COF_2 + CF_2$	1×10^{-17}		[108]
G46 $COF + COF \rightarrow COF_2 + CO$	1×10^{-17}		[108]
G47 $CF + O \rightarrow CO + F$	2×10^{-17}		[108]
G48 $CO_2 + e \rightarrow CO + O + e$	$4.47 \times 10^{-15} T_e^{-0.201} \exp(-4.53/T_e)$	6.1	[103, 104]
G49 $COF_2 + e \rightarrow COF + F + e$	$1.13 \times 10^{-14} T_e^{-0.399} \exp(-13.10/T_e)$	6.0	[103, 104]
G50 $CO + e \rightarrow CO^+ + 2e$	$3.47 \times 10^{-13} T_e^{-0.0487} \exp(-23.8/T_e)$	14.0	[106]

Reactions for silicon fluorides			
G51 $SiF_4 + e \rightarrow SiF_3 + F + e$	$4.80 \times 10^{-15} T_e^{0.8282} \exp(-11.22/T_e)$	7.25	[106]
G52 $SiF_4 + e \rightarrow SiF_2 + 2F + e$	$1.45 \times 10^{-14} T_e^{0.01834} \exp(-16.03/T_e)$	11.9	[106]
G53 $SiF_4 + e \rightarrow SiF + 3F + e$	$6.94 \times 10^{-18} T_e^{1.187} \exp(-18.98/T_e)$	18.6	[106]
G54 $SiF_3 + F \rightarrow SiF_4$	1.0×10^{-16}		[109]
G55 $SiF_2 + F \rightarrow SiF_3$	1.0×10^{-16}		[109]
G56 $SiF + F \rightarrow SiF_2$	1.0×10^{-16}		[109]
G57 $Si + F \rightarrow SiF$	1.0×10^{-16}		Assumed
G58 $SiF_4 + e \rightarrow SiF_3^+ + F + 2e$	$1.15 \times 10^{-14} T_e^{0.6641} \exp(-17.42/T_e)$	16.0	[106]
G59 $SiF_4 + e \rightarrow SiF_2^+ + 2F + 2e$	$3.44 \times 10^{-15} T_e^{0.5108} \exp(-22.83/T_e)$	23.4	[106]
G60 $SiF_4 + e \rightarrow SiF^+ + 3F + 2e$	$6.19 \times 10^{-16} T_e^{1.090} \exp(-26.99/T_e)$	25.1	[106]
G61 $SiF_3 + e \rightarrow SiF_3^+ + 2e$	$9.79 \times 10^{-15} T_e^{0.3633} \exp(-10.21/T_e)$	9.60	[106]
G62 $SiF_2 + e \rightarrow SiF_2^+ + 2e$	$2.80 \times 10^{-14} T_e^{0.2530} \exp(-11.62/T_e)$	10.80	[106]
G63 $SiF + e \rightarrow SiF^+ + 2e$	$6.25 \times 10^{-14} T_e^{0.3258} \exp(-7.80/T_e)$	7.26	[106]
G64 $SiF_4 + e \rightarrow F^- + SiF_3$	$3.18 \times 10^{-16} T_e^{-0.3792} \exp(-9.82/T_e)$	3.8	[106]
G65 $SiF_3^+ + e \rightarrow SiF_3$	4×10^{-14}		Assumed
G66 $SiF_3^+ + F^- \rightarrow SiF_4$	5×10^{-14}		Assumed

[a] $X = CF_x$ ($x = 1$–3).

[b] $O(^1D)$, $O_2(a^1\Delta_g)$ are metastables.

[c] ΔH_{ej} is calculated from the Fourth Edition of NIST-JANAF Thermochemical Tables.

sumed to be $T_w = 300$ K. Ions of CF_x^+ ($x = 1-3$), O_x^+ ($x = 1, 2$), and CO^+ lose their charge by neutralization on the walls to generate their own neutrals CF_x, O_x, and CO, which then return into the gas phase or in the plasma (reactions W1−W3, W8−W10). The neutrals of CF_x ($x = 1-3$), F, and CO are assumed to adsorb on the walls (W4−W7, W13); on the other hand, O atoms recombine and O_2 ($a^1\Delta_g$) metastables are deactivated on the walls to generate O_2, which then returns into the gas phase (W11, W12). The etch products SiF_x, SiF_x^+ ($x = 1-3$), and Si are assumed to behave similarly to CF_x and CF_x^+ (W14−W20), where the respective reaction probabilities are taken to be the same as those for the similar CF_x and CF_x^+.

Surface chemistries for SiO_2 etching in fluorocarbon plasmas have been studied for years [83, 110–123], which are summarized in Table III according to a model of Gogolides *et al.* [124]. The removal of surface atoms of SiO_2 substrates is attributed mainly to ion-enhanced etching reactions through simultaneous exposure of reactive neutrals and energetic ions: the neutral atoms and molecules adsorbed react with SiO_2 surfaces to form surface reaction layers, which are then enhanced to be desorbed from the surfaces under energetic ion bombardment. We assume that fluorine atoms, fluorocarbon radicals, and polymers are bonded to SiO_2 surface sites, and that the etching progresses as long as the polymer does not cover all the sites. The equations of surface site balance are written as

$$\sigma_S \frac{d\theta_F}{dt} = s_F(1-\theta_{tot})\Gamma_F - 2\beta_F(1+b)\theta_F\Gamma_{ion} - 2K(T_s)\theta_F\Gamma_F, \tag{2.23}$$

$$\sigma_S \frac{d\theta_{CF_x}}{dt} = \sum_n s_{CF_n}(1-\theta_{tot})\Gamma_{CF_n} - (\beta_{CF_x} + y_C)\theta_{S_x}\Gamma_{ion} - k_{rec}\theta_{CF_x}\Gamma_F, \tag{2.24}$$

$$\begin{aligned}\sigma_S \frac{d\theta_P}{dt} = \sum_i x_i y_{d,i}\Gamma_{ion} + \beta_S\theta_{CF_x}\Gamma_{ion} - \beta_{F/P}\theta_P\theta_{F/P}\Gamma_{ion} \\ + \beta_S\theta_P\theta_{CF_x/P}\Gamma_{ion} + \sum_n s_{SiF_n}\Gamma_{SiF_n},\end{aligned} \tag{2.25}$$

where σ_S is the surface site areal density on SiO_2, θ_F, θ_{CFx}, and θ_P the surface coverages of fluorine atoms, fluorocarbon radicals, and polymers thereon, $\theta_{tot} = \theta_F + \theta_{CF_x} + \theta_P$ the sum of coverages, s_F, s_{CF_n}, and s_{SiF_n} ($n = 1-3$) the adsorption probabilities of fluorine atoms and fluorocarbon radicals on SiO_2 and of fluorosilicon radicals on all the surface sites. Moreover, b is the branching ratio of the fraction of SiF_2 radicals produced in SiO_2 etching relative to

Table II: Surface reactions considered on metal chamber walls in the simulation.

No.	Reaction j [a,b]			Reaction probability γ_j	Ref.
	Reactions for fluorocarbons				
W1	$CF_3^+(g)$	$\xrightarrow{wall}$	$CF_3(g)$	1.0	[102]
W2	$CF_2^+(g)$	$\xrightarrow{wall}$	$CF_2(g)$	1.0	[102]
W3	$CF^+(g)$	$\xrightarrow{wall}$	CF(g)	1.0	[102]
W4	$CF_3(g)$	$\xrightarrow{wall}$	$CF_3(w)$	0.05	[102]
W5	$CF_2(g)$	$\xrightarrow{wall}$	$CF_2(w)$	0.05	[102]
W6	CF(g)	$\xrightarrow{wall}$	CF(w)	0.20	[102]
W7	F(g)	$\xrightarrow{wall}$	F(w)	0.02	[102]
	Reactions for oxygen-containing species				
W8	$O^+(g)$	$\xrightarrow{wall}$	O(g)	1.0	[105]
W9	$O_2^+(g)$	$\xrightarrow{wall}$	$O_2(g)$	1.0	[105]
W10	$CO^+(g)$	$\xrightarrow{wall}$	CO(g)	1.0	[106]
W11	O(g)	$\xrightarrow{wall}$	$0.5O_2(g)$	0.40	[105]
W12	$O_2(a^1\Delta_g)(g)$	$\xrightarrow{wall}$	$O_2(g)$	0.007	[105]
W13	CO(g)	$\xrightarrow{wall}$	CO(w)	0.01	Assumed
	Reactions for silicon fluorides				
W14	$SiF_3^+(g)$	$\xrightarrow{wall}$	$SiF_3(g)$	1.0	Assumed
W15	$SiF_2^+(g)$	$\xrightarrow{wall}$	$SiF_2(g)$	1.0	Assumed
W16	$SiF^+(g)$	$\xrightarrow{wall}$	SiF(g)	1.0	Assumed
W17	$SiF_3(g)$	$\xrightarrow{wall}$	$SiF_3(w)$	0.05	Assumed
W18	$SiF_2(g)$	$\xrightarrow{wall}$	$SiF_2(w)$	0.02	Assumed
W19	SiF(g)	$\xrightarrow{wall}$	SiF(w)	0.20	Assumed
W20	Si(g)	$\xrightarrow{wall}$	Si(w)	0.20	Assumed

[a] g stands for atoms, radicals, and ions in the gas phase or in the plasma.

[b] w stands for atoms and radicals adsorbed on the walls.

Table III: Surface reactions considered on SiO_2 surfaces (dielectric window as well as substrate surfaces) during etching in the simulation, where T_s is the surface temperature of 300 K.

No.	Reaction [a,b]	Flux	Surface coverage	Rate coefficient [c,d]	Ref.
	Physical sputtering				
S1	SiO_2* → Si(g) + 2O(g)	Γ_{ion}	$1-\theta_{tot}$	$y_{sp,i} = A_i(\sqrt{E_i} - \sqrt{E_{th}})$ [e]	[124]
	Reactions with F atoms				
S2	SiO_2* → SiO_2F_2(s) + 2F(g)	Γ_F	$1-\theta_{tot}$	$s_F = 0.02$	[124]
S3	SiO_2F_2(s) → SiF_4(g) + O_2(g) + 2F(g)	Γ_{ion}	θ_F	$\beta_F = 0.0454(\sqrt{E_i} - \sqrt{E_{th}})$ [f]	[124]
S4	SiO_2F_2(s) → SiF_2(g) + O_2(g) + 2F(g)	Γ_{ion}	θ_F	$\beta_F b = 0.0454b(\sqrt{E_i} - \sqrt{E_{th}})$ [f]	[124]
S5	SiO_2F_2(s) → SiF_4(g) + O_2(s) + 2F(g)	Γ_F	θ_F	$K(T_s) = \frac{K_0 \rho N_A}{M_w} \exp\left(-\frac{E_a}{kT_s}\right)$	[124]
	Reactions with fluorocarbon radicals				
S6	SiO_2* → SiO_2CF_x(s) + CF_x(g)	Γ_{CF_x}	$1-\theta_{tot}$	$s_{CF_x} = 0.1$	Assumed
S7	SiO_2CF_x(s) → SiF_x(g) +2CO(g)	Γ_{ion}	θ_{CF_x}	$\beta_{CF_x} = 0.361(\sqrt{E_i} - \sqrt{E_{th}})$ [f]	[124]
S8	SiO_2CF_x(s) → Si(s) + $2COF_x$(g)	Γ_{ion}	θ_{CF_x}	$y_C = 0.0361$	[124]
S9	SiO_2CF_x(s) → SiO_2* + CF_{x+1}(g) + F(g)	Γ_F	θ_{CF_x}	$k_{rec} = 0.60$	[124]
	Reactions of polymer creation or loss				
S10	CF_x^+(g) → P	Γ_{ion}	1	$y_{d,i} = -A_{d,i}\sqrt{E_i}$ [g] $(0 < E_i \le \frac{1}{2}E_{th})$	[124]
				$y_{d,i} = A_i(\sqrt{E_i} - \sqrt{E_{th}})$ [h] $(\frac{1}{2}E_{th} < E_i < E_{th})$	[124]
S11	SiO_2CF_x(s) → P	Γ_{ion}	θ_{CF_x}	$\beta_s = 0.0361$	[124]

S12	P–F(s/P)	→ etching of P	Γ_{ion}	$\theta_P\theta_{F/P}$	$\beta_{F/P} = 0.2\,(\sqrt{E_i} - \sqrt{E_{th}})^i$	[124]
S13	P–CF_x(s/P)	→ more P	Γ_{ion}	$\theta_P\theta_{CF_x/P}$	$\beta_s = 0.0361$	[124]
S14	SiF_x(g)	→ P	Γ_{SiF_x}	1	$s_{SiF_x} = 0.1$	Assumed
	Reactions with F atoms on polymer surfaces					
S2'	P + 2F(g)	→ P–F_2(s)	Γ_F	$\theta_P(1 - \theta_{tot/P})$	$s_{F/P} = 0.1$	Assumed
S3'	P–F_2(s) + 2F(p)	→ CF_4(g) + O_2(g) + P	Γ_{ion}	$\theta_P\theta_{F/P}$	$\beta_{F/P} = 0.2\,(\sqrt{E_i} - \sqrt{E_{th}})^i$	Assumed
	Reactions with fluorocarbon radicals on polymer surfaces					
S6'	P + CF_x(g)	→ P–CF_x(s)	Γ_{CF_x}	$\theta_P(1 - \theta_{tot/P})$	$s_{CF_x/P} = 0.1$	Assumed
S7'	P–2CF_x(s)	→ CF_x(g) +2CO(g) + P	Γ_{ion}	$\theta_P\theta_{CF_x/P}$	$\beta_{CF_x/P} = 0.2\,(\sqrt{E_i} - \sqrt{E_{th}})^i$	Assumed
S8'	P–CF_x(s)	→ Si(s) + 2COF_x(g) + P	Γ_{ion}	$\theta_P\theta_{CF_x/P}$	$y_C = 0.0361$	Assumed
S9'	P–CF_x(s) + F(g)	→ P + CF_{x+1}(g)	Γ_F	$\theta_P\theta_{CF_x/P}$	$k_{rec} = 0.60$	[124]

[a] p, s, P, and s/P stand for physisorbed atoms, chemisorbed atoms and radicals, polymer, and chemisorbed atoms and radicals on polymer surface, respectively.

[b] The symbol (*) denotes a dangling bond or a site for chemisorption.

[c] A_i and $A_{d,i}$ are constants.

[d] K_0, E_a, ρ, N_A, and M_w stand for a constant, activation energy, material density, Avogadro's number, and the atomic or molecular weight of the material being etched, respectively.

[e] A_i = 0.0456 (CF_3^+), 0.0306 (CF_2^+), 0.0228 (CF^+), E_{th} = 20 eV (CF_3^+), E_{th} = 80 eV (CF_2^+), E_{th} = 150 eV (CF^+).

[f] E_{th} = 4 eV.

[g] $A_{d,i}$ = 0.0189 (CF_3^+), 0.0127(CF_2^+), 0.0094(CF^+), E_{th} = 20 eV (CF_3^+), E_{th} = 80 eV (CF_2^+), E_{th} = 150 eV (CF^+).

[h] A_i = 0.0456 (CF_3^+), 0.0306 (CF_2^+), 0.0228 (CF^+), E_{th} = 20 eV (CF_3^+), E_{th} = 80 eV (CF_2^+), E_{th} = 150 eV (CF^+).

[i] E_{th} = 4 eV.

that of SiF_4, described as $b = b_0\sqrt{E_i}$, where $b_0 = 0.007$ is the coefficient of the branching ratio and E_i is the ion energy [117]; $K(T_s)$ is the thermal (chemical) etching coefficient for fluorine atoms at a surface temperature T_s. The coefficients β_F and β_{CF_x} are the ion-enhanced SiO_2 etching yields by fluorine atoms and fluorocarbon radicals, respectively, $\beta_{F/P}$ the ion-enhanced polymer etching yield by fluorine atoms, β_S the ion-enhanced deposition yield of adsorbed fluorocarbon radicals, y_C the carbon sputtering yield, k_{rec} the recombination coefficient of adsorbed fluorocarbon radicals and fluorine atoms, x_i the ratio of the ith ion ($i = 1-3$) to the total ion flux, $y_{d,i}$ the direct ion deposition yield for the ith ion, and $\theta_{F/P}$ and $\theta_{CFx/P}$ the coverages of fluorine atoms and fluorocarbon radicals on the polymer. In addition, Γ_{ion}, Γ_F, Γ_{CF_n}, and Γ_{SiF_n} ($n = 1-3$) are the incident fluxes of ions, fluorine atoms, fluorocarbon radicals, and fluorosilicon radicals onto the surfaces, respectively.

The F and CF_x site balances on the polymer surfaces are written in a similar manner:

$$\sigma_S \frac{d\theta_P\theta_{F/P}}{dt} = s_{F/P}\theta_P(1-\theta_{tot/P})\Gamma_F - \beta_{F/P}\theta_P\theta_{F/P}\Gamma_{ion}, \tag{2.26}$$

$$\sigma_S \frac{d\theta_P\theta_{CF_x/P}}{dt} = \sum_n s_{CF_n/P}\theta_P(1-\theta_{tot/P})\Gamma_{CF_n} - (\beta_{CF_x/P}+y_C)\theta_P\theta_{CF_x/P}\Gamma_{ion} - k_{rec}\theta_P\theta_{CF_x/P}\Gamma_F, \tag{2.27}$$

where $\theta_{tot/P} = \theta_{F/P} + \theta_{CF_x/P}$ is the sum of surface coverages of fluorine atoms and fluorocarbon radicals on the polymer, $s_{F/P}$ and $s_{CF_n/P}$ ($n = 1-3$) the adsorption probabilities of fluorine atoms and fluorocarbon radicals on the polymer, and $\beta_{CF_x/P}$ the ion-enhanced polymer etching yield by fluorocarbon radicals. In the calculation, s_{CF_n}, s_{SiF_n}, and $s_{CF_n/P}$ are taken to be s_{CF_x}, s_{SiF_x}, and $s_{CF_x/P}$, irrespective of the species concerned.

It is noted that the first term of equation (2.23) represents the adsorption of fluorine atoms on SiO_2 (reaction S2), the second term the removal of fluorine atoms by ion-enhanced etching to produce SiF_4 and SiF_2 (S3, S4), and the third term the chemical etching by fluorine atoms (S5). The first term of equation (2.24) represents the adsorption of fluorocarbon radicals on SiO_2 (S6), the second term the removal of fluorocarbon radicals by ion-enhanced etching (S7) and carbon sputtering (S8), and the third term the removal of fluorocarbon radicals by recombination with fluorine atoms (S9). The first term of equation (2.25) represents the direct ion deposition (S10), the second term the ion-enhanced deposition of fluorocarbon radicals

adsorbed on SiO_2 (S11), the third term the ion-enhanced etching of polymer (S12), the forth term the ion-enhanced deposition of fluorocarbon radicals adsorbed on polymer (S13), and the last term the direct deposition of silicon fluorides (S14). Moreover, equations (2.26) and (2.27) characterizing reactions on polymer surfaces are assumed to be similar to equations (2.23) and (2.24), respectively. The first term of equation (2.26) represents the adsorption of fluorine atoms on polymer (S2'), and the second term the removal of fluorine atoms by ion-enhanced etching (S3'). The first term of equation (2.27) represents the adsorption of fluorocarbon radicals on polymer (S6'), the second term the removal of fluorocarbon radicals by ion-enhanced etching (S7') and carbon sputtering (S8'), and the third term the removal of fluorocarbon radicals by recombination with fluorine atoms (S9').

Here, we solve equations (2.23)−(2.27) to obtain the surface site coverage θ_{F}, θ_{CF_x}, θ_{P}, $\theta_{\mathrm{F/P}}$, and $\theta_{\mathrm{CF}_x/\mathrm{P}}$ under steady-state conditions ($d/dt = 0$). These surface coverages are used to determine the net fluxes of reactants and products into and out of the surface. The etch rate is given by

$$ER = \Gamma_{\mathrm{SiF}_x}/\rho_{\mathrm{SiO_2}}, \tag{2.28}$$

where $\rho_{\mathrm{SiO_2}} = 2.64 \times 10^{22}$ molecules/cm^3 is the material density of SiO_2 to be etched, and Γ_{SiF_x} is the flux of SiF_n ($n = 0$−4) molecules leaving SiO_2 surfaces through surface reactions given by

$$\Gamma_{\mathrm{SiF}_x} = \sum_i x_i y_{\mathrm{sp},i}(1-\theta_{\mathrm{tot}})\Gamma_{\mathrm{ion}} + \beta_{\mathrm{F}}(1+b)\theta_{\mathrm{F}}\Gamma_{\mathrm{ion}} + K(T)\theta_{\mathrm{F}}\Gamma_{\mathrm{F}} + (\beta_{\mathrm{CF}_x} + y_{\mathrm{C}})\theta_{\mathrm{CF}_x}\Gamma_{\mathrm{ion}}, \tag{2.29}$$

where $y_{\mathrm{sp},i}$ is the physical sputtering yield by the ith ion. The first term of (2.29) represents the physical sputtering of SiO_2 (S1), the second term the ion-enhanced etching by fluorine atoms (S3, S4), the third term the purely chemical etching by fluorine atoms (S5), and the last term the ion-enhanced etching by fluorocarbon radicals (S7) and carbon sputtering (S8).

2.3 Numerical procedures

We employed a home-made code in Fortran programing language to obtain steady-state solutions. The model consists of an electromagnetic equation for the inductive electric field power-

ing the plasma, an equation for the electron energy assuming Maxwellian electrons, and continuity equations for charged (positive and negative ions) and neutral species including gas-phase and surface reactions. The present model is based on the fluid approximation, with the charged particle flux being further described by the drift-diffusion approximation and the neutral flux by the diffusion approximation [125, 126]. These equations include a stiff system which involves both fast and slow time-varying phenomena, and so a modular approach is essential to overcome the disparate time scales associated with the transport and chemistry of electrons and heavy particles (ions and neutrals) in the plasma.

In the electromagnetic module, we employ the cylindrical coordinates (r, z), assuming the azimuthal symmetry of the system; Maxwell's equations are solved to obtain the power deposition into the plasma, where equation (2.1) is spatially discretized with the finite-volume approximation [127] and solved for each unit cell with a boundary condition (2.3) at the plasma-dielectric window interfaces. The spatial steps are taken to be $\Delta r = 0.5$ cm and $\Delta z = 0.3$ cm, where the simulation area is divided into 30 cells in the r direction and 30 cells in the z direction. In the electron energy module, the electron temperature is determined by integrating equation (2.9) with no transfer of the electron thermal energy at plasma-surface boundaries (on chamber walls and substrate surfaces). In the plasma reaction module, the rate coefficients for gas-phase reactions through electron impact are calculated as a function of electron temperature, being employed in source and sink terms of the continuity equations (2.12) and (2.19) for charged and neutral species to obtain their densities in the plasma. Then, we integrate a set of the ordinary differential equations by iterating Gear's backward differential formulae (BDF) method [128] with the minimum time step $\Delta t = 1 \times 10^{-7}$ s, assuming initial two-dimensional profiles of the electron density, temperature, and species densities. At plasma-surface boundaries, given the flux of positive ions and neutrals from the plasma onto surfaces, the surface site balance model of equations such as (2.23)−(2.27) is employed to analyze surface reactions, to obtain the flux of reaction products desorbed from surfaces into the plasma. The electron density is calculated by charge neutrality to give the plasma conductivity, which in turn is employed in Maxwell's equations.

In the present simulation, we include 12 charged and 16 neutral species, along with 66 gas-phase reactions and 40 surface reactions (20 on chamber walls and 20 on substrate surfaces). The electron transport properties in electromagnetic and fluid equations are given based on the

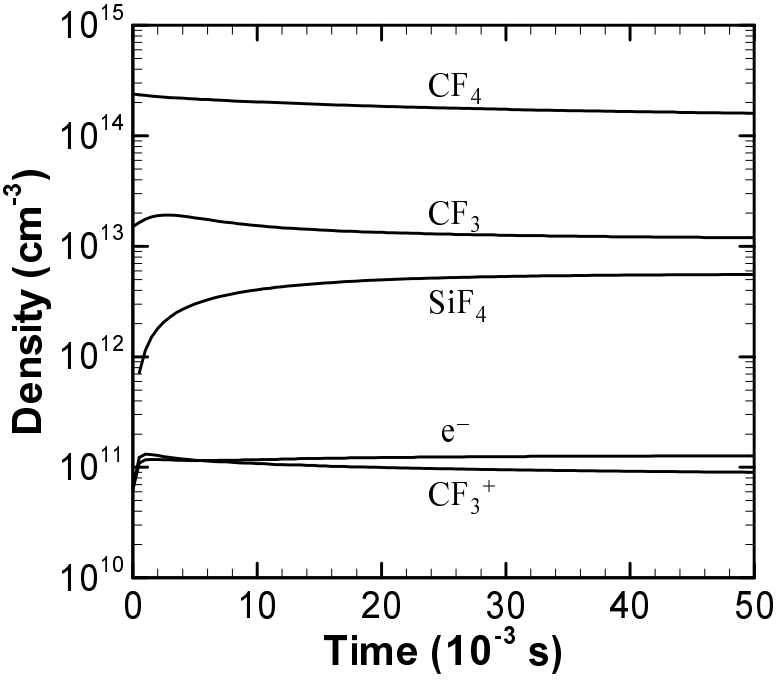

Fig. 2.2: Time variation of the spatially averaged densities of several major species: a gas pressure of 10 mTorr, a feedstock CF_4 flow rate of 200 sccm, a total power deposition of 250 W, and an ion bombardment energy of 100 eV on substrate surfaces.

electron momentum transfer collision cross section [129], and the transport properties for neutrals and ions therein are given based on the Lennard-Jones parameter and polarizability [88]. The following is chosen as standard conditions: a gas pressure of 10 mTorr, a feedstock CF_4 flow rate of 200 sccm, a total power deposition of 250 W at an rf frequency of 13.56 MHz, and an ion bombardment energy of 100 eV on substrate surfaces of temperature $T_s = 300$ K. The ion bombardment energy on SiO_2 surfaces of the dielectric window is determined from the plasma and floating potentials as $E_i = V_p - V_f = k_B T_e[0.5 + (M_i/2\pi m_e)^{1/2}]$, which is in the range 15−20 eV in the present simulation. The numerical procedure is iterated until a steady-state solution is obtained. Figure 2.2 shows the time variation of the spatially averaged density of major species under the standard condition, indicating that the species density converges to the steady state for less than several 10 ms.

2.4 Results and Discussion

Figures 2.3(a)−2.3(j) show the two-dimensional distribution of plasma properties in the reactor chamber under the standard conditions. Figure 2.3(a) gives the power deposition, most of which is localized near the coil, since the electromagnetic waves cannot penetrate the high-density plasma over a few skin depths ($\delta \sim 1.5$ cm). The peak power deposition is more than 0.7 W/cm^3 just beneath the coil. Figure 2.3(b) gives the feedstock CF_4 density, which is maximum near the gas inlet and decreases farther away from the inlet. Figures 2.3(c) and 2.3(d) give the electron density and temperature, respectively, where the electrons produced by ionization are mainly lost by ambipolar diffusion to the chamber walls and by dissociative attachment to CF_4 in the plasma. Although the electron temperature is maximum beneath the coil where the power deposition is maximum, the high thermal conductivity for electrons at low pressures results in heating up the whole plasma in the reactor. Figures 2.3(e) and 2.3(f) give the F atom and F^- ion densities, respectively. Neutral F atoms are produced mainly through electron-impact dissociation of the feedstock CF_4 and its fragments CF_3 and CF_2, in the central upper part of the reactor chamber where the electron density and temperature are relatively high. On the chamber walls, F atoms are adsorbed with a probability $\gamma_j = 0.02$, or reemitted with a probability $(1 - \gamma_j)$. Negative F^- ions are produced through dissociative electron attachment to CF_4 in abundant CF_4 atmospheres near the gas inlet, being confined by the ambipolar electric fields owing to its

negative charge, and being lost in the central part of the chamber by frequent ion-ion recombination with positive ions such as CF_3^+ and SiF_3^+. Figures 2.3(g) and 2.3(h) give the density of fragments CF_2 and CF_3^+, respectively. The CF_2 neutral density is maximum around beneath the coil, where CF_2 neutrals are produced mainly through electron-impact dissociation of CF_4 and CF_3. The CF_3^+ ion density has a peak in the central middle part of the chamber, where CF_3^+ ions are produced through electron-impact dissociative ionization of CF_4 and also electron-impact ionization of CF_3. Figures 2.3(i) and 2.3(j) give the density of etch products SiF_4 and SiF_3^+, respectively. The SiF_4 density has a strong downhill-like gradient from the central region on SiO_2 substrates towards the exit owing to a large amount of SiF_4 production thereon, implying that the diffusion is slower than surface reactions. The SiF_4 molecules are produced on SiO_2 dielectric windows as well as on substrate surfaces; in practice, the density of products decays away from both the top and bottom boundaries. It is noted here that the etch rate ER was typically 0.46 μm/min for substrates, while 0.28 μm/min for dielelctric windows. The SiF_4 density is about 10% of that of the feedstock CF_4, and is comparable to that of CF_2; thus, etch products are not negligible in etching reactions. Electron-impact dissociation and ionization produce fragments SiF_x and SiF_x^+ ($x = 1-3$). The SiF_3^+ ion density has a peak at the central middle part of the chamber, decreasing towards boundary surfaces through ambipolar diffusion. The location of the SiF_3^+ and CF_3^+ density peak almost corresponds to that of the electron density peak, while the density of SiF_3^+ is about 5% of that of CF_3^+.

Figures 2.4(a) and 2.4(b) show the radial distribution of different ion and neutral fluxes incident on substrate surfaces, respectively, derived from the results of Fig. 2.3. The ion and neutral fluxes decrease radially towards the edge, being consistent with the distribution of the respective ion and neutral densities in the plasma near the substrate surfaces as shown in Fig. 2.3. The neutral-to-ion flux ratio is typically $\Gamma_F/\Gamma_{CF_3^+} \approx 100$ and $\Gamma_{CF_2}/\Gamma_{CF_3^+} \approx 10$. Figure 2.4(c) shows the distribution of etch rate ER and surface coverages θ_F, θ_{CF_x}, and θ_P of F atoms, CF_x radicals, and polymers. The coverage is determined by a balance between ion and neutral fluxes; in practice, the F coverage θ_F increases with increasing F flux, while it decreases with increasing ion flux; and the CF_x coverage θ_{CF_x} increases with increasing CF_x flux, while it decreases with increasing ion and F fluxes. The etch rate ER decreases gradually in the radial direction towards the edge and then slightly increases near the edge, which is governed primarily by the ion-enhanced etching with F atoms and CF_x radicals adsorbed on substrate surfaces. A drop in the

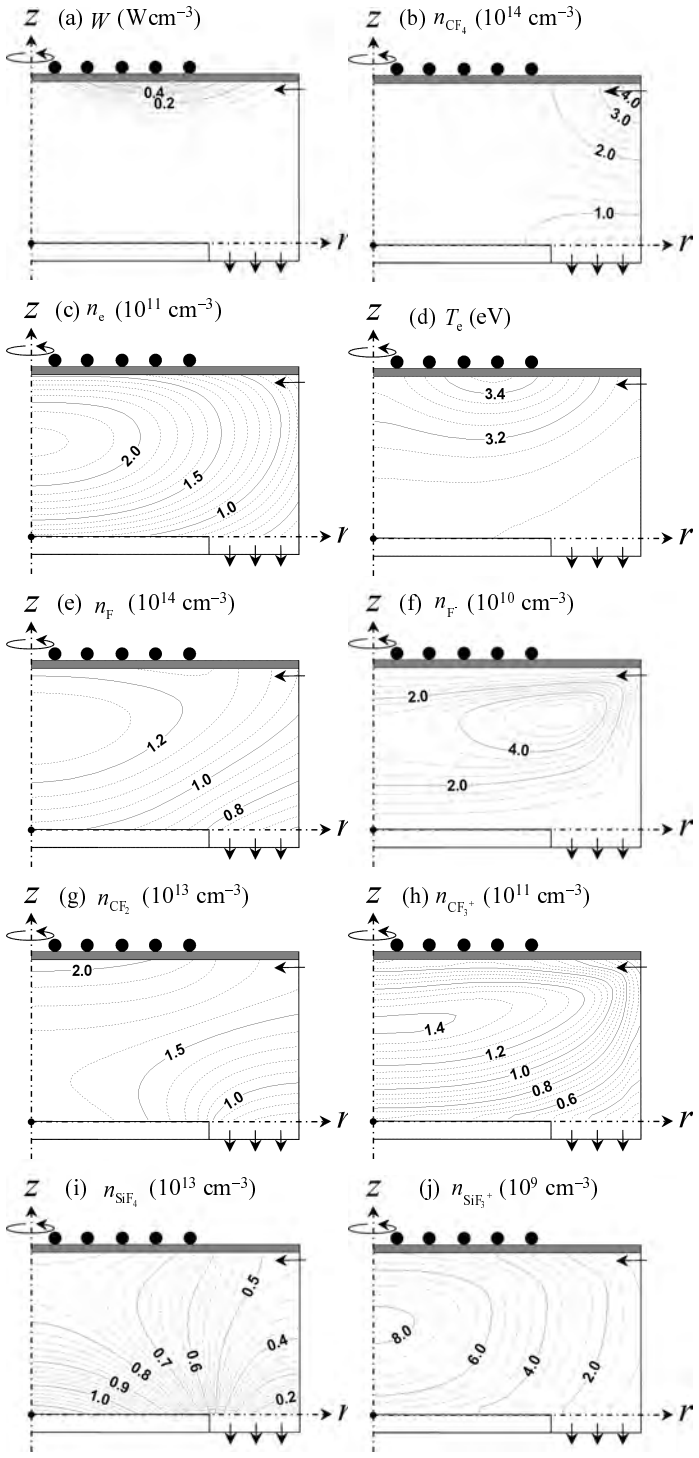

Fig. 2.3: Two-dimensional distributions of (a) power deposition, (b) feedstock CF_4 density, (c) electron density, (d) electron temperature, (e) F density, (f) F^- density, (g) CF_2 density, (h) CF_3^+ density, (i) SiF_4 density, and (j) SiF_3^+ density under the standard conditions: a gas pressure of 10 mTorr, a feedstock CF_4 flow rate of 200 sccm, a total power deposition of 250 W, and an ion bombardment energy of 100 eV on substrate surfaces of temperature T_s = 300 K.

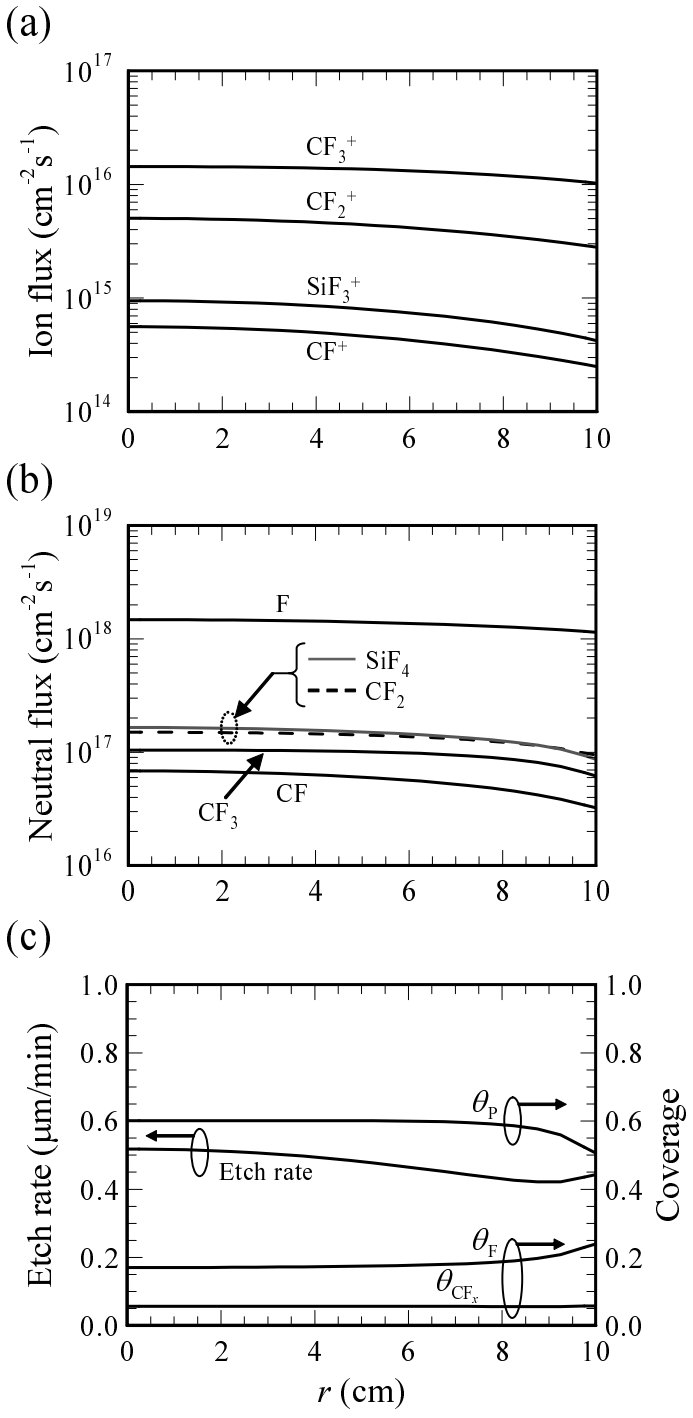

Fig. 2.4: Radial distributions on substrate surfaces of (a) ion fluxes, (b) neutral fluxes, and (c) etch rate and surfaces coverages θ_P, θ_F, and θ_{CF_x} under the standard conditions of Fig. 2.3.

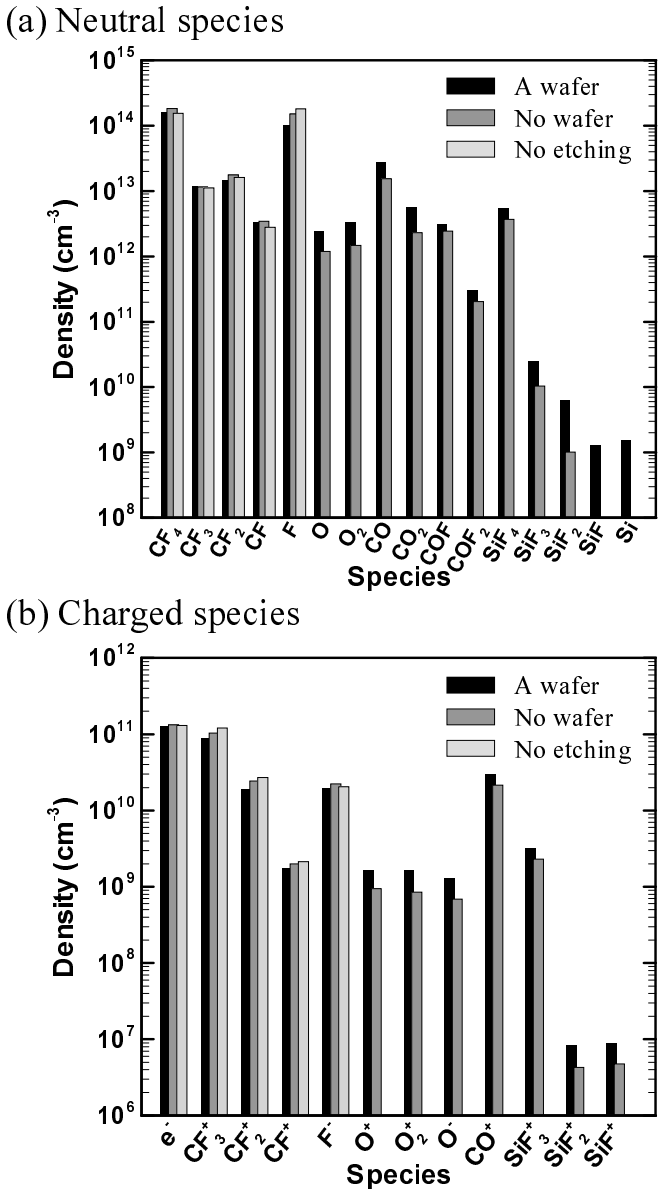

Fig. 2.5: Chemical compositions of (a) neutral and (b) charged species averaged over the entire region of the reactor chamber in three cases of ”a wafer ”, ”no wafer”, and ”no etching”, with the other parameters being the same as those under the standard conditions of Fig. 2.3. Etching occurs on both the SiO_2 dielectric window and substrate surfaces in the ”a wafer” case (or a case of Figs. 2.3 and 2.4), and occurs only on the SiO_2 dielectric window in the ”no wafer” case; in contrast, no etching occurs on any surfaces in the ”no etching” case.

polymer coverage θ_P near the edge also contributes to the increased *ER* thereat.

Figures 2.5(a) and 2.5(b) show the chemical composition of neutral and charged species,

respectively, averaged over the entire region of the reactor chamber, where calculations were made for three cases of ”a wafer”, ”no wafer”, and ”no etching” with the other parameters being the same as those under the standard conditions of Fig. 2.3. Etching occurs on both the SiO_2 dielectric window and substrate surfaces in the ”a wafer” case (or a case of Figs. 2.3 and 2.4), and occurs only on the SiO_2 dielectric window in the ”no wafer” case; on the other hand, no etching occurs on any surfaces in the ”no etching” case, where there are no etch products such as CO, SiF_4, and SiF_3^+. Under the ”no wafer” case, etch products are attributed to SiO_2 surface reactions of the dielectric window. It is noted that the etch product densities are larger in the ”a wafer” case than in the ”no wafer” case. In both cases, the densities of the feedstock CF_4 and its fragment neutrals and ions such as CF_x, F, and CF_x^+ tend to be decreased as compared with those in the ”no etching” case, as a result of desorption of etch products into the reactor chamber; in contrast, the electron and F^- ion densities remain almost unchanged. The CO radical density is the largest among etch products, and that of CO^+ ions is the largest among product ions, which are possible to contribute to the ion-enhanced etching.

Here, we did a sensitivity analysis by changing the assumed coefficients, indicating that the results were not so sensitive to changes in the coefficient of gas-phase reactions. However, the results were sensitive to changes in the coefficient of surface reactions, in particular, the adsorption probability of CO on chamber walls.

2.4.1 Ion energy dependence

Figures 2.6(a)−2.6(h) show the two-dimensional distribution of plasma properties in the reactor chamber for a higher ion energy of 500 eV, with the other parameters being the same as those under the standard conditions of Fig. 2.3. A comparison between Figs. 2.3 and 2.6 indicates that as a result of increased ion bombardment energy on the substrate surfaces, the density of etch product SiF_4 in the plasma is typically 1.3 times larger than that for the ion energy of 100 eV. Correspondingly, the density of product ion SiF_3^+ is also increased, while the densities of fragment neutrals and ions such as CF_2 and CF_3^+ are slightly decreased at a constant pressure. It is noted that the etch rate ER was increased to typically 0.68 μm/min for the substrates, while slightly decreased to typically 0.24 μm/min for the dielectric window. Figures 2.7(a) and 2.7(b) show the chemical composition of neutral and charged species for different ion energies of 100 (standard), 300, and 500 eV, averaged over the entire region of the reactor chamber. Note that

these data correspond to those in "a wafer" case, and so the data for 100 eV are the same as those in the "a wafer" case of Fig. 2.5; in addition, the data in the "no wafer" and "no etching" cases for 100 eV are the same as those in Fig. 2.5. The densities of fluorocarbon radicals CF_x ($x = 1-3$) are smaller for higher ion energies, while the densities of etch products such as O-containing species and SiF_x ($x = 0-4$) are larger for higher ion energies. Correspondingly, the densities of fluorocarbon ions CF_x^+ ($x = 1-3$) are smaller, and the densities of product ions such as O-containing ions and SiF_x^+ ($x = 1-3$) are larger for higher ion energies.

2.4.2 Pressure dependence

Figures 2.8(a)−2.8(h) show the two-dimensional distribution of plasma properties in the reactor chamber for a higher pressure of 50 mTorr, with the other parameters being the same as those under the standard conditions of Fig. 2.3. A comparison between Figs. 2.3 and 2.8 indicates that as a result of increased pressure, the electron density has a maximum in the vicinity of the coil, decreasing significantly towards the bottom of the chamber, which is ascribed to the lowered electron thermal conduction as well as ambipolar diffusion of ions and electrons at increased pressures. Correspondingly, the densities of fragment neutrals and ions such as F, CF_2 and CF_3^+ are decreased at around substrate surfaces at the chamber bottom, which in turn results in reduced densities of etch product SiF_4 and product ion SiF_3^+ in the plasma. It is noted that the etch rate *ER* was decreased to typically 0.06 μm/min for substrates, where the neutral-to-ion flux ratio was typically $\Gamma_F/\Gamma_{CF_3^+} \approx 400$ and $\Gamma_{CF_2}/\Gamma_{CF_3^+} \approx 60$ with $\Gamma_{CF_3^+} \approx 1.5 \times 10^{15}$ cm^{-3}; on the other hand, the *ER* remained almost unchanged at typically 0.27 μm/min for the dielectric window, and thus the etch product originated primarily from the SiO_2 dielectric window beneath the coil.

Figures 2.9(a) and 2.9(b) show the chemical composition of neutral and charged species for different pressures of 10 (standard) and 50 mTorr, averaged over the entire region of the reactor chamber. Note that the data for 10 mTorr are the same as those in the "a wafer" case of Fig. 2.5. The densities of F atoms and fluorocarbon radicals CF_x ($x = 1, 3$) tend to be smaller at higher pressures, and the densities of etch products such as O-containing species and SiF_x ($x = 0-4$) are also smaller at higher pressures. Correspondingly, the densities of fluorocarbon ions CF_x^+ ($x = 1-3$) tend to be smaller, and the densities of product ions such as O-containing ions and SiF_x^+ ($x = 1-3$) are smaller at higher pressures.

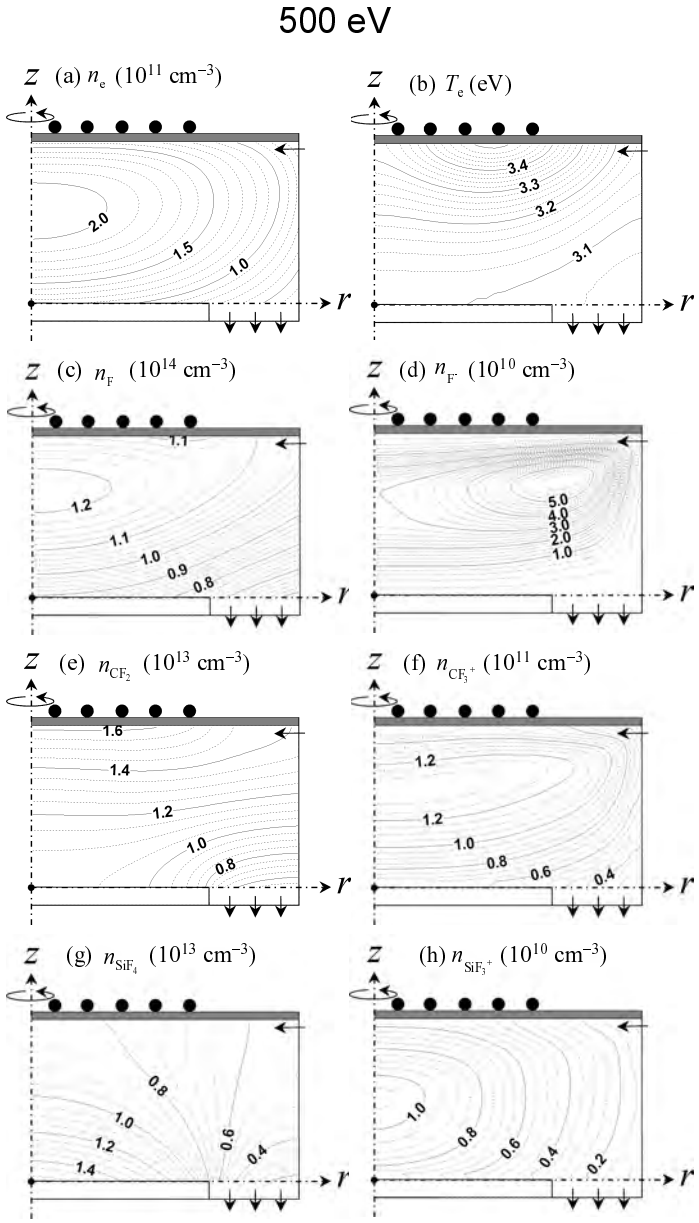

Fig. 2.6: Two-dimensional distributions of plasma properties in the reactor chamber for a higher ion energy of 500 eV with the other parameters being the same as those under the standard conditions of Fig. 2.3: (a) electron density, (b) electron temperature, (c) F density, (d) F^- density, (e) CF_2 density, (f) CF_3^+ density, (g) SiF_4 density, and (h) SiF_3^+ density.

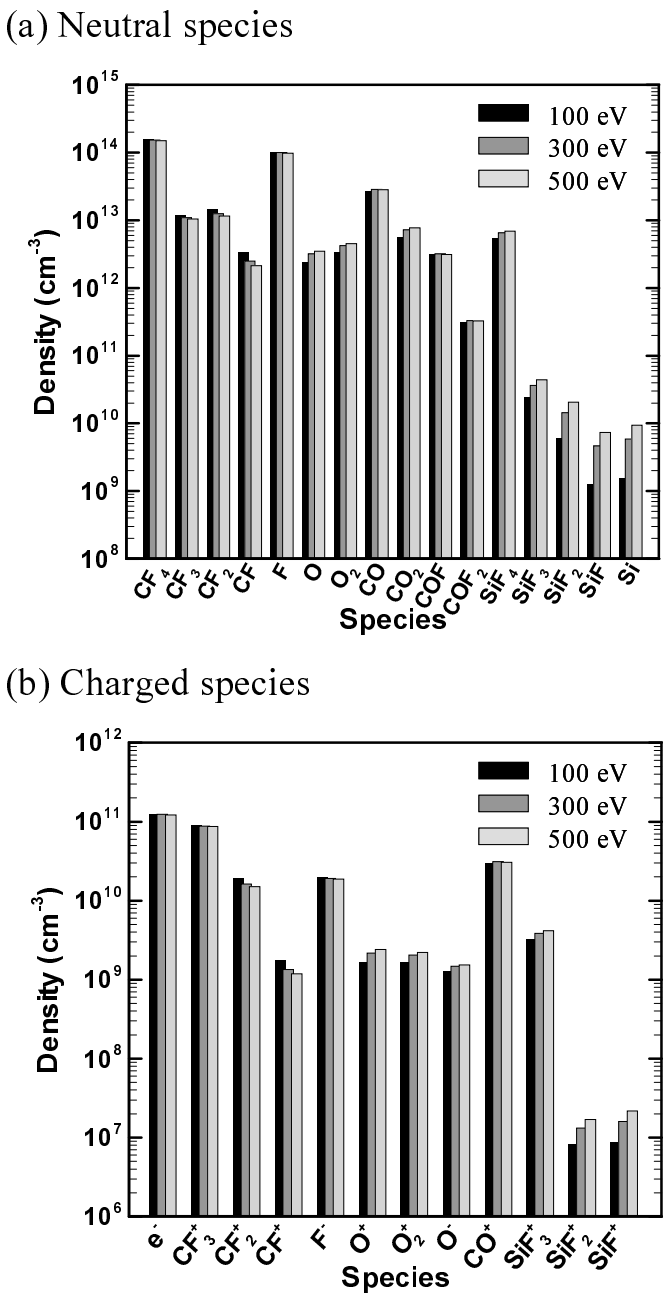

Fig. 2.7: Chemical compositions of (a) neutral and (b) charged species averaged over the entire region of the reactor chamber for different ion energies of 100 (standard), 300, and 500 eV. Note that the data for 100 eV are the same as those in ”a wafer” case of Fig. 2.5.

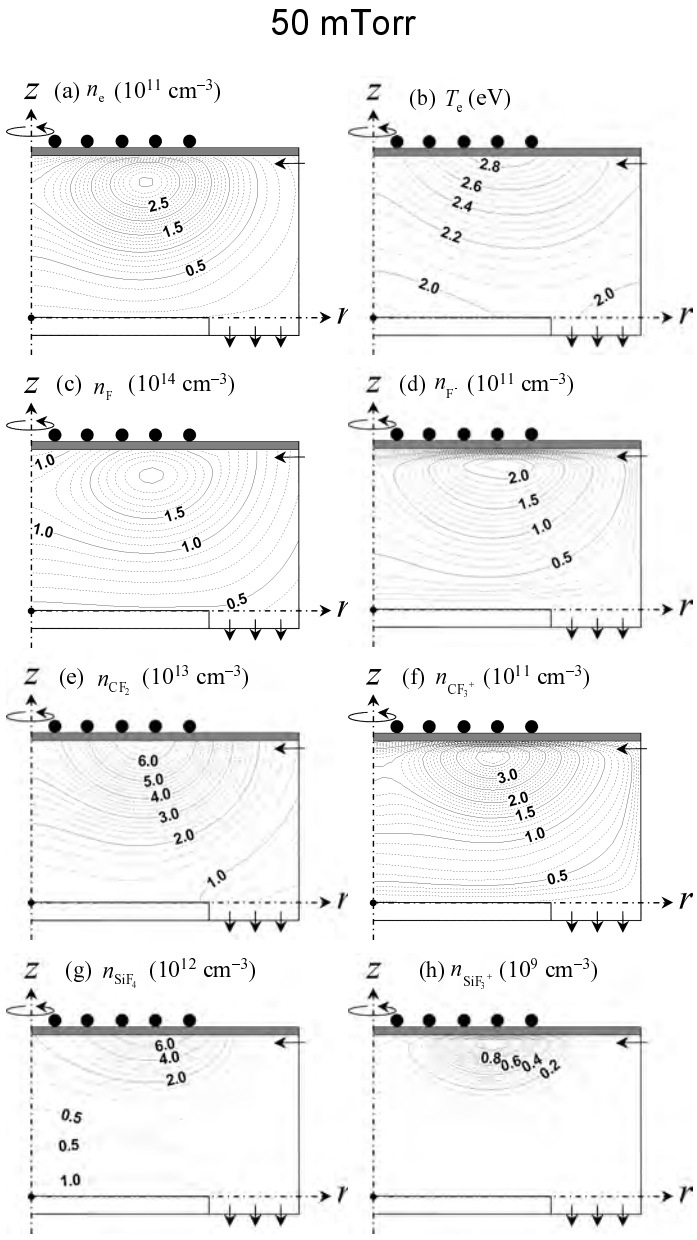

Fig. 2.8: Two-dimensional distributions of plasma properties in the reactor chamber for a higher pressure of 50 mTorr with the other parameters being the same as those under the standard conditions of Fig. 2.3: (a) electron density, (b) electron temperature, (c) F density, (d) F^- density, (e) CF_2 density, (f) CF_3^+ density, (g) SiF_4 density, and (h) SiF_3^+ density.

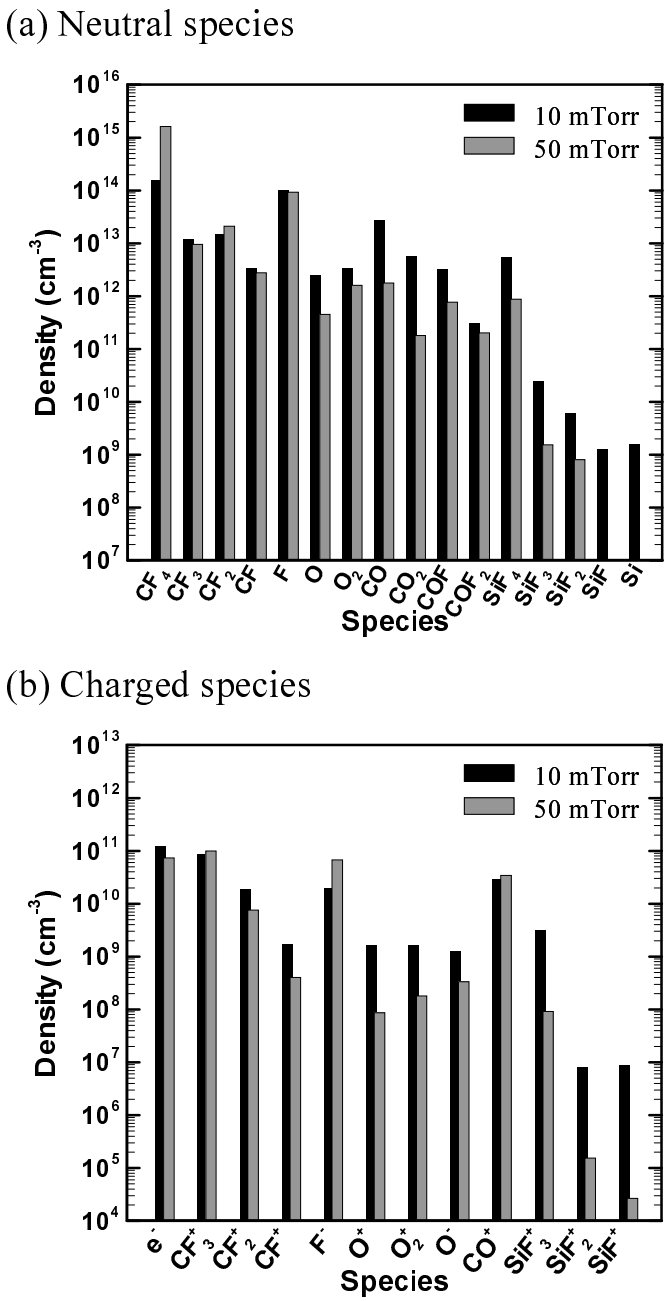

Fig. 2.9: Chemical compositions of (a) neutral and (b) charged species averaged over the entire region of the reactor chamber for different pressures of 10 (standard) and 50 mTorr. Note that the data for 10 mTorr are the same as those in the ”a wafer” case of Fig. 2.5.

2.4.3 Mass flow dependence

Figures 2.10(a)−2.10(h) show the two-dimensional distribution of plasma properties in the reactor chamber for a higher mass flow rate of 300 sccm, with the other parameters being the same as those under the standard conditions of Fig. 2.3. A comparison between Figs. 2.3 and 2.10 indicates that as a result of increased mass flow rate, or reduced gas residence time in the chamber, the densities of fragment neutrals and ions such as CF_2 and CF_3^+ are increased owing to reduced recombination loss at chamber walls, while the F atom density is slightly decreased. Moreover, the densities of etch product SiF_4 and product ion SiF_3^+ in the plasma are decreased owing to reduced residence time or increased exhaust velocity to maintain a constant pressure. In practice, the increase in the mass flow rate effectively decreases the amount of etch products in the reactor chamber. It is noted that the etch rate ER was slightly decreased to typically 0.41 μm/min for substrates, owing to the reduced density and thus the surface coverage of F atoms; on the other hand, the ER for the dielectric window remained almost unchanged at 0.28 μm/min.

Figures 2.11(a) and 2.11(b) show the chemical composition of neutral and charged species for different mass flow rates of 100, 200 (standard), and 300 sccm, averaged over the entire region of the reactor chamber. Note that the data for 200 sccm are the same as those in the "a wafer" case of Fig. 2.5. The densities of fluorocarbon radicals CF_x (x = 1−3) are larger for higher flow rates, while the densities of etch products such as O-containing species and SiF_x (x = 2−4) are smaller for higher flow rates. Correspondingly, the densities of fluorocarbon ions CF_x^+ (x = 1−3) are larger, and the densities of product ions such as O-containing ions and SiF_x^+ (x = 1−3) are smaller for higher flow rates.

2.4.4 Coil configurations

Figure 2.12(a) and 2.12(b) show the two-dimensional distribution of electron and SiF_4 densities in the reactor chamber for three different ICP coil configurations, with the other parameters being the same as those under the standard conditions of Fig. 2.3: (i) standard coil configuration as used for the aforementioned analysis, (ii) inner coil configuration, and (iii) outer coil configuration. Note that the figures for (i) are the same as those in Fig. 2.3. The electron density distribution in all configurations has a peak in the central middle part of the chamber, and the

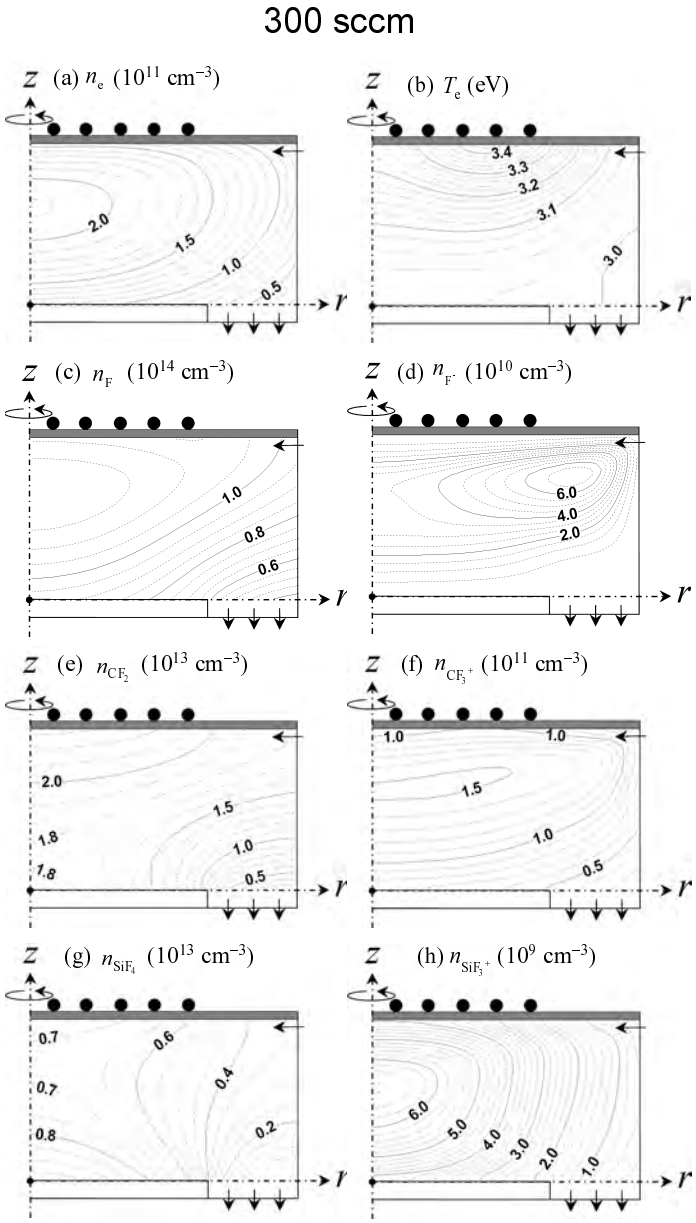

Fig. 2.10: Two-dimensional distributions of plasma properties in the reactor chamber for a higher mass flow rate of 300 sccm with the other parameters being the same as those under the standard conditions of Fig. 2.3: (a) electron density, (b) electron temperature, (c) F density, (d) F^- density, (e) CF_2 density, (f) CF_3^+ density, (g) SiF_4 density, and (h) SiF_3^+ density.

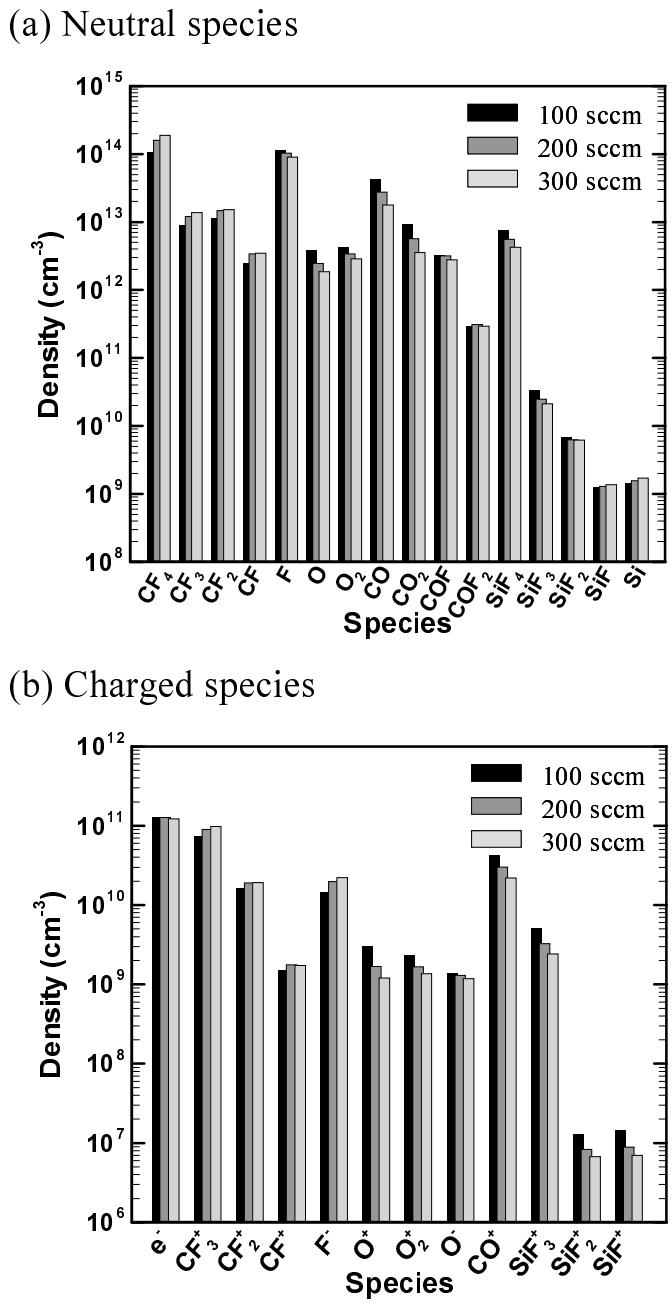

Fig. 2.11: Chemical compositions of (a) neutral and (b) charged species averaged over the entire region of the reactor chamber for different mass flow rates of 100, 200 (standard), and 300 sccm. Note that the data for 200 sccm are the same as those in ”a wafer” case of Fig. 2.3.

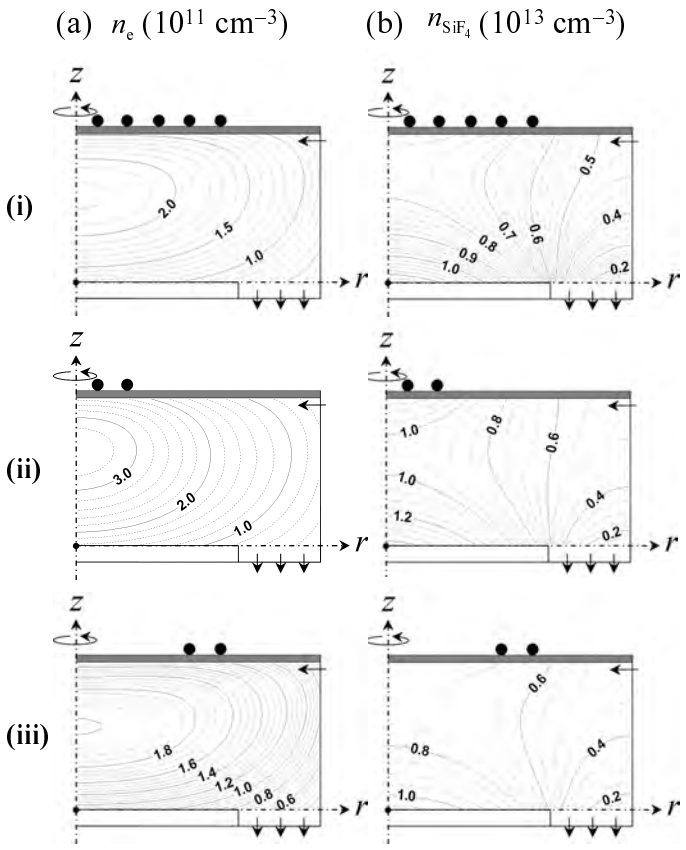

Fig. 2.12: Two-dimensional distributions of (a) electron and (b) SiF_4 densities in the reactor chamber for different ICP coil configurations: (i) standard, (ii) inner, and (iii) outer coil configurations. The other parameters are the same as those under the standard conditions of Fig. 2.3. Note that the figures for (i) are the same as those in Fig. 2.3.

density difference is attributed to the distance between the coil and reactor chamber walls which consume electrons as a result of diffusion. The electron density (and also temperature) in configuration (ii) is highest among the three, because the input power is absorbed in a limited area beneath the coil; on the other hand, in configuration (iii), the electrons generated in a region beneath the coil easily diffuse radially to chamber walls, and so the electron density is lowest among the three. The distribution of etch products is also affected by the coil configuration. The etch product SiF_4 originates primarily from substrate surfaces in configurations (i) and (iii), while originates from the SiO_2 dielectric window as well as substrate surfaces in configuration (ii). The etch rate uniformity of the substrates was found to be significantly better in (i) and (iii), as compared to that in (ii).

2.5 Conclusions

Two-dimensional fluid simulation of an ICP CF_4 plasma etching of SiO_2 has been performed taking into account gas-phase and surface chemistries of etch products as well as reactants during etching. The plasma fluid model consisted of Maxwell's equations, continuity equations for neutral and charged species including gas-phase and surface reactions, and an energy balance equation for electrons. The surface reaction model assumed Langumiur adsorption kinetics with the coverage of fluorine atoms, fluorocarbon radicals, and polymers on SiO_2 surfaces. In the simulation, we included 12 charged and 16 neutral species, together with 66 gas-phase reactions and 40 surface reactions (20 on metal chamber walls, and 20 on the SiO_2 dielectric window as well as the substrate surfaces). The steady-state solutions were obtained by coupling all these equations involving both fast and slow time-varying phenomena in a self-consistent manner.

The numerical results indicated that etch product species occupy a significant fraction of reactive ions as well as neutrals in the reactor chamber during etching, which in turn leads to a change of plasma and surface chemistry underlying the process. In practice, SiF_4 was the most abundant product species of silicon fluorides SiF_x, and its density was typically about 10% of that of the feedstock CF_4, which is comparable to that of the most abundant fluorocarbon radical CF_2; moreover, CO was the most abundant O-containing product species, and its density was much larger than that of SiF_4. Regarding product ions, SiF_3^+ was the most abundant among product SiF_x^+ ions, and its density was typically about 5% of that of the most abundant fluorocarbon ion CF_3^+; moreover, CO^+ was most abundant among O-containing product ions, and its density was much larger than that of SiF_3^+. The density and its distribution of such product species in the reactor chamber, together with those of fluorocarbon ions and neutrals, were changed by varying the ion bombardment energy on substrate surfaces, gas pressure, mass flow rate, and coil configuration, which arises in part from gas-phase reactions depending on plasma electron density and temperature. Surface reactions on the chamber walls and on the substrate also affect the density and distribution of product species in the reactor chamber; in particular, the surface reactions on the SiO_2 dielectric window as well as the substrate surfaces were found to largely affect the product density and distribution, depending on the plasma properties including the ion bombardment energy.

References

[1] H. Abe, M. Yoneda, and N. Fujiwara: Jpn. J. Appl. Phys. **47** (2008) 1435.

[2] M. Tuda, K. Ono, and K. Nishikawa: J. Vac. Sci. Technol. B **14** (1996) 3291.

[3] J. W. Coburn and H. F. Winters: J. Vac. Sci. Technol. **16** (1979) 391.

[4] E. M. Van Veldhuizen, T. Bisschops, E. J. W. van Vliembergen, and J. H. M. C van Wolput: J. Vac. Sci. Technol. A **3** (1985) 2205.

[5] J. A. O'Neill, J. Singh, and G. G. Gifford: J. Vac. Sci. Technol. A **8** (1990) 1716.

[6] K. Ono, M. Tuda, K. Nishikawa, T. Oomori, and K. Namba: Jpn. J. Appl. Phys. **33** (1994) 4424.

[7] K. Nishikawa, K. Ono, M. Tuda, T. Oomori, and K. Namba: Jpn. J. Appl. Phys. **34** (1995) 3731.

[8] K. Nishikawa, T. Oomori, and K. Ono: J. Vac. Sci. Technol. B **17** (1999) 127.

[9] G. Cunge, P. Chabert, J. P. Booth: Plasma Sources Sci. Technol. **6** (1997) 349.

[10] G. A. Hebner: J. Appl. Phys. **89** (2001) 900.

[11] G. A. Hebner: J. Appl. Phys. **90** (2001) 4938.

[12] M. V. V. S. Rao, S. P. Sharma, B. A. Cruden, and M. Meyyappan: Plasma Sources Sci. Technol. **11** (2002) 69.

[13] B. A. Cruden, M. V. V. S. Rao, S. P. Sharma, and M. Meyyappan: Plasma Sources Sci. Technol. **11** (2002) 77.

[14] J. Mostaghimi and M. Boulos: Plasma Chem. Plasma Process. **9** (1989) 25.

[15] S.-K. Park and D. J. Economou: J. Electrochem. Soc. **137** (1990) 2624.

[16] S.-K. Park and D. J. Economou: J. Electrochem. Soc. **138** (1991) 1499.

[17] X. Chen and E. Pfender: Plasma Chem. Plasma Process. **11** (1991) 103.

[18] D. B. Graves: IEEE Trans. Plasma Sci. **22** (1994) 31.

[19] P. L. G. Ventzek, R. J. Hoekstra, and M. J. Kushner: J. Vac. Sci. Technol. B **12** (1994) 461.

[20] P. L. G. Ventzek, M. Grapperhaus, and M. J. Kushner: J. Vac. Sci. Technol. B **12** (1994) 3118.

[21] K. A. Ashtiani, J. L. Shohet, W. N. G. Hitchon, G.-H. Kim, and N. Hershkowitz: J. Appl. Phys. **78** (1995) 2270.

[22] M.P. Hong and G. A. Emmett: J. Appl. Phys. **78** (1995) 6967.

[23] F. Y. Huang, H. H. Hwang, and M. J. Kushner: J. Vac. Sci. Technol. A **14** (1996) 562.

[24] R. J. Hoekstra and M. J. Kushner: J. Appl. Phys. **79** (1996) 2275.

[25] J. D. Bukowski, D. B. Graves, and P. Vitello: J. Appl. Phys. **80** (1996) 2614.

[26] T. Suekane, T. Taya, Y. Okuno, and K. Kabashima: IEEE Trans. Plasma Sci. **24** (1996) 1147.

[27] W. Z. Collison and M. J. Kushner: Appl. Phys. Lett. **68** (1996) 903.

[28] R. S. Wise, D. P. Lymberopoulos, and D. J. Economou: Appl. Phys. Lett. **68** (1996) 2499.

[29] M. J. Grapperhaus and M. J. Kushner: J. Appl. Phys. **81** (1997) 569.

[30] S. Rauf and M. J. Kushner: J. Appl. Phys. **81** (1997) 5966.

[31] M. J. Kushner: J. Appl. Phys. **82** (1997) 5312.

[32] R. J. Hoekstra, M. J. Grapperhaus, and M. J. Kushner: J. Vac. Sci. Technol. A **15** (1997) 1913.

[33] S. Rauf and M. J. Kushner: J. Appl. Phys. **83** (1998) 5087.

[34] W. Z. Collison, T. Q. Ni, and M. S. Barnes: J. Vac. Sci. Technol. A **16** (1998) 100.

[35] G. I. Font, I. D. Boyd, and J. Balakrishnan: J. Vac. Sci. Technol. A **16** (1998) 2057.

[36] E. Meeks, P. Ho, A. Ting, and R. J. Buss: J. Vac. Sci. Technol. A **16** (1998) 2227.

[37] K. Bera, B. Farouk, and Y. H. Lee: Plasma Sources Sci. Technol. **8** (1999) 412.

[38] K. Kamimura, K. Iyanagi, N. Nakano, and T. Makabe: Jpn. J. Appl. Phys. **38** (1999) 4429.

[39] J. P. Booth, G. Cunge, P. Chabert, and N. Sadeghi: J. Appl. Phys. **85** (1999) 3097.

[40] A. Fiala, M. Kiehlbauch, S. Mahnovski, and D. B. Graves: J. Appl. Phys. **86** (1999) 152.

[41] D. Zhang and M. J. Kushner: J. Appl. Phys. **87** (2000) 1060.

[42] K. Maeshige, M. Hasebe, Y. Yamaguchi, and T. Makabe: J. Appl. Phys. **88** (2000) 4518.

[43] R. Ye, P. Proulx, and M. I. Boulos: J. Phys. D: Appl. Phys. **33** (2000) 2145.

[44] D. Zhang and M. J. Kushner: J. Vac. Sci. Technol. A **18** (2000) 2661.

[45] H. C. Kim and V. I. Manousiouthakis: J. Vac. Sci. Technol. B **18** (2000) 841.

[46] H.-M. Wu: Plasma Sources Sci. Technol. **9** (2000) 347.

[47] D. J. Economou: Thin Solid Films **365** (2000) 348.

[48] B. Kim and S. Park: Chemometrics Intelligent Lab. Syst. **56** (2001) 39.

[49] D. Bernardi, V. Colombo, G. G. M. Coppa, and A. D'Angola: Eur. Phys. J. D **14** (2001) 337.

[50] K. Takechi and M. A. Lieberman: J. Appl. Phys. **90** (2001) 3205.

[51] T. Makabe and Z. Lj. Petrović: Appl. Surf. Sci. **192** (2002) 88.

[52] H. Nishiyama and M. Shigeta: Eur. Physl J. AP **18** (2002) 125.

[53] T. Panagopoulos, D. Kim, V. Midha, and J. Economou: J. Appl. Phys. **91** (2002) 2687.

[54] S. Xue, P. Proulx, and M. I. Boulos: J. Phys. D: Appl. Phys. **35** (2002) 1131.

[55] S. Rauf and P. L. G. Ventzek: J. Vac. Sci. Technol. A **20** (2002) 14.

[56] B. Ramamurthi and D. J. Economou: J. Vac. Sci. Technol. A **20** (2002) 467.

[57] S. Rauf, W. J. Dauksher, S. B. Clemens, and K. H. Smith: J. Vac. Sci. Technol. A **20** (2002) 1177.

[58] V. Sukharev: Vacuum **65** (2002) 281.

[59] M. W. Kiehlbauch: J. Vac. Sci. Technol. A **21** (2003) 116.

[60] S. Xue, P. Proulx, and M. I. Boulos: Plasma Chem. Plasma Process. **23** (2003) 245.

[61] A. V. Vasenkov and M. J. Kushner: J. Appl. Phys. **95** (2004) 834.

[62] A. V. Vasenkov, X. Li, G. S. Oehrlein, and M. J. Kushner: J. Vac. Sci. Technol. A **22** (2004) 511.

[63] A. Sankaran and M. J. Kushner: J. Vac. Sci. Technol. A **22** (2004) 1242.

[64] A. M. Efremov, S.-M. Koo, D.-P. Kim, K.-T. Kim, and C.-I. Kim: J. Vac. Sci. Technol. A **22** (2004) 2101.

[65] A. Agarwal and M. J. Kushner: J. Vac. Sci. Technol. A **23** (2005) 1440.

[66] S. Rauf, A. Haggag, M. Moosa, and P. L. G. Ventzek: J. Appl. Phys. **100** (2006) 023302.

[67] P. J. Stout, S. Rauf, R. D. Peters, and P. L. G. Ventzek: J. Vac. Sci. Technol. B **24** (2006) 1810.

[68] S. Tinck, W. Boullart, and A. Bogaerts: J. Phys. D: Appl. Phys. **41** (2008) 065207.

[69] A. Agarwal and M. J. Kushner: J. Vac. Sci. Technol. A **26** (2008) 498.

[70] C.-C. Hsu, J. Hoang, V. Le, and J. P. Chang: J. Vac. Sci. Technol. B **26** (2008) 1919.

[71] M. Bavafa, H. Ilati, and B. Rashidian: Semicond. Sci. Technol. **23** 2008 095023.

[72] Y. An, Y. Lu, D. Li, and Y. Chen: Sci. China Ser. E-Technol. Sci. **51** (2008) 674.

[73] A. Agarwal and M. J. Kushner: J. Vac. Sci. Technol. A **27** (2009) 37.

[74] D. P. Lymberopoulos and D. J. Economou: IEEE Trans. Plasma Sci. **23** (1995) 573.

[75] D. J. Economou, T. J. Bartel, R. S. Wise, and D. P. Lymberopoulos: IEEE Trans. Plasma Sci. **23** (1995) 581.

[76] K. Nanbu, T. Morimoto, and M. Suetani: IEEE Trans. Plasma Sci. **27** (1999) 1379.

[77] M. J. Kusuner, W. Z. Collison, M. J. Grapperhaus, J. P. Holland, and M. S. Barnes: J. Appl. Phys. **80** (1996) 1337.

[78] C. Lee, D. B. Graves, and M. A. Lieberman: Plasma Chem. Plasma Process. **16** (1996) 99.

[79] M. Schaepkens and G. S. Oehrlein: J. Electrochem. Soc. **148** (2001) C211.

[80] The International Technology Roadmap for Semiconductors 2008 Update at http://www.itrs.net/Links/2008ITRS/Update/2008_Update.pdf

[81] D. Edelson and D. L. Flamm: J. Appl. Phys. **56** (1984) 1522.

[82] K. Miyata, M. Hori, and T. Goto: J. Vac. Sci. Technol. A **14** (1996) 2343.

[83] H.-H. Doh, J.-H. Kim, S.-H. Lee, and K.-W. Whang: J. Vac. Sci. Technol. A **14** (1996) 2827.

[84] B. K. McMillin and M. R. Zachariah: J. Vac. Sci. Technol. A **15** (1997) 230.

[85] C. Suzuki, K. Sakaki, and K. Kadota: J. Vac. Sci. Technol. A **16** (1998) 2222.

[86] A. Bogaerts: J. Anal. At. Spectrom. **14** (1999) 1375.

[87] A. Armaou, J. Baker, and P. D. Christofides: Chem. Eng. Sci. **56** (2001) 1467.

[88] D. B. Hash, D. Bose, M. V. V. S. Rao, B. A. Cruden, M. Meyyappan, and S. P. Sharma: J. Appl. Phys. **90** (2001) 2148.

[89] S.-Y. So, A. Oda, H. Sugawara, and Y. Sakai: J. Phys. D: Appl. Phys. **34** (2001) 1919.

[90] S.-Y. So, A. Oda, H. Sugawara, and Y. Sakai: J. Phys. D: Appl. Phys. **35** (2002) 2978.

[91] A. M. Efremov, D. P. Kim, K. T. Kim, and C. I. Kim: Vacuum **75** (2004) 321.

[92] S. Dujko, R. D. White, K. F. Ness, Z. Lj. Petrović, and R. E. Robson: J. Phys. D: Appl. Phys. **39** (2006) 4788.

[93] V. Georgieva and A. Bogaerts: Phys. Rev. E **73** (2006) 036402.

[94] V. Georgieva and A. Bogaerts: Plasma Sources Sci. Technol. **15** (2006) 368.

[95] G. Cunge, R. Ramos, D. Vempaire, M. Touzeau, M. Neijbauer, and N. Sadeghi: J. Vac. Sci. Technol. A **27** (2009) 471.

[96] Z.-H. Bi, Z.-L. Dai, X. Xu, Z.-C. Li, and Y.-N. Wang: Phys. Plasmas **16** (2009) 043510.

[97] D. Zhang and M. J. Kushner: J. Vac. Sci. Technol. A **19** (2000) 524.

[98] M. L. Lieberman and A. J. Lichtenberg: *Principles of Plasma Discharge and Material Processing* (Wiley, 1994, New York) p. 93

[99] B. W. Yu and S. L. Girshick: J. Appl. Phys. **69** (1991) 656.

[100] P. Silvester: *Modern Electromagnetic Fields* (Prentice-Hall, 1968, Englewood Cliffs, NJ) p. 143.

[101] M. M. Turner: Phys. Rev.L **71** (1993) 1844.

[102] T. Kimura and K. Ohe: Plasma Sources Sci. Technol. **8** (1999) 553.

[103] E. Meeks and P. Ho: *Handbook of Advanced Plasma Processing Techniques* ed R J Shul and S J Pearton (Springer, 2000, New York) p. 99.

[104] M. W. Kiehlbauch and D. B. Graves: J. Appl. Phys. **89** (2001) 2047.

[105] T. Kimura, A. J. Lichtenberg, and M. A. Lieberman: Plasma Sources Sci. Technol. **10** (2001) 430.

[106] P. Ho, J. E. Johannes, R. J. Buss, and E. Meeks: J. Vac. Sci. Technol. A **19** (2001) 2344.

[107] S. F. Wong, M. J. W. Boness, and G. J. Schulz: Phys. Rev.L **31** (1973) 969.

[108] I. C. Plumb and K. R. Ryan: Plasma Chem. Plasma Process **6** (1986) 205.

[109] K. R. Ryan and I. C. Plumb: Plasma Chem. Plasma Process **6** (1986) 231.

[110] G. S. Oehrlein, Y. Zhang, D. Vender, and M. Haverlag: J. Vac. Sci. Technol. A **12** (1994) 323.

[111] G. S. Oehrlein, Y. Zhang, D. Vender, and M. Haverlag: J. Vac. Sci. Technol. A **12** (1994) 333.

[112] D. L. Flamm, C. J. Mogab, and E. R. Sklaver: J. Appl. Phys. **50** (1979) 6211.

[113] G. Fortuño: J. Vac. Sci. Technol. A **4** (1986) 744.

[114] N. Selamoglu, M. J. Rossi, and D. M. Golden: J. Chem. Phys. **84** (1986) 2400.

[115] M. Haverlag, G. M. W. Kroesen, C. J. H. de Zeeuw, Y. Creyghton, T. H. J. Bisschops, and F. J. de Hoog: J. Vac. Sci. Technol. B **7** (1989) 529.

[116] J. W. Butterbaugh, D. C. Gray, and H. H. Sawin: J. Vac. Sci. Technol. B **9** (1991) 1461.

[117] D. C. Gray, I. Tempermeister, and H. H. Sawin: J. Vac. Sci. Technol. B **11** (1993) 1243.

[118] J. P. Booth: Plasma Sources Sci. Technol. **8** (1999) 249.

[119] T. E. F. M. Standaert, C. Hedlund, E. A. Joseph, G. S. Oehrlein, and T. J. Dalton: J. Vac. Sci. Technol. A **22** (2004) 53.

[120] K. Ishikawa, M. Okigawa, Y. Ishikawa, S. Samukawa, and S. Yamasaki: Appl. Phys. Lett. **86** (2005) 264104.

[121] O. Kwon, B. Bai, and H. H. Sawin: J. Vac. Sci. Technol. A **24** (2006) 1920.

[122] C. Köhler and T. Frauenheim: Surf. Sci. **600** (2006) 453.

[123] R. Knizikevičius: Vacuum **82** (2008) 1191.

[124] E. Gogolides, P. Vauvert, G. Kokkoris, G. Turban, and A. G. Boudouvis: J. Appl. Phys. **88** (2000) 5570.

[125] G. J. Nienhuis, W. J. Gedheer, E. A. G. Hamers, W. G. J. H. M. van Sark, and J. Bezemer: J. Appl. Phys. **82** (1997) 2060.

[126] H. J. Yoon, T. H. Chung, C. J. Chung, and J. K. Lee: Thin Solid Films **506** (2006) 454.

[127] K. W. Morton and E. Süli: IMA J. Numer. Anal. **11** (1991) 241.

[128] C. W. Gear: Comm. ACM **14** (1971) 176.

[129] L. G. Christophorou, J. K. Olthoff, and M. V. V. S. Rao: J. Phys. Chem. Ref. Data **25** (1996) 1341.

Chapter 3

Plasma Etching Profile

3.1 Introduction

Plasma etching is widely employed in today's semiconductor manufacturing, which has contributed to progress in semiconductor industry. Much effort to improve the plasma etching technique has resulted in the scaling down of process dimensions, which in turn has improved semiconductor device performance. Further scaling down will continue to produce faster and smaller semiconductor devices. In practice, plasma etching forms circuit structures on substrates through a patterned mask, and the sectional profiles of the circuit structures are essential for device performance. One issue is critical dimension (CD) loss or gain, which is a pattern gap between the mask and etching profiles [1]. For example, the CD variation of gate electrodes, which closely affects the channel length of a transistor and thus device performance, has become increasingly important as integrated circuit device dimensions are scaled down to much less than 100 nm. Thus, a better understanding of plasma-surface interactions during etching continues to be important for the nanoscale control of etched profiles and CDs.

Etching profiles are affected by various factors during etching such as neutral and ion fluxes from plasma, mask patterns and materials, and bias voltage through the sheath. Boufnichel *et al.* investigated the effect of process parameters such as pressure, bias voltage, temperature, and gas flow rate on local bowing, by cryogenic etching with SF_6/O_2 inductively coupled plasmas

(ICP) [2]. They especially showed that local bowing depends on the trench passivation mechanism and on ion energy and density. Vyvoda *et al.* studied the effects of source and bias powers, pressure, and feed gas composition on the feature profiles of SiO_2-masked crystalline silicon etched in Cl_2/HBr transformer-coupled plasmas (TCP) [3]. They obtained higher etch rates at higher source powers, bias powers, and pressures. When HBr was used instead of Cl_2, etch rate decreased substantially, but the etch profile became more vertical and the trench bottom became flatter.

In recent years, etching profile simulation has contributed to the investigation of etching mechanisms, owing to improvement in computational performance. There are several methods of investigating plasma etching profiles [4–6]: string method [7–16], ray-tracing method [4, 17], cell removal method [4–6, 18–34], and level-set method [35–39]. Each method has both advantages and disadvantages. The string and ray-tracing methods are fast in computation and use surface-advancement algorithms, in which a mesh of connected points is used to represent the surface of the material during etching. However, surface-advancement algorithms poses difficulty in implementing calculations, and also present difficult algorithmic and geometrical problems in the treatment of boundaries or in the elimination of loops. In contrast, in the cell removal method, the volume of wafer to be simulated is described by dividing it into a matrix of small cells, which are removed depending on the local etch conditions. Increasing computing power now makes it possible to develop a three-dimensional profile simulator using the cell removal algorithm. The level set method views the moving front as a particular level set of a higher-dimensional function, where sharp gradients and cusps form naturally, and the effects of curvature can be easily incorporated. This method is highly robust for tracking interfaces moving with complex motions.

For the mask geometry, Kokkoris *et al.* calculated the neutral flux onto surfaces in two different structures, namely, a hole and a trench, indicating that the neutral flux is lower in a hole than in a trench of the same aspect ratio [40]. Dalvie *et al.* analyzed the feature profile evolution of a via and a trench exposed to three-dimensional-velocity ion fluxes, using the string method coupled with the Monte Carlo method for the plasma sheath. [41] They indicated that the etch rate is lower in a via than in a trench because of the larger geometrical constraint of via on ion trajectories.

There are several experimental studies of the difference in etching profile between holes and

trenches. Vyvoda *et al.* investigated Si etching profiles with oxide masks with geometrically different openings of a via and a trench in Cl_2 and HBr plasmas [3]. Their results showed that similar profiles are observed for via and trench bottoms, but that there are slight differences between nested vias and trenches in that in some cases (i.e., low pressure, high source power, and low bias power) microtrenching is less severe in vias, while in other cases the reverse is true. Chung investigated the reactive ion etching (RIE) lag for different feature dimensions of rectangles, squares, and circles/doughnuts during Si deep etching in ICPs with gases alternating between SF_6/O_2 and C_4F_8 [42]. Kiihamäki and Franssila reported that the RIE lag is related to pattern shape (square and circular holes, and trenches with variable aspect ratios) and size (from a few microns to over 100 μm) during Si etching in ICPs with SF_6 followed by the application of a short unbiased C_4F_8 passivation pulse [43]. Doemling *et al.* compared etch depth and profile between holes and trenches during SiO_2 etching in CHF_3 plasmas, showing that the inverse RIE lag was stronger in holes than in trenches [44].

A number of profile simulations have been developed not only for plasma etching but also for chemical vapor deposition (CVD) in terms of surface geometry [45–47]. IslamRaja *et al.* simulated the feature profile evolution of CVD in holes and trenches using a string algorithm in two dimensions, showing that the step coverage is higher in a trench than in a hole [45]. Here, step coverage was defined as the ratio of the deposited film thickness on sidewalls near the feature bottom to the thickness at the top surface. Coronell *et al.* also simulated the profile evolution of CVD using two geometrical models of a hole and a trench represented by discretized cells in two dimensions, showing similar step coverages [46]. These differences between a hole and a trench are clearly caused by stronger shadowing or geometrical restrictions in hole structures. Correspondingly, the geometrical effects of a mask pattern on processing characteristics such as RIE lag and step coverage should be considered more important from the point of view of circuit design, while the effects of aspect ratio have been considered important in a number of researches.

In this study, we present a profile simulation of SiO_2 etching in CF_4 plasmas, which is widely employed for the fabrication of trenches, vias, and contact holes. Attention was given on the effects of mask geometry to optimize mask patterning for the obtaining the etched profiles desired. In practice, silicon dioxide has been employed for interlayer insulating films owing to its low dielectric constant, and most SiO_2 etch processes use plasmas of fluorocarbon and

hydrofluorocarbon gases such as CF_4, C_2F_6, C_4F_8, and CHF_3 [23, 48]. F atoms are needed to react with Si to form the volatile product SiF_4, and C atoms are needed to combine with O atoms to form the volatile products CO, CO_2, and COF_2. The plasma etching of SiO_2 requires energetic ions as well as etchant neutrals, because ion bombardment stimulates the chemical reaction between deposited fluorocarbon polymers and oxide surfaces, by breaking strong Si-O bonds (7.9 eV) [27, 49, 50]. The predominant ion is pressumed to be CF_3^+ in CF_4 plasmas, where the relative abundance of CF_3^+, CF_2^+, and CF^+ depends on feed gas density as well as on plasma electron density and temperature [51]. To investigate the role of mask geometry on etched profiles such as undercut, bowing, and RIE lag, profile evolution was simulated using the Monte Carlo and cell removal methods. The model is described in § 3.2, and the numerical results of the etched feature profiles are presented in § 3.3. Finally, the conclusions are given in § 3.4.

3.2 Model

We consider two structures of an axisymmetric circular hole and an infinitely long rectangular trench in two dimensions, as shown in Fig. 3.1. The simulation domain is a several-hundreds-of-nanometer region containing plasma and substrate surfaces. The profiles are represented by two-dimensional coordinates (r, z) for the hole and (x, z) for the trench. The substrate surfaces have two layers: the upper layer for the resist mask and the lower for SiO_2 to be etched. Particle trajectories are tracked through a three-dimensional position and a three-dimensional velocity.

The model for etching profile evolution consists of four modules: a particle injection module outside microstructures where ions and neutrals are injected from the plasma through the sheath, a particle transport module inside microstructures where ions and neutrals are transported from the top boundary of the simulation domain to feature surfaces, a surface reaction module of the SiO_2 layer, and a surface evolution module. The injection module calculates the flux of ions and neutrals using parameters such as species density and temperature obtained from plasma simulation. The transport module calculates the flux of ions and neutrals transported inside microstructures onto surfaces, including the incident angle thereon. Then, the surface reaction module treats the interactions between incident ions and neutrals and surface compounds (SiO_2 layer consisting of SiO_2 and the polymer deposited). The Monte Carlo ap-

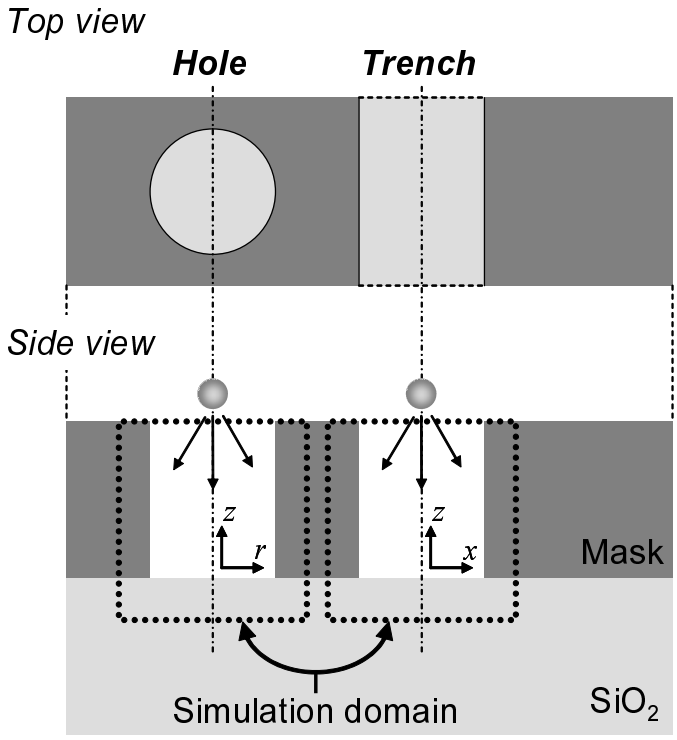

Fig. 3.1: Schematic of the simulation domain.

proach allows chemical and physical mechanisms with probabilistic considerations, taking into account neutral adsorption, spontaneous chemical etching, and sputtering on SiO_2 surfaces, together with specular reflection of ions and diffusive reflection of neutrals on mask surfaces. All these mechanisms play an important role in profile evolution. [9, 20, 52]

Figure 3.2 shows the flowchart of the simulation. Firstly, newly injected particles from the plasma are characterized by their own initial positions and velocities. Secondly, all particles in the simulation domain move at their own velocities every small time step Δt. If a particle reaches surfaces, it is discriminated from other particles in the domain to calculate the surface reaction. Finally, SiO_2 layer surfaces evolve as a result of surface reactions. The procedures are repeated during the calculation. We now exclude the evolution of a resist mask and charging effects on feature surfaces, because we are interested in pure geometrical effects in plasma-surface interactions as a first step. However, charging has become an important issue in the present plasma processing, particularly the charging potential deflecting ion trajectories to cause profile irregularities [26]. We are now developing a new version of the simulation including charging as well as geometrical effects on plasma etching, which will soon be reported.

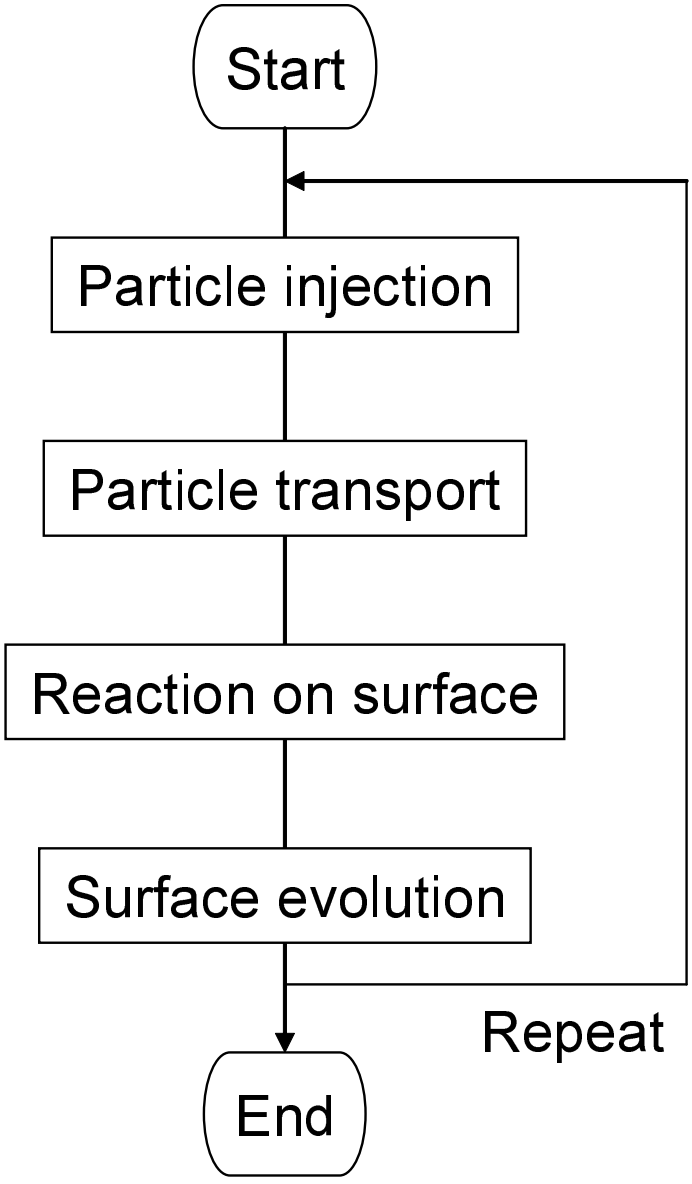

Fig. 3.2: Flowchart of the simulation.

Table I: Densities of seven chemical species in the plasma.

Ion	Density (m^{-3})	Neutral	Density (m^{-3})
CF^+	5.49×10^{14}	F	9.70×10^{19}
CF_2^+	1.31×10^{16}	CF	1.24×10^{18}
CF_3^+	1.34×10^{17}	CF_2	1.61×10^{19}
		CF_3	1.83×10^{19}

3.2.1 Plasma conditions and particle transport

Silicon dioxide etching in fluorocarbon plasmas involves a number of chemical species, which result in complicated gas-phase and surface reactions. Since all these reactions are difficult to treat in the simulation, several important ones are selected in the model. We assume fluorocarbon plasmas containing seven species (i.e., CF_3^+, CF_2^+, CF^+, CF_3, CF_2, CF, and F), as listed in Table I. The respective densities in the plasma were taken from our gas-phase calculations of ICP CF_4 plasmas at 10 mTorr and 250 W, where the electron density and temperature were $n_e = 1.0 \times 10^{11}$ cm^{-3} and $T_e = 3$ eV, respectively [53,54]. The ions are assumed to be in thermal equilibrium at $T_i = 0.5$ eV, and the neutrals at $T_n = 0.05$ eV in the plasma.

The species originating from the plasma are injected from the top boundary of the simulation domain, where the particles are randomly located, being transported in microstructures onto feature surfaces. Here, particle simulation is employed on the basis of successively injected multi-particle trajectories with three velocity components (v_x, v_y, v_z). The velocity distribution of injected particles is assumed to be anisotropic for ions, while isotropic for neutrals. The particles travel straight towards feature surfaces by reflecting on mask sidewalls with a given probability γ, and thus adsorbing thereon with a probability $(1 - \gamma)$. The reflection is assumed to be specular for ions, while diffusive for neutrals at a surface temperature of 300 K [15].

The ion flux Γ_i is given by [55]

$$\Gamma_i = n_s u_B = 0.61 n_0 u_B, \tag{3.1}$$

where n_s is the plasma density at the sheath edge, $u_B = \sqrt{kT_e/M_i}$ the Bohm velocity, k the Boltzmann constant, M_i the mass of ion, and n_0 the bulk plasma density. Ions acquire their own kinetic energy after being accelerated through the sheath between the plasma and substrate

surfaces; the resulting energetic ions have their own thermal energy plus a given bias voltage. The neutral flux Γ_n is given by [55]

$$\Gamma_n = \frac{1}{4} n_n v_n, \tag{3.2}$$

where n_n is the neutral density of the plasma and v_n the thermal velocity of neutrals. The particle velocity is defined in three dimensions at the top boundary, where particles are injected into the simulation domain. The velocity (v_x, v_y, v_z) for neutrals is given as [56]

$$v_x = \sqrt{-\frac{2kT_n \ln \xi_1}{M_n}} \cos 2\pi\xi_2, \tag{3.3}$$

$$v_y = \sqrt{-\frac{2kT_n \ln \xi_1}{M_n}} \sin 2\pi\xi_2, \tag{3.4}$$

$$v_z = -\sqrt{-\frac{2kT_n \ln \xi_3}{M_n}} \sin \pi\xi_4, \tag{3.5}$$

where $M_n (= M_i)$ is the mass of neutrals, and ξ_1, ξ_2, ξ_3, and ξ_4 are random numbers between 0 and 1 independent of each other.

For weakly ionized plasmas used in plasma etching, the average motion of ions in the sheath can be described in terms of a constant drift velocity along the direction of the sheath electric field. In practice, ions are accelerated by the electric field through the sheath, to gain an energy corresponding to the potential difference between the bulk plasma and substrate surfaces. Thus, assuming a collisionless sheath, the velocity component for ions in the z-axis or the direction normal to the substrate surface at the injection boundary is modified as [57]

$$v_z = -\sqrt{-\frac{2kT_i \ln \xi_3}{M_i} \sin^2 \pi\xi_4 + \frac{2e(\phi_p - \phi_s)}{M_i}}, \tag{3.6}$$

where e is the elementary charge, ϕ_p the plasma potential, and ϕ_s the surface potential. We consider the potential difference $\phi_p - \phi_s$ as the ion energy E_i under the condition of $E_i \gg kT_i$. Figure 3.3 shows the x-axis component of the angular distribution of ions at the injection boundary for different values of E_i = 50, 100, 200, 400, and 800 eV. The velocity distribution of ions is anisotropic after the ions were accelerated through the sheath, and most part of the distribution ranges between ±10°. A larger ion energy E_i gives a sharper distribution, which in turn gives anisotropic etching. Here, the incident angle θ and its x-axis component θ_x are defined as shown in Fig. 3.4, where θ takes values from 0 to 90°, and θ_x takes values from −90 to 90°.

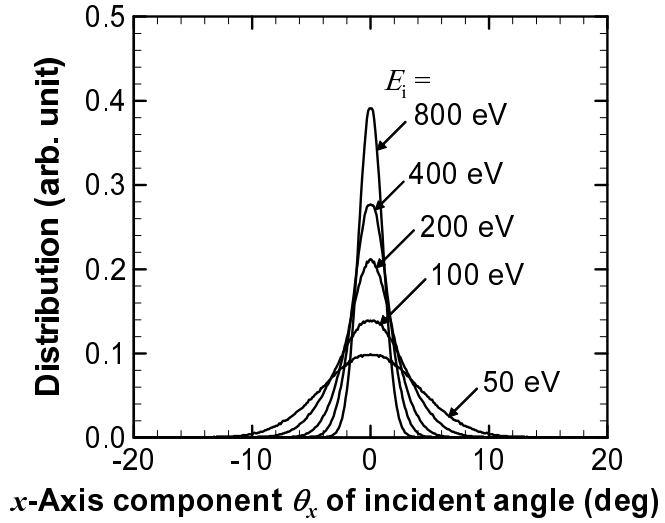

Fig. 3.3: Definition of the incident angle θ and its x-axis component θ_x.

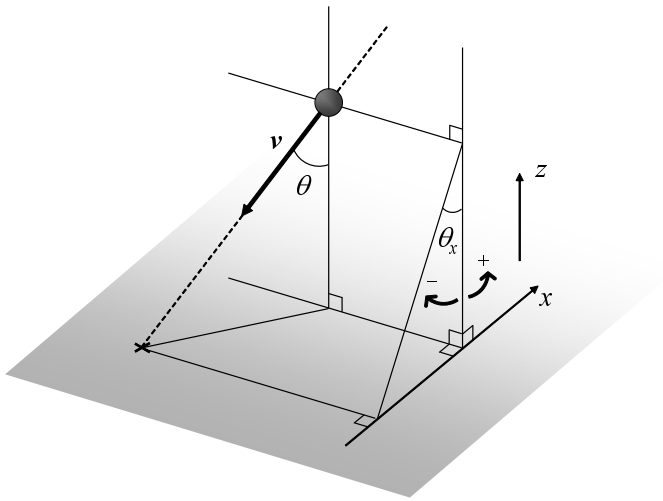

Fig. 3.4: Definition of the incident angle θ and its x-axis component θ_x.

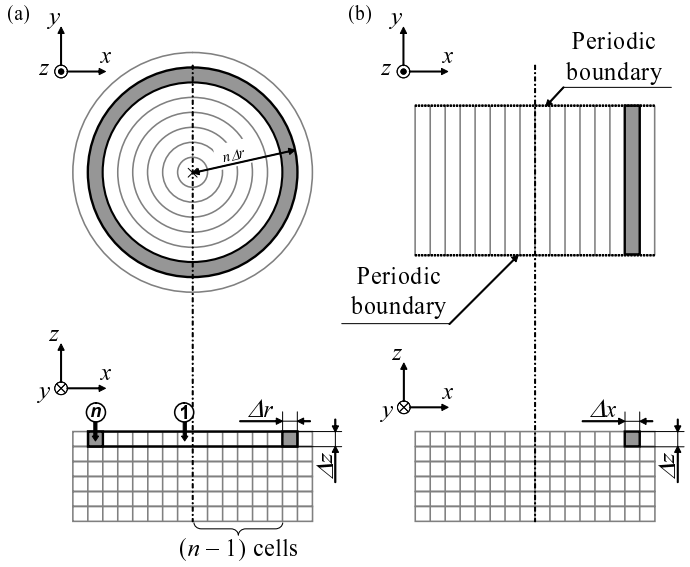

Fig. 3.5: Schematic of the cell structure for the SiO_2 layer to be etched: (a) rectangular doughnut ring for the hole and (b) infinitely long rectangular parallelepiped for the trench.

3.2.2 Surface representation

We employ two-dimensional cell removal method for representing the difference in geometrical effects on etching profiles between a hole and a trench. The SiO_2 layer being etched is represented by a number of two-dimensional cells, each of which is a rectangular doughnut ring for the hole and an infinitely long rectangular parallelepiped for the trench, as shown in Figs. 3.5(a) and 3.5(b), respectively. In the hole model, the section of each cell is rectangular with an area $\Delta r \times \Delta z$, and the nth cell from the center axis has an inner radius of $(n-1)\Delta r$ and an outer radius of $n\Delta r$. On the other hand, in the trench model, the cells employed are all the same with the section of each cell being rectangular with an area $\Delta x \times \Delta z$. The cell volume is $v_{\text{cell}} = (2n-1)\pi(\Delta r)^2\Delta z$ for the nth cell in a hole, and $v_{\text{cell}} = \Delta x \Delta y \Delta z$ for all the cells in trench. The parameters taken in the present calculation are $\Delta x = \Delta r = 1$ nm, $\Delta z = 5$ nm, and $\Delta y = 60$ nm.

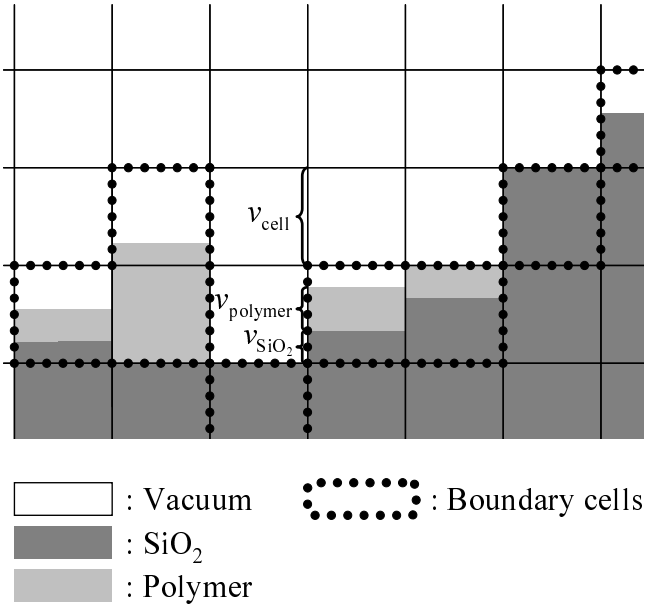

Fig. 3.6: Schematic of the SiO_2-layer cell consisting of three components: ”Vacuum”, ”SiO_2”, and ”Polymer”.

Figure 3.6 shows a schematic of the cell of SiO_2 layer. The volume of a cell is taken to be separated into three components, namely, "Vacuum", "SiO_2", and "Polymer", and the sum of the respective volumes is given by $v_{\text{cell}} = v_{\text{Vacuum}} + v_{\text{SiO}_2} + v_{\text{Polymer}}$. "Vacuum" indicates an empty space, "SiO_2" a space occupied only by SiO_2, and "Polymer" a space occupied by the polymer deposited consisting of carbon, fluorine, silicon, and oxygen. The cells neighboring the vacuum or empty cell are defined as boundary cells, which are cells on the uppermost surfaces being etched. The polymer surface coverage is defined thereat as

$$\alpha = \frac{v_{\text{Polymer}}}{v_{\text{SiO}_2} + v_{\text{Polymer}}}. \tag{3.7}$$

At the beginning of the calculation, all the cells are solid "SiO_2".

3.2.3 Surface reactions

The particles injected into the simulation domain strike either the mask or SiO_2-layer surfaces. On the mask surfaces, as mentioned earlier, all incident species of ions and neutrals are assumed to reflect thereon with a probability γ, where no etching or deposition is assumed to occur. We treat the reflection probability γ on the mask surfaces as a given parameter, and the particles adsorbed on mask surfaces with a probability $(1 - \gamma)$ are removed from the simulation domain.

On SiO_2 layer surfaces, all incident species are assumed to react with SiO_2 or polymer on the surface without reflection. Table II shows chemical reactions on SiO_2 layer surfaces which are incorporated in the model [27,58]. The reactions depend on incident species and the surface composition of SiO_2 or the polymer. Incident ions ($CF_x^+ : x = 1 - 3$) have two kinds of reaction processes: etching or sputtering and direct ion deposition. The sputtering or deposition yield Y is a function of ion incident energy E_{i} and angle θ [59]:

$$Y(E_{\text{i}}, \theta) = \begin{cases} A_1(\sqrt{E_{\text{i}}} - \sqrt{E_{\text{th}}})f(\theta) & E_{\text{th}} < E_{\text{i}}, \\ A_1(\sqrt{E_{\text{i}}} - \sqrt{E_{\text{th}}}) & \frac{1}{2}E_{\text{th}} < E_{\text{i}} \le E_{\text{th}}, \\ -A_2\sqrt{E_{\text{i}}} & 0 < E_{\text{i}} \le \frac{1}{2}E_{\text{th}}, \end{cases} \tag{3.8}$$

where A_1 and A_2 are coefficients of sputtering and deposition, respectively, and E_{th} is the sputtering threshold energy [60]. The function $f(\theta)$ is given by

$$f(\theta) = \begin{cases} 1 & \theta \le \theta_{\text{cr}}, \\ \dfrac{\cos\theta}{\cos\theta_{\text{cr}}} & \theta > \theta_{\text{cr}}, \end{cases} \tag{3.9}$$

Table II: Reactions on SiO_2 layer surfaces.

Reaction	Incident species	Surface	Process
(1) O_2 −Si* → Si(g) + 2O(g) + O_2−Si* ($E_i \geq E_{th}$)	CF_x^+	SiO_2	Physical sputtering
(2) polymer → sputtering of polymer ($E_i \geq E_{th}$)	CF_x^+	polymer	Physical sputtering
(3) CF_x^+(g) → polymer(s) ($E_i < E_{th}$)	CF_x^+	SiO_2 or polymer	Deposition
(4) CF_x → polymer	CF_x	SiO_2 or polymer	Deposition
(5) 2F(g) + O_2− Si *(s) → O_2−Si−F_2(s)	F	SiO_2	Adsorption
(6) 2F(g) + O_2−Si−F_2(s) → Si−F_4(g) + O_2(g) + O_2−Si*	F	SiO_2	Chemical etching
(7) F(g) + polymer(s) → etching of polymer	F	polymer	Chemical etching

E_i: ion energy, E_{th}: sputtering threshold energy,

g: gas phase, s: solid, *: a dangling bond or a site for chemisorption.

where $\theta_{cr} = 45°$ is a critical incident angle [33, 34]. Note that the yield Y indicates etching ($Y > 0$) at $E_i > E_{th}$ and deposition ($Y < 0$) at $E_i < E_{th}$, and that the yield Y for deposition has a peak (a negative peak) at $E_i = 1/2E_{th}$. The coefficients A_1 and A_2 and the threshold energy E_{th} are listed in Table III, which are cited from the surface model of Gogolides *et al.* [59]. In general, the effect of etching on sputtering yield for a polymer remains unknown but is expected to depend on the type of polymer, because the reactions of a polymer are difficult to identify owing to its complex constituents. Thus, we assumed the ion sputtering yield for SiO_2 to be the same as the sputtering yield for a polymer, as Gogolides *et al*. did in their simulation of plasma-surface interactions [59]. In practice, SiO_2 and a polymer in a cell are simultaneously sputtered, where the sputtered volumes of SiO_2 and the polymer are determined from their occupation of the cell.

Incident CF_x (x=1−3) radicals result in deposition on SiO_2 layer surfaces, with a reaction probability of unity on both surface compositions of SiO_2 and a polymer. On the other hand, incident F atoms have three reaction paths: adsorption on the surface composition of SiO_2, and chemical etchings on compositions of SiO_2 and a polymer, where the respective reaction

Table III: Coefficients A_1 and A_2 for sputtering and deposition, and the sputtering threshold energy E_{th} of fluorocarbon ions on SiO_2 and polymer.

Ion	A_1	A_2	E_{th} (eV)	Ref.
CF^+	0.0456	0.0189	20	59
CF_2^+	0.0306	0.0127	80	59
CF_3^+	0.0228	0.0094	150	59

probabilities are taken to be 0.1, 0.9, and 1.0, respectively [58, 61] When a polymer is etched with F atoms, it volatilizes from the surface as CF_4, because a polymer consists primarily of fluorocarbons.

3.3 Results and Discussion

We simulate etching profiles by varying several parameters, including the incident flux and angular distribution of ions and neutrals onto feature surfaces. The following are chosen as standard conditions: an ion energy $E_i = 200$ eV, a mask pattern diameter/width $D/W = 20$ nm, a mask height $H = 100$ nm, and a reflection probability $\gamma = 0.5$ on mask surfaces for all plasma species of ions and neutrals. It is assumed that on mask surfaces, incident ions reflect specularly and neutrals reflect thermally or randomly, as mentioned earlier.

3.3.1 Ion energy

Figures 3.7(a) and 3.7(b) show the feature profile evolutions of a hole and a trench during etching, respectively, simulated for different values of $E_i = 200$, 400, and 800 eV with $D/W = 20$ nm, $H = 100$ nm, and $\gamma = 0.5$. Each curve represents the evolving interfaces obtained every 60 s. By comparing the two structures, the etched depth is larger for the trench, and the bowing or lateral etch on sidewalls is also more significant for the trench. In both structures, the etched depth is larger, or the etch rate is higher, at higher E_i, owing to increased etching or sputtering yield.

Figures 3.8(a) and 3.8(b) show the distributions of CF_3 radical and CF_3^+ ion fluxes incident to the mask sidewalls and bottom SiO_2 surfaces for the hole and trench, respectively, calculated

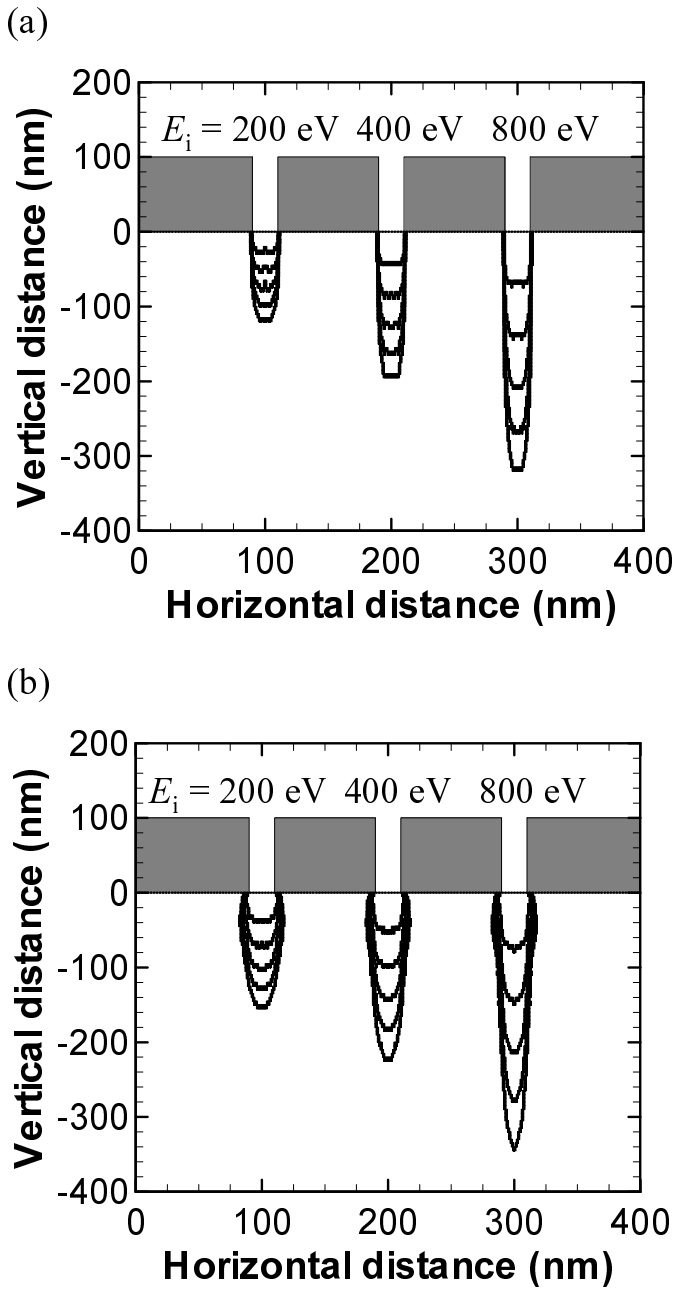

Fig. 3.7: Feature profile evolutions of the (a) hole and (b) trench during etching, simulated for different ion energies E_i = 200, 400, and 800 eV. The other conditions are D/W = 20 nm, H = 100 nm, and γ = 0.5. Each curve represents the evolving interfaces obtained every 60 s.

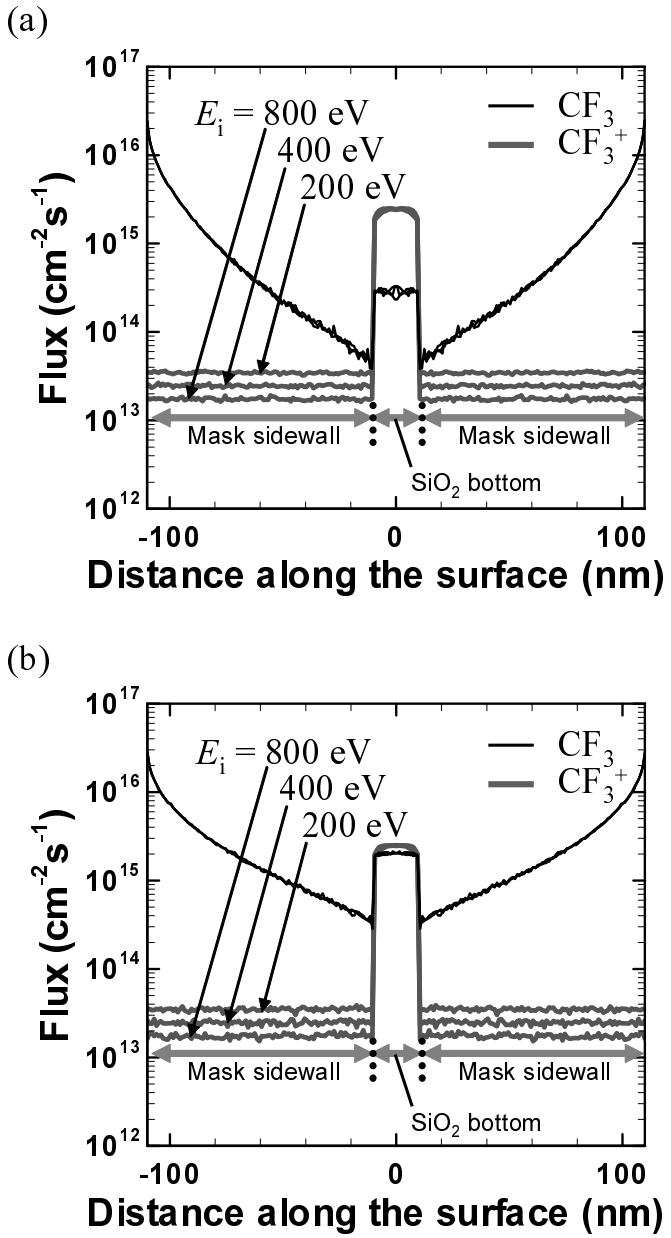

Fig. 3.8: Distributions of CF_3 radical and CF_3^+ ion fluxes incident to mask sidewalls and bottom SiO_2 surfaces for the (a) hole and (b) trench, calculated under the same conditions of Fig. 3.7.

under the same conditions shown in Fig. 3.7. By comparing the two structures, the neutral flux is larger in the trench than in the hole; in particular, on bottom surfaces and mask sidewalls near the bottom, the neutral flux in the trench is about ten times larger than that in the hole. On the other hand, the ion fluxes are almost the same in both structures. Therefore, the profile differences between the hole and trench in Fig. 3.7 come from the geometrical shadowing effects of the structure for neutrals, which are more severe for the hole than for the trench. In both structures, the neutral flux onto bottom surfaces and sidewalls remains almost the same under different values of E_{i}, assuming no collisions between ions and neutrals in the sheath. On the other hand, the ion flux onto bottom surfaces remains almost the same under different values of E_{i}, while the ion flux onto mask sidewalls decreases by about 1.5 times with the doubling of E_{i}, owing to the increased anisotropy of the ion velocity distribution. The ion flux incident on bottom surfaces almost equals that injected at the top boundary.

3.3.2 Mask pattern size

Figures 3.9(a) and 3.9(b) show the feature profile evolutions of the hole and trench during etching, respectively, simulated for different values of D/W = 20, 30, 40, and 50 nm with E_{i} = 200 eV, H = 100 nm, and γ = 0.5. Each curve also represents the evolving interfaces every 60 s. By comparing the two structures, the etched depth is larger, and the bowing or lateral etch is more significant for the trench, as in Fig. 3.7. In both structures, the etched depth decreases with decreasing mask pattern size D/W, or RIE lag occurs; in practice, the decrease with decreasing D/W is more remarkable, or the degree of the RIE lag is larger, for the trench than for the hole. Moreover, the bowing or lateral etch on sidewalls is also reduced with decreasing D/W, which is also more significant for the trench than for the hole. These differences also come from the geometrical shadowing effects of the structure for neutrals, which are more severe for smaller mask patterns, as can be seen below. Kiihamäki *et al.* investigated the etch depths of a hole and a trench, which decreased with decreasing D/W [43]; they found that the etch depth was larger in the trench than in the hole for similar values of D/W. Thus, our results are in good agreement with their experimental results.

Figures 3.10(a) and 3.10(b) show the distributions of the CF_3 radical and CF_3^+ ion fluxes incident on mask sidewalls and bottom SiO_2 surfaces for the hole and trench, respectively, calculated under the same conditions shown in Fig. 3.9. By comparing the two structures, the

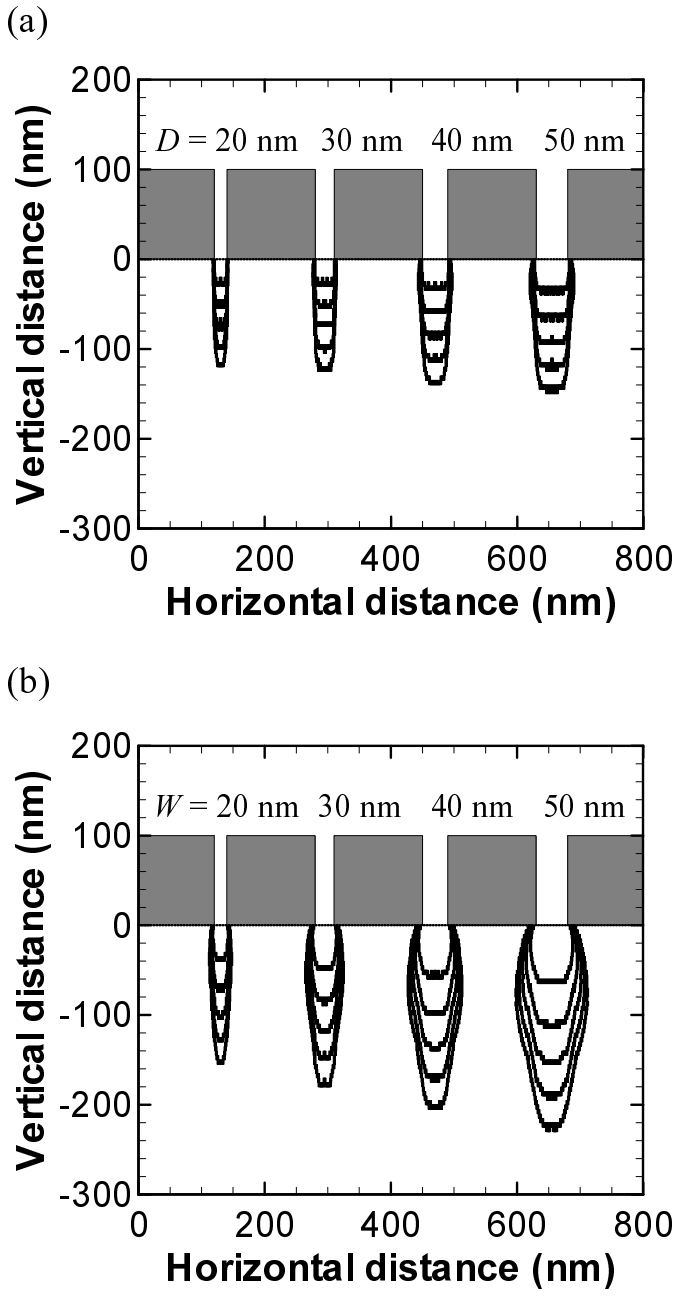

Fig. 3.9: Feature profile evolutions of the (a) hole and (b) trench during etching, simulated for different mask pattern diameters/widths D/W = 20, 30, 40, and 50 nm. The other conditions are H = 100 nm, E_i = 200 eV, and γ = 0.5. Each curve represents the evolving interfaces obtained every 60 s.

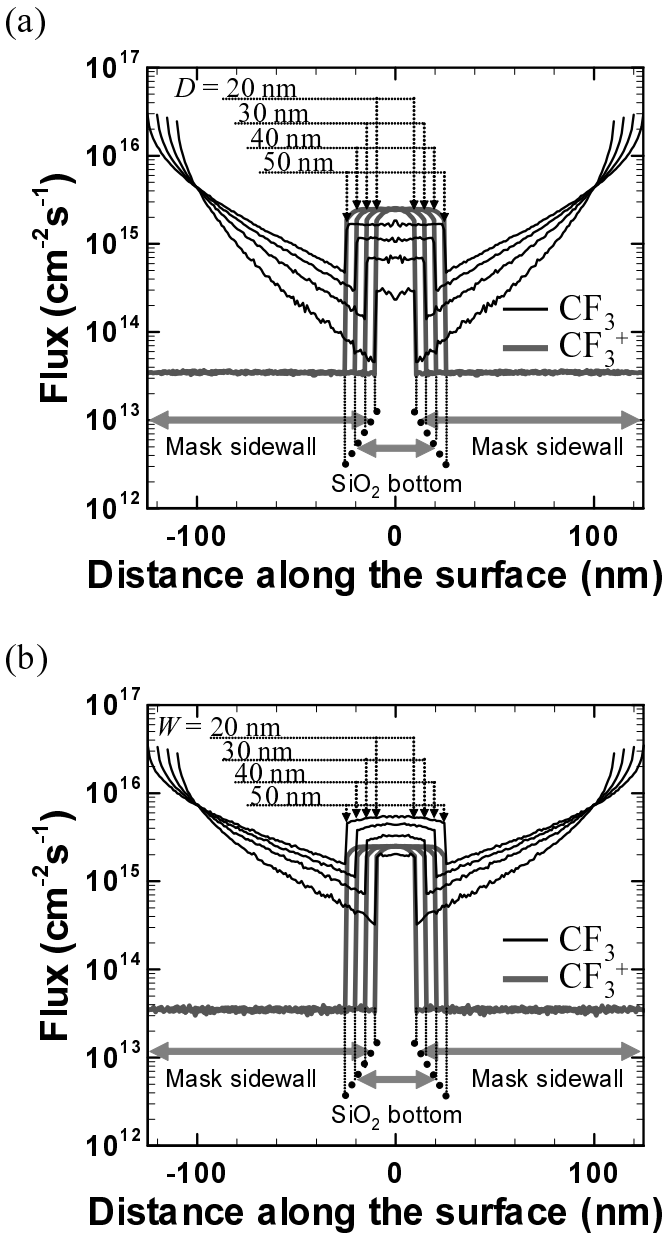

Fig. 3.10: Distributions of CF_3 radical and CF_3^+ ion fluxes incident to mask sidewalls and bottom SiO_2 surfaces for the (a) hole and (b) trench, calculated under the same conditions shown in Fig. 3.9.

neutral flux is larger in the trench than in the hole, while the ion fluxes are almost the same, as in Fig. 3.8. In both structures, the neutral flux onto bottom surfaces and sidewalls is smaller for smaller D/W, while the ion flux onto bottom surfaces and sidewalls remains almost the same for different D/W values. Thus, the neutral-to-ion flux ratio is smaller in the hole than in the trench, and is also smaller for smaller D/W, which results in a higher anisotropy of the etching profile for a hole and for a smaller pattern size D/W, as shown in Fig. 3.9. In practice, the neutral-to-ion flux ratios on bottom surfaces are > 1 in the trench and < 1 in the hole; moreover, in the case of a small $D = 20$ nm of the hole, the neutral-to-ion flux ratio on bottom surfaces is < 0.1, where the etching starves for neutrals and thus is determined primarily by incident ion flux. It is further noted that the larger degree of RIE lag for the trench is ascribed to the decrease in neutral flux onto bottom surfaces with decreasing D/W, which affects etching more significantly for the trench owing to the neutral-to-ion flux ratio being > 1.

3.3.3 Mask height

The etching profile can be controlled by changing the mask pattern diameter/width D/W, as mentioned above. However, pattern size is usually determined by circuit design requirements, and so the mask pattern size D/W is inflexible as an option for controlling etching profile. Thus, the mask height H can be an option for controlling the profile.

Figures 3.11(a) and 3.11(b) show the feature profile evolutions of the hole and trench during etching, respectively, simulated for different values of $H = 50$, 100, 200, and 400 nm with $E_i = 200$ eV, $D/W = 20$ nm, and $\gamma = 0.5$. Each curve also represents the evolving interfaces every 60 s. In both structures, etched depth and the rate of bowing or lateral etch significantly decrease with increasing mask height H, especially in the trench, which is ascribed to the geometrical shadowing effects of the structure for ions as well as for neutrals, which are more severe for greater mask heights. Figure 3.12 shows the normalized flux Γ/Γ_0 of CF_3 radicals and CF_3^+ ions as a function of H for the hole and trench, calculated under the same conditions shown in Fig. 3.11. Here, Γ is the flux incident to bottom SiO_2 surfaces and Γ_0 is the flux injected at the top boundary. Neutral flux decreases substantially with increasing H in both structures, and even ion flux decreases almost linearly with increasing H.

Figures 3.13(a) and 3.13(b) show the angular distributions of the CF_3 radical flux incident to bottom SiO_2 surfaces for the hole and trench with different mask heights H, respectively, cal-

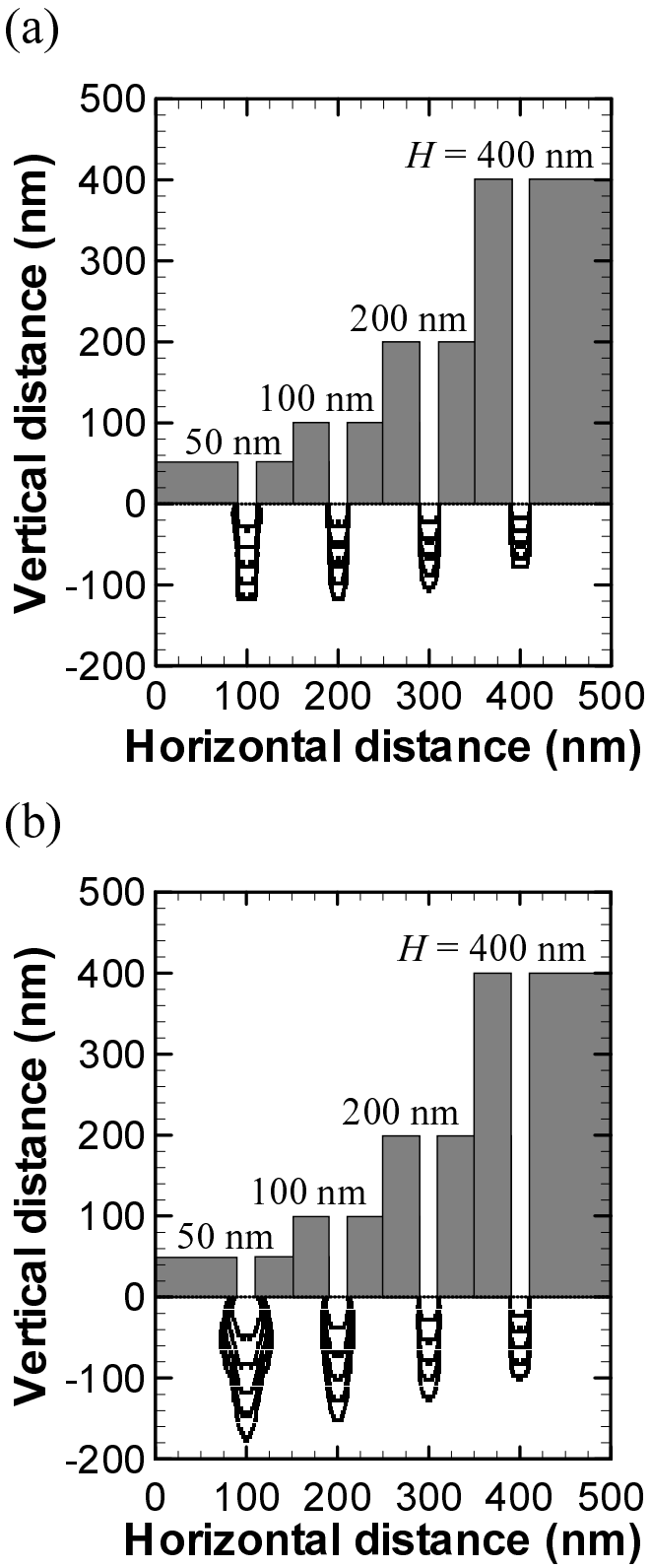

Fig. 3.11: Feature profile evolutions of the (a) hole and (b) trench during etching, simulated for different mask heights H = 50, 100, 200, and 400 nm. The other conditions are D/W = 20 nm, E_i = 200 eV, and γ = 0.5. Each curve represents the evolving interfaces obtained every 60 s.

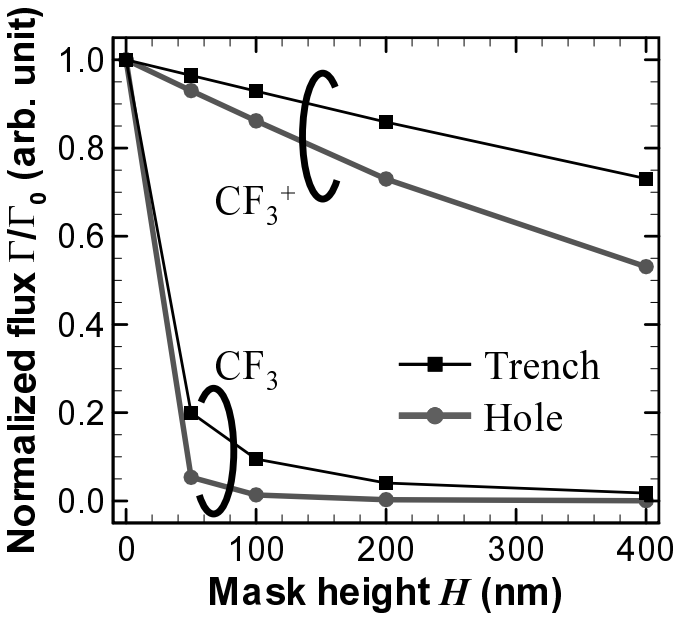

Fig. 3.12: Normalized fluxes Γ/Γ_0 of CF_3 radicals and CF_3^+ ions as a function of mask height H for the hole and trench, calculated under the same conditions shown in Fig. 3.11.

culated under the same conditions shown in Fig. 3.11. Here, angular distribution is concerned with the x-axis component θ_x of the incident angle θ (see Figs. 3.4 and 3.5 for the definitions of θ_x and θ). The distributions over θ_x are similar in both structures, having a prominent peak at $\theta_x = 0°$. The angular distribution is sharper for higher H, while the distribution is isotropic at the top boundary. In other words, the angular distribution of a neutral flux gradually becomes sharper, or the velocity distribution of neutrals gradually becomes anisotropic, towards the bottom of the structure, because neutrals approach the bottom through successive interactions with the mask sidewalls to adsorb and/or reflect thereon.

Figures 3.14(a) and 3.14(b) show the two-dimensional angular distributions of the CF_3 radical flux incident on bottom SiO_2 surfaces for the hole and trench with different mask heights H, respectively, calculated under the same conditions shown in Fig. 3.11. Here, the y-axis component θ_y of the incident angle θ is defined as the x-axis component θ_x (see also Figs. 3.4 and 3.5). The two-dimensional distribution over θ_x and θ_y gives a new point of view, as compared with the one-dimensional distribution over θ_x as shown in the preceding Fig. 3.13, exhibiting marked differences between the two structures. The distribution in the hole is shaped like a circular cone, while that in the trench is shaped like a long hill or a triangle wall ranging from -90 to

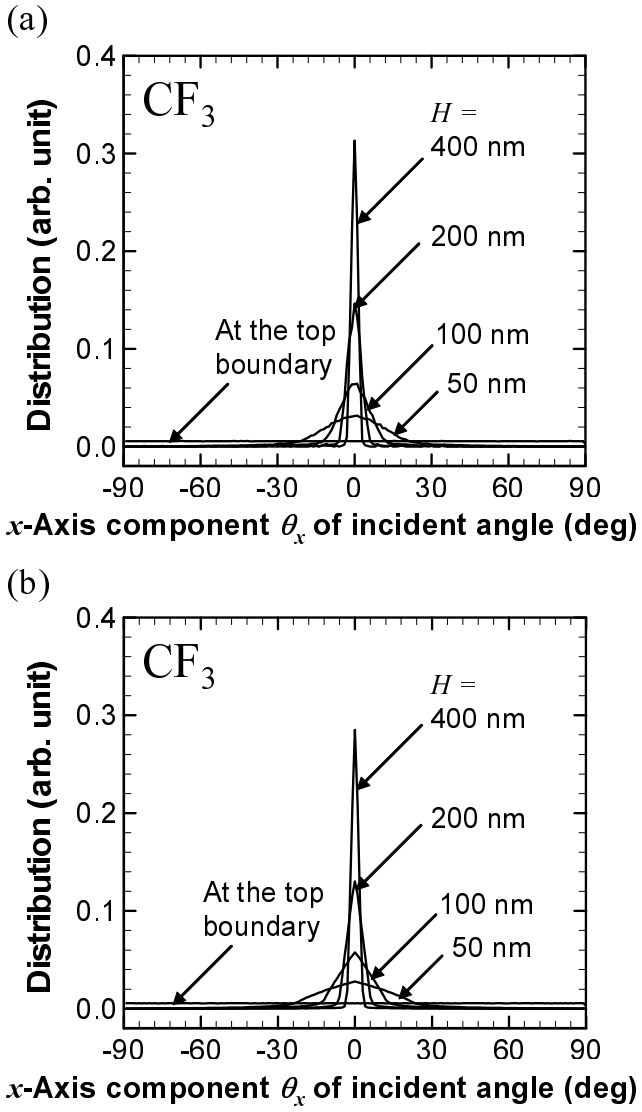

Fig. 3.13: *x*-Axis component of the angular distribution of CF_3 radical flux incident to bottom SiO_2 surfaces for the (a) hole and (b) trench with different mask heights *H*, calculated under the same conditions shown in Fig. 3.11.

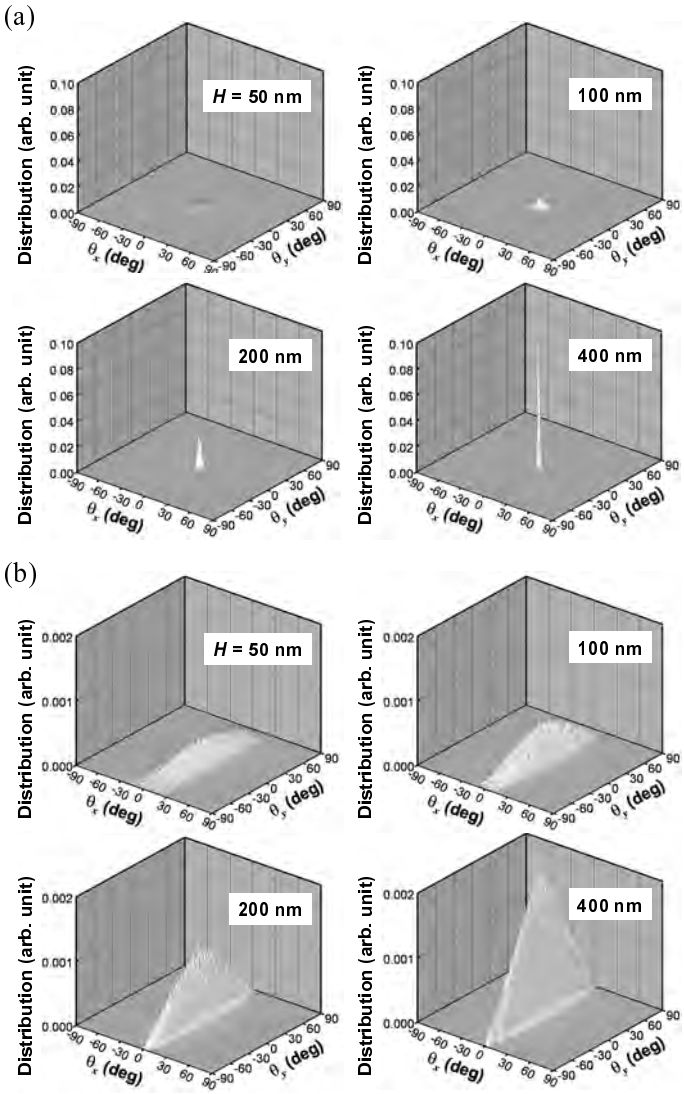

Fig. 3.14: Two-dimensional angular distributions of the CF_3 radical flux incident to bottom SiO_2 surfaces for the (a) hole and (b) trench with different mask heights H, calculated under the same conditions shown in Fig. 3.11.

90° in the *y*-axis; in both structures, the distribution is sharper for higher H, as in Fig. 3.13. Note that in the hole, neutrals reach the bottom of the structure with successive interactions with mask sidewalls in both *x*- and *y*-axis directions (see Fig. 3.5); thus, the angular distribution of the neutral flux over θ is sharper, or the velocity distribution of neutrals is more anisotropic, in the hole than in the trench, and the neutral flux incident to bottom surfaces is smaller in the hole than in the trench. These transport effects for neutrals, as well as the geometrical shadowing effects of the structure, cause differences in feature profile evolution between a hole and a trench.

3.3.4 Mask surface condition

Mask surface conditions such as material and surface roughness are important factors for regulating the particle flux onto the bottom of the structure. Thus, we investigate the effects of mask surface condition on etching profiles by changing the reflection probability of ions and neutrals on mask surfaces from $\gamma = 0.1$ to 0.9. The reflection probability on feature sidewalls has been reported to be $\gamma \approx 0.4$ [15] and 0.5 [21, 44], depending on plasma species and surface material; however, the probability changes largely depending on surface condition during etching.

Figures 3.15(a) and 3.15(b) show the feature profile evolutions of the hole and trench during etching, respectively, simulated for different values of $\gamma = 0.1$, 0.5, and 0.9 with $E_i = 200$ eV, $D/W = 20$ nm, and $H = 100$ nm. Each curve also represents the evolving interfaces every 60 s. In both structures, the etched depth and the rate of bowing or lateral etch decrease with decreasing reflection probability γ, especially in the trench, which is primarily attributed to the smaller neutral flux onto feature surfaces being etched in the case of a smaller γ, as can be seen below.

Figures 3.16(a) and 3.16(b) show the distributions of the CF_3 radical and CF_3^+ ion fluxes incident to mask sidewalls and bottom SiO_2 surfaces for the hole and trench, respectively, calculated under the same conditions shown in Fig. 3.15. In both structures, the neutral flux onto bottom surfaces and sidewalls is smaller for smaller γ, which is more significant for the hole than for the trench. In contrast, the ion flux onto bottom surfaces and sidewalls remains almost the same for different values of γ, and also for the hole and trench. Thus, the neutral-to-ion flux ratio is smaller in the hole than in the trench, and is also smaller for a smaller γ, which results in a higher anisotropy of the etching profile for the hole and for a smaller reflection probability

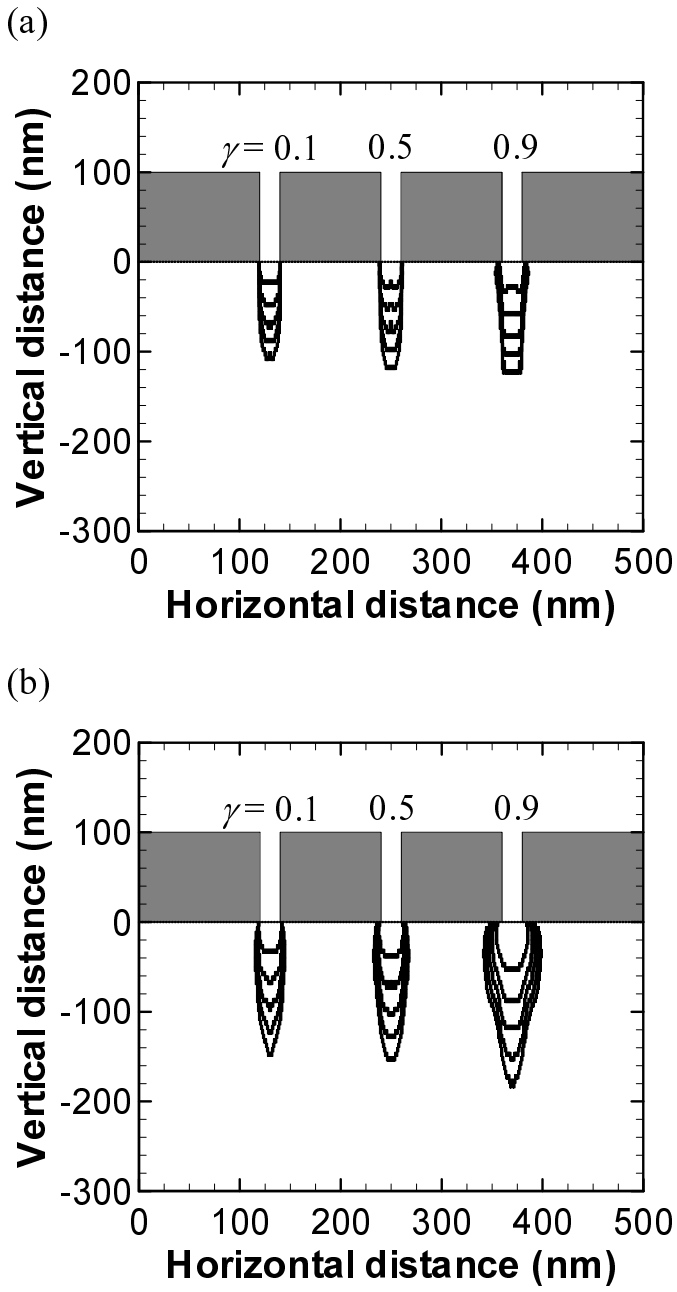

Fig. 3.15: Feature profile evolutions of the (a) hole and (b) trench during etching, simulated for different reflection probabilities $\gamma = 0.1$, 0.5, and 0.9. The other conditions are $D/W = 20$ nm, $H = 100$ nm, and $E_i = 200$ eV. Each curve represents the evolving interfaces obtained every 60 s.

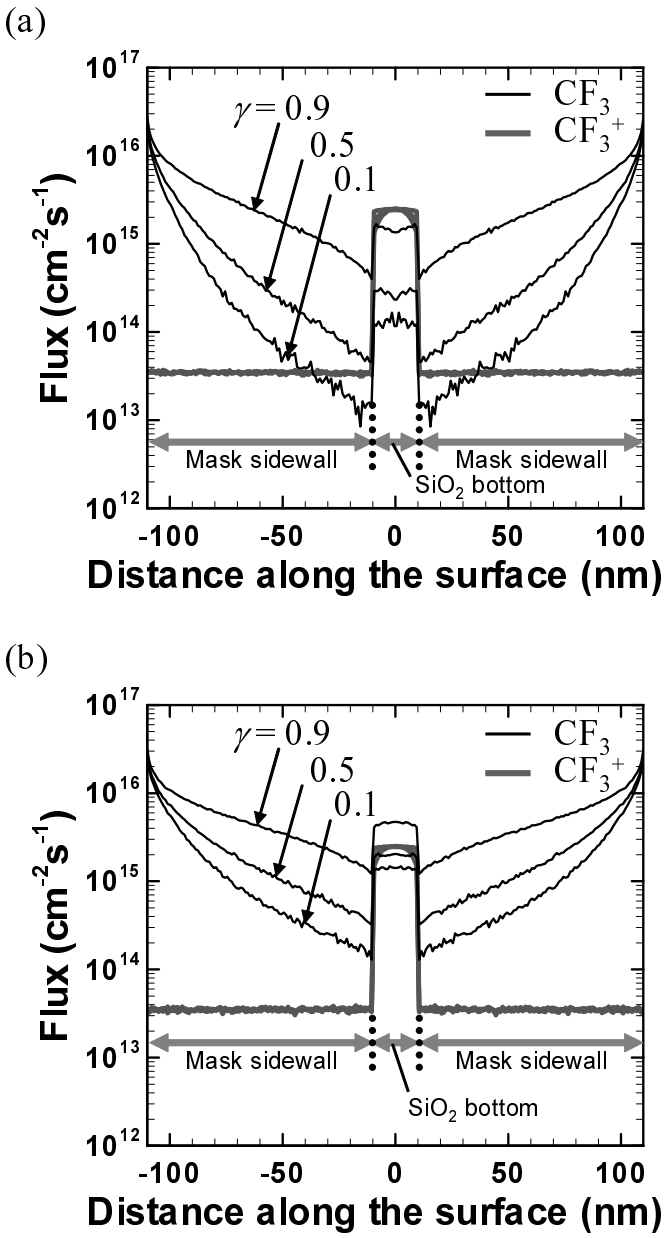

Fig. 3.16: Distributions of CF_3 radical and CF_3^+ ion fluxes incident to mask sidewalls and bottom SiO_2 surfaces for the (a) hole and (b) trench, calculated under the same conditions shown in Fig. 3.15.

γ, as shown in Fig. 3.15.

3.4 Conclusions

Two-dimensional etching profile simulation was conducted to investigate the effects of mask pattern geometry on the feature profile evolution during SiO_2 etching in CF_4 plasmas. The model included the particle transport of ions and neutrals and surface kinetics, for an axisymmetric hole and an infinitely long trench. The calculation used the Monte Carlo technique with a cellular representation of etching profile evolution; in practice, the cell removal method enabled us to treat the two mask pattern geometries of a cylindrical hole and a rectangular trench without changing the numerical scheme. Numerical results indicated that the feature profile evolutions of the hole and trench have similar tendencies under different plasma conditions of ion energy, mask pattern size (D/W), mask height, and reflection probability on mask surfaces. However, two mask pattern geometries exhibited several marked differences: the profile evolution is slower and more anisotropic for the hole than for the trench; in practice, the profile of the trench tends to have prominent lateral etches such as an undercut and a bowing on sidewalls. Moreover, the reactive ion etching lag is less significant for the hole than for the trench. These differences are ascribed to the geometrical shadowing effects of the structure for neutrals, where the incident flux of neutrals is more significantly reduced in the hole than in the trench. The neutral-to-ion flux ratios on bottom surfaces are typically > 1 in the trench and < 1 in the hole, where the etching starves for neutrals and thus is determined primarily by ion flux. The differences are also attributed to the velocity distribution of neutrals in the structure, which is more anisotropic for the hole than for the trench, because more particles interact with mask sidewalls to adsorb or reflect thereon in the hole.

References

[1] M. Kurihara, M. Izawa, J. Tanaka, K. Kawai, and N. Fujiwara: IEEE Trans. Semicond. Manufact. **20** (2007) 232.

[2] M. Boufnichel, S. Aachboun, F. Grangeon, P. Lefaucheux, and P. Ranson: J. Vac. Sci. Technol. B **20** (2002) 1508.

[3] M. A. Vyvoda, H. Lee, M. V. Malyshev, F. P. Klemens, M. Cerullo, V. M. Donnelly, D. B. Graves, A. Kornblit, and J. T. C. Lee: J. Vac. Sci. Technol. A **16** (1998) 3247.

[4] R. E. Jewett, P. I. Hagouel, A. R. Neureuther, and T. Van Duzer: Polym. Eng. Sci. **17** (1977) 381.

[5] J. Pelka: Microelectron. Eng. **13** (1991) 487.

[6] J. Pelka: Microelectron. Eng. **14** (1991) 269.

[7] W. G. Oldham, A. R. Neureuther, C. Sung, J. L. Reynolds, and S. N. Nandgaonkar: IEEE Trans. Electron Devices **27** (1980) 1455.

[8] E. S. G. Shaqfeh and C. W. Jurgensen: J. Appl. Phys. **66** (1989) 4664.

[9] V. K. Singh, E. S. G. Shaqfeh, and J. P. McVittie: J. Vac. Sci. Technol. B **10** (1992) 1091.

[10] J. C. Arnold, H. H. Sawin, M. Dalvie, and S. Hamaguchi: J. Vac. Sci. Technol. A **12** (1994) 620.

[11] M. Tuda, K. Nishikawa, and K. Ono: J. Appl. Phys. **81** (1997) 960.

[12] M. Tuda, K. Ono, K. Nishikawa: J. Vac. Sci. Technol. B **14** (1996) 3291.

[13] M. A. Vyvoda, M. Li, D. B. Graves, H. Lee, M. V. Malyshev, F. P. Klemens, J. T. C. Lee, and V. M. Donnelly: J. Vac. Sci. Technol. B **18** (2000) 820.

[14] B. Abraham-Shrauner: J. Vac. Sci. Technol. B **19** (2001) 711.

[15] S. Takagi, K. Iyanagi, S. Onoue, T. Shinmura, and M. Fujino: Jpn. J. Appl. Phys. **41** (2002) 3947.

[16] L. Elmonser, A. Rhallabi, M. Gaillard, J. P. Landesman, A. Talneau, F. Pommereau, and N. Bouadma: J. Vac. Sci. Technol. A **25** (2007) 126.

[17] J. Chlebe, H. L. Huber, H. Oertel, and M. Weiß: Microelectron. Eng. **9** (1989) 629.

[18] O. Than and S. Büttgenbach: Sens. Actuators A **45** (1994) 85.

[19] G. S. Hwang, C. M. Anderson, M. J. Gordon, T. A. Moore, T. K. Minton, and K. P. Giapis: Phys. Rev. Lett. **77** (1996) 3049.

[20] R. J. Hoekstra, M. J. Grapperhaus, and M. J. Kushner: J. Vac. Sci. Technol. A **15** (1997) 1913.

[21] J. P. Chang, A. P. Mahorowala, and H. H. Sawin: J. Vac. Sci. Technol. A **16** (1998) 217.

[22] T. Won: J. Korean Phys. Soc. **33** (1998) S72.

[23] R. J. Hoekstra, M. J. Kushner, V. Sukharev, and P. Schoenborn: J. Vac. Sci. Technol. B **16** (1998) 2102.

[24] I. Karafyllidis: Adv. Eng. Software **30** (1999) 419.

[25] I. Karafyllidis: Model. Simulation Mater. Sci. Eng. **7** (1999) 157.

[26] K. P. Giapis and G. S. Hwang: Thin Solid Films **374** (2000) 175.

[27] D. Zhang and M. J. Kushner: J. Vac. Sci. Technol. A **19** (2001) 524.

[28] A. P. Mahorowala and H. H. Sawin: J. Vac. Sci. Technol. B **20** (2002) 1064.

[29] W. Jin, S. A. Vitale, and H. H. Sawin: J. Vac. Sci. Technol. A **20** (2002) 2106.

[30] M. A. Blauw, E. van der Drift, G. Marcos, and A. Rhallabi: J. Appl. Phys. **94** (2003) 6311.

[31] W. Jin and H. H. Sawin: J. Electrochem. Soc. **150** (2003) G711.

[32] G. Macros, A. Rhallabi, and P. Ranson: J. Vac. Sci. Technol. A **21** (2003) 87.

[33] Y. Osano and K. Ono: Jpn. J. Appl. Phys. **44** (2005) 8650.

[34] Y. Osano and K. Ono: J. Vac. Sci. Technol. B **26** (2008) 1425.

[35] H. H. Hwang, T. R. Govindan, and M. Meyyappan: J. Electrochem. Soc. **146** (1999) 1889.

[36] Y. H. Im, Y. B. Hahn, and S. J. Pearton: J. Vac. Sci. Technol. B **19** (2001) 701.

[37] H. H. Hwang, M. Meyyappan, G. S. Mathad, and R. Ranade: J. Vac. Sci. Technol. B **20** (2002) 2199.

[38] A. La Magna and G. Garozzo: J. Electrochem. Soc. **150** (2003) F178.

[39] T. Shimada, T. Yagisawa, and T. Makabe: Jpn. J. Appl. Phys. **45** (2006) L132.

[40] G. Kokkoris, A. G. Boudouvis, and E. Gogolides: J. Vac. Sci. Technol. A **24** (2006) 2008.

[41] M. Dalvie, R. T. Farouki, and S. Hamaguchi: IEEE Trans. Electron Devices **39** (1992) 1090.

[42] C.-K. Chung: J. Micromech. Microeng. **14** (2004) 656.

[43] J. Kiihamäki and S. Franssila: J. Vac. Sci. Technol. A **17** (1999) 2280.

[44] M. F. Doemling, N. R. Rueger, and G. S. Oehrlein: Appl. Phys. Lett. **68** (1996) 10.

[45] M. M. IslamRaja, M. A. Cappelli, J. P. McVittie, and K. C. Saraswat: J. Appl. Phys. **70** (1991) 7137.

[46] D. G. Coronell and K. F. Jensen: J. Electrochem. Soc. **141** (1994) 2545.

[47] O. Kwon, H. Jung, S. Yoon, and T. Won: J. Korean Phys. Soc. **39** (2001) 100.

[48] G. S. Oehrlein, M. F. Doemling, B. E. E. Kastenmeier, P. J. Matsuo, N. R. Rueger, M. Shaepkens, and T. E. F. M. Standaert: IBM J. Res. Dev. **43** (1999) 181.

[49] Y. Chinzei, T. Ichiki, N. Ikegami,Y. Feurprier,H. Shindo, and Y. Horiike: J. Vac. Sci. Technol. B **16** (1998) 1043.

[50] N. Ikegami, A. Yabata, T. Matsui, J. Kanamori, and Y. Horiike: Jpn. J. Appl. Phys. **36** (1997) 2470.

[51] C. Liu and B. Abraham-Shrauner: IEEE Trans. Plasma Sci. **30** (2002) 1579.

[52] J. A. Levinson, E. S. G. Shaqfeh, M. Balooch, and A. V. Hamza: J. Vac. Sci. Technol. A **15** (1997) 1902.

[53] H. Fukumoto, K. Takahashi, and K. Ono: Proc. 24th Symp. Plasma Processing, Nagoya, 2005, p. 108

[54] H. Fukumoto, I. Fujikake, Y. Takao, K. Eriguchi, and K. Ono: Plasma Sources Sci. Technol. **18** (2009) 045027.

[55] M. A. Lieberman and A. J. Lichtenberg: *Principles of Plasma Discharges and Materials Processing* (Wiley, 2005, Hoboken, NJ) 2nd ed., p. 37.

[56] D. K. Bhattacharya: Phys. Rev. A **43** (1991) 761.

[57] H. Kerstena, H. Deutscha, H. Steffena, G. M. W. Kroesenb, and R. Hippler: Vacuum **63** (2001) 385.

[58] S. T. Seo, Y. H. Lee, K. S. Lee, D. R. Yang and B. K. Choi: Proc. Int. Conf. Control, Automation and Systems, Gyeonggi, Korea, 2005.

[59] E. Gogolides, P. Vauvert, G. Kokkoris, G. Turban and A. G. Boudouvis: J. Appl. Phys. **88** (2000) 5570.

[60] C. Steinbrüchel: Appl. Phys. Lett. **55** (1989) 1960.

[61] D. Zhang and M. J. Kushner: J. Vac. Sci. Technol. A **19** (2001) 524.

Chapter 4

Charging Effects on Flux Characteristics

4.1 Introduction

Higher-aspect-ratio patterning is indispensable for next generation ultralarge-scale integrated circuits (ULSI). In particular, the etching of contact holes through SiO_2 layers or via holes through low-dielectric films are key processes in fabricating multilayer interconnections [1, 2]. However, as the feature size is reduced to a nanometer level, the etching requirement becomes more severe. Many serious problems occur during the high-aspect-ratio etching process, such as charge-buildup damage [3–5], etching stop [6–8], and microloading effects [6, 9, 10]. The dependence of etch rate on feature dimensions has been referred to as reactive ion etching (RIE) lag, or aspect ratio dependent etching (ARDE) [11–14]. These phenomena are attributed to various mechanisms such as transport of neutrals, ion shadowing, neutral shadowing, and differential charging of the insulating microstrucure [12].

Here, charging damage is attracting a great deal of attention as one of the most serious current and future problems in plasma processing [15]. In particular, pattern-dependent charging is rapidly becoming one of the most serious issues to confront plasma processing of advanced ULSI [16]. Understanding charging damage requires detailed modeling and simulation of ion and electron dynamics in plasmas, through sheaths, and as they impinge at various microstruc-

ture surfaces where they cause charging, physical sputtering, and chemical reactions.

Charging is also possible to cause profile irregularities in process and degradation in performance. The mechanisms mainly concern the rf electric field, nonuniform plasma, nonuniform bias voltage, and electron-shading effect. In addition, electron shading can also cause structural defects during etching in the form of sidewall bowing, microtrenching, undercutting, and notching [17, 18]. Furthermore, it has been discovered that charging is one of the main causes of the problems involved in high aspect ratio plasma processing. These problems include notching, etch stop, micro-loading and ARDE [12].

Local charging is attributed to the difference in angular distributions of ions and electrons in the sheath. The electrons have a broad velocity distribution, while the ions have a sharp velocity distribution. Therefore the upper sidewalls are negatively charged, because the electrons initially impact the sidewalls more than the ions. On the other hand, the bottoms of the feature are positively charged [19]. The local charging between a topologically different pattern exposed to plasmas during etching has been traditionally understood by a mechanism of electron shading induced by the great difference in velocity distribution between the positive ions and electrons incident on the microstructures [18, 20, 21]. Charge builds up until the bottom surface acquires a potential large enough to repel a sufficient number of ions so that the ion and electron currents to the bottom surface balance [4, 22]. The repelled ions bombard the sidewalls, increasing the charging potential on the sidewalls. As the potential difference across the underlying gate oxide builds up, large Fowler-Nordheim tunneling currents are possible to lead to oxide degradation and breakdown [18, 23].

Current balance is accomplished when equal fluxes of ions and electrons impinge onto each surface segment. While the directionality difference has no important issue for flat surfaces, it can significantly perturb the current balance when the surface is patterned as a result of geometrical shading of the surface segment from the oblique electrons by the features that constitute the pattern. The phenomenon, termed ”electron shading”, is a major cause of charging damage during plasma processing [23]. The total charge density and its distribution along the surface at steady state depend upon the geometry of the structure and the initial energy and angle distributions of the ions and electrons [19]. In particular, the high aspect ratio features (depth over diameter/width) influence critically the ability of electrons to reach the feature bottom. Owing to a result of geometrical shadowing of the more isotropic electrons and the local electrostatics

in the feature, which adjust the bottom and sidewall potentials so that electrons can be attracted to balance the ion current to the various surfaces [24].

Various modeling approaches have been tried to predict feature profile evolution and provided useful insights to many difficulties such as RIE lag, inverse RIE lag, bowing, trenching, faceting. Arnold and Sawin modeled the localized charging of a rectangular trench during the plasma etching of a perfectly insulating surface by assuming an isotropic electron flux and monodirectional ion bombardment [19]. Mahorowala and Sawin simulated the electric potential near the feature surfaces through their Monte Carlo method profile evolution simulator incorporating charging model, assuming two electrical assumptions of a perfect insulating feature and a resistive feature [25]. Kinoshita *et al.* found significant positive charging at the bottom of high aspect ratio features and related it to the notching observed on the inner wall of the outermost line [4]. Hwang and Giapis *et al.* devotedly investigated charging mechanisms during plasma etching by using two-dimensional Monte Carlo simulations, obtaining electric potential, ion trajectories, and profile evolutions [15, 16, 22, 26–31]. They found that charging effects are fluctuated by several mechanisms such as mask thickness, electron temperature, the number of line-and-space features, and the ratio of the exposed area to the patterned area. Park and Lee *et al.* studied charge-up phenomena for the aspect ratios of 5 and 10, and different pressures of 10, 50, and 100 mTorr. At a high-aspect ratio, the charge-up potential was reduced when the pressure of a plasmas chamber is high. At a high pressure, more vertical etching feature is expected [32]. Lee and Chang *et al.* performed a simplified two-dimensional Monte Carlo simulations is performed to estimate the charging potential fluctuations caused by strong binary Coulomb interactions between discrete charged particles in nanometer scale trenches. They found that the discrete charge effect can be an important part of the nanoscale trench research, inducing scattering of ion trajectories in a nanoscale trench by a fluctuating electric field [33]. Ootera and Namba *et al.* investigated ion trajectories near a submicron-patterned surface through numerical simulations including the effects of local charging on the patterned surface and ion drift velocity toward the wafer. They showed that the ion trajectories were largely deflected at the inside of the outermost lines of the line-and-space patterns [5]. Vyvoda and Graves *et al.* simulated ion trajectories and feature profiles of a trench, comparing to their previous experiments [34]. Matsui and Makabe *et al.* simulated the wall potential in the trench exposed to plasma etching in a pulsed operation, assuming different surface conductivity [1].

They also numerically investigated physical and electrical influences on plasma etching on the inside of a microtrench in SiO_2 by using Monte Carlo simulation of ions and electrons with the aid of surface charge continuity and Poisson's equation [35].

A number of researchers have studied the effect of feature charging during the high density plasma etching and have made efforts to reduce the trench charging have been suggested, including negative ion discharges and pulsed operations [36]. Schaepkens and Oehrlein have shown experimentally that charging of the insulating material enhances microtrench formation in SiO_2 etching. A weak magnetic field increased the negative charge buildup on the oxide sidewall, thus steering positive ions towards one side of the trench and producing asymmetric microtrenches [37]. Ohtake and Samukawa *et al.* measured charge accumulation during pulse-time-modulated (TM) plasma process by using their developed on-wafer monitoring chip. The results indicated that the accumulated charge in the TM operation was drastically decreased compared to continuous-wave plasma [2]. Upadhyaya and Kruger *et al.* showed scanning surface-potential microscopy can be used to measure the differential charging in a high-aspect-ratio pit through measuring the surface potential of the structures after plasma exposure, and suggested a circuit model used to explain the experimental results [38]. Bogart and Lane *et al.* investigated mask charging and profile evolution through experiments of chlorine plasma etching of silicon, showing that charging of an insulating mask is not the primary origin of microtrench formation during Cl_2 etching of Si(100) or poly-Si [39]. Ohmori, Kamata Goto, Kitajima, and Makabe investigated time-resolved charging and discharging on patterned SiO_2 during one on/off period [20].

Charging damage generally depends on plasma parameters, such as electron and ion temperatures, plasma density, and rf bias voltage and frequency [40]. It also depends strongly on the pattern geometry: feature aspect ratio, mask aspect ratio, open areas separating dense patterns, antenna area, and gate oxide area.

When the patterns consist of insulating materials, plasma-induced charging may cause ion deflection with undesirable consequences; for example, mask charging leads to sidewall profile irregularities when etching high-aspect-ratio features [19, 41]. Therefore, the relation between mask pattern geometry and potential distribution is important for the more precise processing. However, only a few studies have been performed regarding the etching of oxides. The studies of charging were mostly performed for poly-Si with resist and these revealed that local poten-

tials may develop in high aspect ratio trenches which will change the trajectories of ions and affect the ion-assisted etching [22, 42, 43].

Understanding charging potential requires detailed modeling and simulation of ion and electron dynamics in plasmas, through sheaths, and as they impinge at various microstructure surfaces where they cause charging, physical sputtering and chemical reactions, or undergo inelastic scattering. We have developed a self-consistent flux simulator that combines rf sheath, surface charging, and long-range electrostatic effects [15]. Physical and electrical influences on plasma etching on the inside of a microstructure in SiO_2 were numerically investigated using particle simulation of ions and electrons with the aid of surface charge continuity and Poisson's equation [35].

In this study, we observe the surface potential distribution and ion trajectories over the microstructure by varying aspect ratios between two different geometries of a hole and a trench. We assume SiO_2 etching by using CF_4 inductively coupled plasmas (ICPs). Attention is imposed on the effects of mask pattern geometry of surface potential distribution and ion trajectories. We employ Poisson's equations for surfaces potential distribution and ballistic model of plasma species for ion trajectories.

4.2 Model

In this work, we have employed kinetic process for particle trajectories with surface charge continuity and Poisson's equation in order to investigate the growth of local potential inside geometrically different microstructures on a resist mask and a dielectric SiO_2 exposed by a fluorocarbon plasma for a wide range of aspect ratios.

4.2.1 Simulation domain

We consider two structures of an axisymmetric circular hole and an infinitely long rectangular trench in two dimensions, as shown in Fig. 4.1. The whole simulation domain is represented by a number of two-dimensional cells, each of which is a rectangular doughnut ring for the hole and an infinitely long rectangular parallelepiped for the trench. The substrate surfaces have two layers: the upper layer for the resist mask and the lower for SiO_2, where both layers to be perfect insulator. We do not take into account any kind of possible charge transfer by means

of the surface or bulk current or surface discharge because details of these processes are not clear. In other words, particles impinging the surface of a dielectric are considered to remain at the point where they hit the surface. The particles are generated at the top boundary of the simulation region. The particle trajectories are tracked through a three-dimensional position and a three-dimensional velocity.

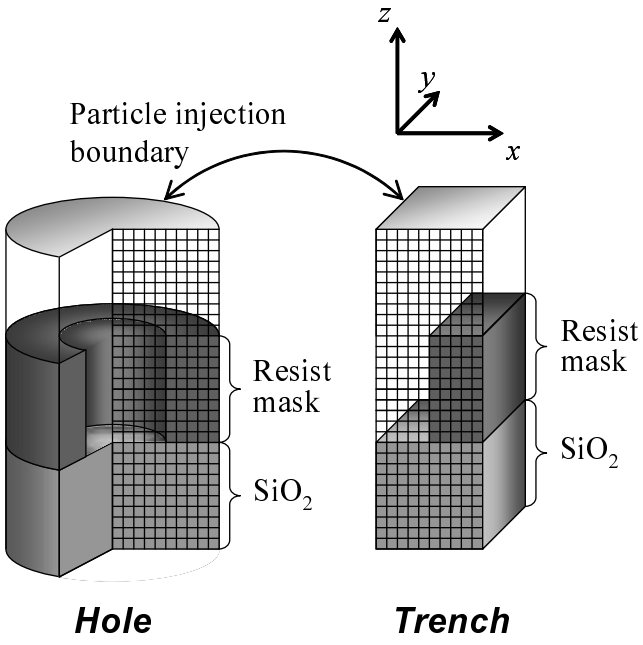

Fig. 4.1: Schematic of the simulation domain.

We employ two-dimensional cells for representing the difference in geometrical effects on potentials and charging fluxes between a hole and a trench. The two geometries are represented by two-dimensional coordinates (r, z) for a hole and (x, z) for a trench. In the hole model, the section of each cell is rectangular with an area $\Delta r \times \Delta z$, and the nth cell from the center axis has an inner radius of $(n-1)\Delta r$ and an outer radius of $n\Delta r$. On the other hand, in the trench model, the cells employed are all the same with the section of each cell being rectangular with an area $\Delta x \times \Delta z$ as shown in Fig. 4.2. The cell volume is $v_{\text{cell}} = (2n-1)\pi(\Delta r)^2\Delta z$ for the nth cell in a hole, and $v_{\text{cell}} = \Delta x \Delta y \Delta z$ for all the cells in trench. The parameters taken in the present calculation are $\Delta x = \Delta r = 1$ nm, $\Delta z = 1$ nm, and $\Delta y = 60$ nm.

The model for flux and potential calculation consists of four modules: a particle injection module where particles are injected from the plasma through the sheath, a particle transport

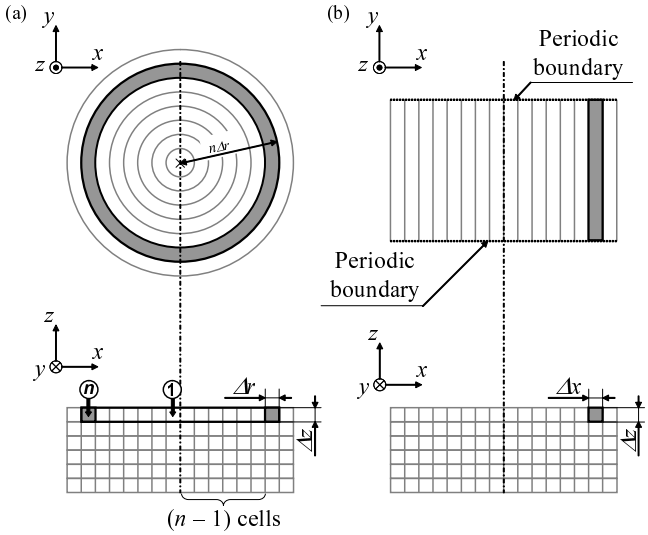

Fig. 4.2: Schematic of the cell structure in the simulation domain: (a) rectangular doughnut ring for the hole and (b) infinitely long rectangular parallelepiped for the trench.

module where particles are transported from the top boundary of the simulation domain toward feature surfaces, a particle deposition module treating the interactions between incident particles and surfaces, and a potential calculation module where potential is renewed for affecting charged particle trajectories. The injection module calculates the flux of particles using parameters such as species density, temperature, and oscillating sheath voltage obtained from plasma and sheath simulation. The transport module calculates the flux of particles transported onto surfaces, including the incident angle thereon. Then, the particle deposition module counts particles reaching surfaces to calculate charge deposition. The potential calculation module calculates deposited charging on the surface, and determine electric potential distribution of the whole simulation domain.

Figure 4.3 shows the flowchart of the simulation. At the beginning, newly injected particles from the plasma are characterized by their own initial positions and velocities based on plasma and sheath condition. All particles in the simulation domain move at their own velocities every small time step Δt. The number of ions and electrons reaching the surface cell are counted, and then charge density is accumulated on the surface cell. The electric potential is obtained by solving Poisson's equation. Then, the electric field is calculated from the resulting electric potential and used for renewing the velocity of ions and electrons. The procedures are repeated

during the calculation.

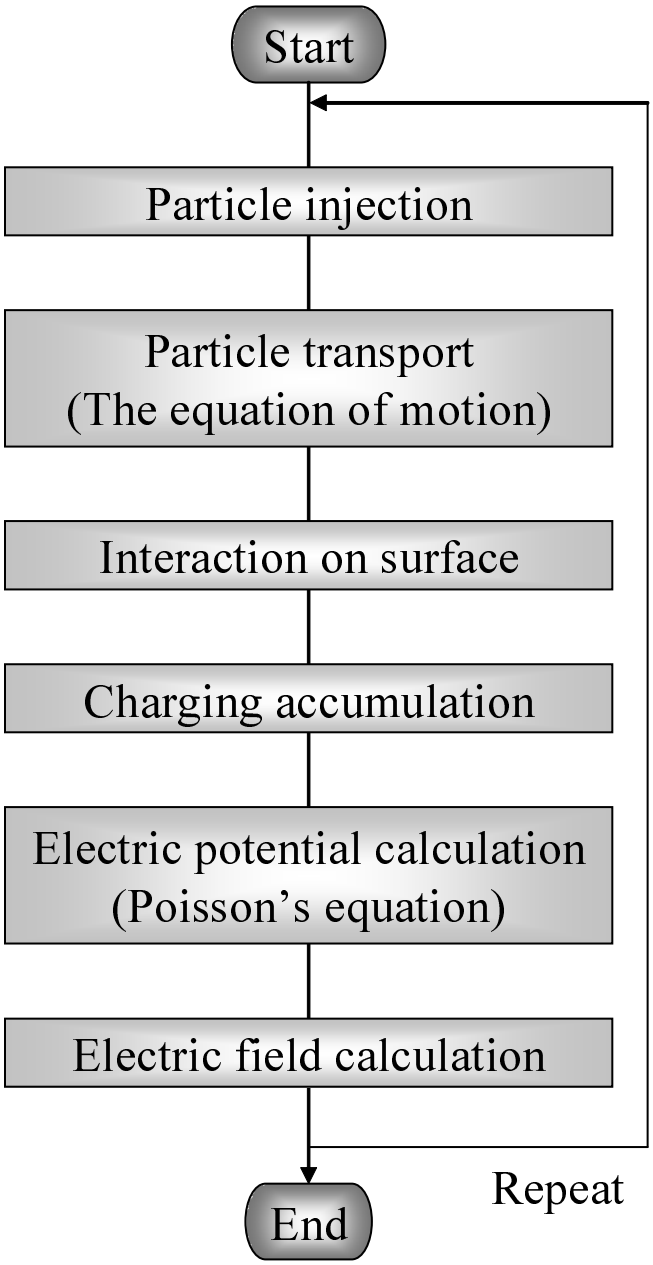

Fig. 4.3: Flowchart of the simulation.

4.2.2 Plasma conditions and particle transport

Silicon dioxide etching in fluorocarbon plasmas involves a number of chemical species, which result in complicated gas-phase and surface reactions. Since all these reactions are difficult to treat in the simulation, several important ones are selected in the model. We assume fluoro-

Table I: Densities of ions in the plasma.

Ion	Density (m^{-3})
CF^+	5.49×10^{14}
CF_2^+	1.31×10^{16}
CF_3^+	1.34×10^{17}

carbon plasmas containing five charged species (i.e., CF_3^+, CF_2^+, CF^+, and electron), as listed in Table I, where neutral species are omitted in this model to focus on charging effects from flux of charged species. The respective densities in the plasma are taken from our gas-phase calculations of ICP CF_4 plasmas at 10 mTorr and 250 W [44, 45]. The electron density n_e is equal to the sum of all positive ions $n_e = n_{CF_3^+} + n_{CF_2^+} + n_{CF^+}$. The ions are assumed to be in thermal equilibrium at $T_i = 0.5$ eV and the electrons at $T_e = 3$ eV in the plasma.

The species originating from the plasma given randomly Bohm velocity for ions and thermal velocity for electrons. The ions and electrons affected electrically through sheath are injected from the top boundary of the simulation domain above 50 nm from the top mask surface before they travel into the simulation domain in the microstructures. Therefore, the velocity distribution of injected particles is anisotropic for ions and electrons after passing across the sheath. Here, particle simulation is employed on the basis of successively injected multi-particle trajectories with three velocity components (v_x, v_y, v_z).

The ion flux $\Gamma_i = \sum_i \Gamma_i$ is given by [46]

$$\Gamma_i = \sum_i \Gamma_i = \sum_i n_{si} u_{Bi} = 0.61 \sum_i n_{0i} u_{Bi}, \tag{4.1}$$

where n_{si} is the plasma density at the sheath edge of ion i ($i = CF_3^+$, CF_2^+, and CF^+), $u_{Bi} = \sqrt{kT_e/M_i}$ the Bohm velocity of ion i, k the Boltzmann constant, M_i the mass of ion i, and n_{0i} the bulk plasma density of ion i. Ions acquire their own kinetic energy after being accelerated through the sheath between the plasma and substrate surfaces; the resulting energetic ions have their own thermal energy plus a given bias voltage. The electron flux Γ_e has a relation of $\Gamma_e = \Gamma_i$. The velocity is defined in three dimensions at the top boundary before calculation of the sheath

model. The isotropic velocity (v_x, v_y, v_z) of ions and electrons in the bulk plasma is given as [47]

$$v_x = \sqrt{-\frac{2kT \ln \xi_1}{M}} \cos 2\pi\xi_2, \tag{4.2}$$

$$v_y = \sqrt{-\frac{2kT \ln \xi_1}{M}} \sin 2\pi\xi_2, \tag{4.3}$$

$$v_z = -\sqrt{-\frac{2kT \ln \xi_3}{M}} \sin \pi\xi_4, \tag{4.4}$$

where T is the temperature of a particle, M is the mass of a particle, and ξ_1, ξ_2, ξ_3, and ξ_4 are random numbers between 0 and 1 independent of each other.

We use a rf sheath model and a resulting ion and electron energy distribution from a particle simulation, instead of a monoenergetic ion beam. Ions and electrons transport through the sheath are solved explicitly to determine realistic energy flux and angular distributions of ions and electrons arriving at the surfaces. The rf frequency is 13.56 MHz with the dc bias voltage 200−800 V. The rf electric field in the sheath must be combined with the equation of motion for ions and electrons. We apply the linear model of Kushner [48], where the electric field decrease in magnitude linearly proportional with distance for the electric field on position. The sheath is assumed to be collisionless in view of the low pressure (10 mTorr) used in the ICP plasma.

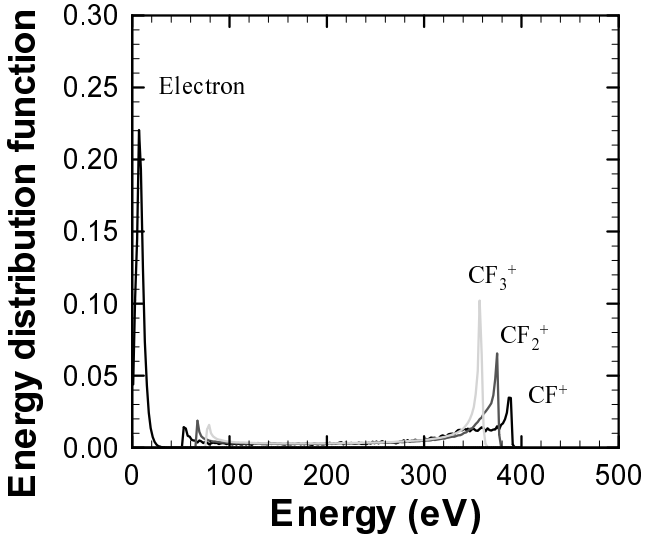

Fig. 4.4: Ion energy distribution functions of CF_3^+, CF_2^+, CF^+ ions, and electron energy distribution function arriving at the sheath lower boundary as predicted by a nonlinear sheath model. The sheath parameters were: $V_{dc} = -200$ V, $V_{rf} = 205$ V, and $f_{rf} = 13.56$ MHz.

Figure 4.4 shows ion energy distribution function (IEDF) and electron energy distribution function (EEDF) at the sheath condition: dc bias voltage $V_{dc} = -200$ V, $V_{rf} = 205$ V, and $f_{rf} = 13.56$ MHz. As a result of the rf oscillation, ions entering the sheath at different phases of one rf cycle will gain different energy as they cross the sheath. The ions striking the feature surfaces have a bimodal energy distribution after being accelerated in the rf sheath. The splitting of the ion energy distribution is typical when the sheath thickness is small because ions can cross the sheath in less than one rf cycle. The high energy peak has higher intensity than the low energy peak, as expected from the selfconsistent treatment of the sheath at the high rf bias frequency. The low energy peak of the IEDF is essential for reaching steady-state charging at the sidewalls. The IEDF of heavy ions has a narrow peak interval owing to their own large inertia. The EEDF curve has one sharp peak at the 10 eV because electrons can pass the sheath in small time range of one rf cycle, while the IEDF curve has two peaks at about 70 eV and 370 eV. The EEDF and IEDF indicates that this model has good agreement with the numerical results by Hwang *et al.* [49] and the experimental results by Edelberg *et al.* [50]

In addition to energy distribution, angular distribution of incident flux is important to analyze fluxes of ions and electrons. Here, the incident angle θ and its x-axis component θ_x are defined as shown in Fig. 4.5, where θ takes values from 0 to 90°, and θ_x takes values from −90 to 90°. y-Axis component θ_y is defined as the same with θ_x.

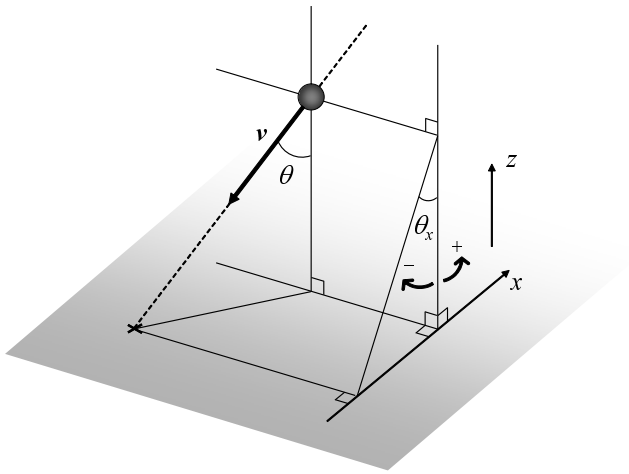

Fig. 4.5: Definition of the incident angle θ and its x-axis component θ_x.

4.2.3 Surface interactions

The particles injected into the simulation domain strike either the resist mask or SiO_2-layer surfaces unless they are repelled from electric potential barriers. The particles travel towards feature surfaces by repeating reflections on mask sidewalls with a given probability γ, and thus adsorbing thereon with a probability $(1 - \gamma)$. The reflection is assumed to be specular for ions, while diffusive for neutrals at a surface temperature of 300 K [51]. The reflection probability is zero for electrons. Electrons disappear from the simulation domain at the reaching point of the surface leaving its charge. On SiO_2 layer surfaces, all incident species are assumed to react with the SiO_2 surfaces without reflection.

It is also assumed that there is no re-emission of the incident electrons on all surfaces. Then local electric field is generated by the total charge of the electrons or ions on the patterned surface. The trajectories of electrons and ions are calculated by solving the equation of motion with the electric field.

4.2.4 Charging model

A charging potential calculation module is added to our previous model [44]. Fluxes to the surfaces of the structure are determined in every time step Δt and the wall charge densities are calculated temporally. The electrons and ions incident on the patterned surface are counted at every small surface segment in every time step. The resulting potentials are then calculated and the next step of simulation in the revised potential is carried out. Local electric field near the patterned surface is calculated from the revised potential. In the next time step, the trajectories of the electrons and ions are recalculated including the effect of the local electric field. The steady state is obtained when the potential distribution along the bottom SiO_2 surface no longer changes [22]. Surface currents and secondary electron emission are both neglected. Charge deposition creates local electric fields determined by solving Poisson's equation. The fields are used to alter ion and electron trajectories and are modified self-consistently as more charge accumulates. The mask and the SiO_2 layer are both perfect insulators in the simulation, where the dielectric constant 3.9 of SiO_2 is employed. The SiO_2 is assumed to be thick enough to prevent any tunneling current to the substrate.

Poisson's equation, $\nabla^2\phi = -\frac{\rho}{\varepsilon}$, is solved in the entire simulation domain, taking into con-

sideration the surface charge distribution along the pattern, where ρ is the charge density on the resist mask and SiO_2 surfaces, and ε is the permittivity of the resist mask and SiO_2 layer, respectively. Charge deposition creates local surface potentials that give rise to local electric fields which, in turn, alter ion trajectories.

We traced the electron and ion trajectories under a local wall potential by charging in each time step, and computed the further charge accumulation from the fluxes incident on the wall surface. The potential distribution was then calculated by solving Poisson's equation for a hole:

$$\frac{1}{r}\frac{\partial \phi}{\partial r} + \frac{\partial^2 \phi}{\partial r^2} + \frac{\partial^2 \phi}{\partial z^2} = -\frac{\rho}{\varepsilon}, \tag{4.5}$$

while Poisson's equation for a trench:

$$\frac{\partial^2 \phi}{\partial x^2} + \frac{\partial^2 \phi}{\partial z^2} = -\frac{\rho}{\varepsilon}. \tag{4.6}$$

We obtain an electric field from the resulting potential for a hole (E_r, E_z) written as:

$$E_r = -\frac{\partial \phi}{\partial r}, E_z = -\frac{\partial \phi}{\partial z}, \tag{4.7}$$

and for a trench (E_x, E_z) written as:

$$E_x = -\frac{\partial \phi}{\partial x}, E_z = -\frac{\partial \phi}{\partial z}, \tag{4.8}$$

The probability that more than two particles exist in the simulation space at the same time is very low because the life time of particles in the simulation region is much shorter than the incident time interval. Therefore, Poisson's equation with the absence of space charge ρ is simplified to Laplace's equation $\nabla \phi = 0$. The solution of Laplace's equation are repeated until steady state is reached as monitored by surface potential distributions that no longer change. This condition corresponds to equal fluxes of ions and electrons impinging at all points along the microstructure surfaces. After a reasonable number of particles has been sampled, Poisson's equation is solved for the simulation domain subject to the following boundary conditions of $\nabla V = 0$ at the boundaries except the top and bottom: the cylindrical sidewall boundary for a hole, and the left, right, back and forth sidewall boundary for a trench, where the Neumann boundary condition, and the periodic boundary conditions, $\phi_{\text{left}} = \phi_{\text{right}}$ and $\phi_{\text{back}} = \phi_{\text{forth}}$ are adopted, and at the top and bottom the Dirichlet boundary conditions, $\phi_{\text{top}} = \phi_{\text{bottom}} = 0$ are employed. Particles arriving at periodic boundary pass the boundary and ejected from opposite side periodic boundary.

4.3 Results and Discussion

To investigate the effects of the mask pattern geometry on the resulting ion and electron fluxes, we simulate fluxes onto the surfaces and distribution of incident angles of the plasma species by varying parameters such as mask height and reflection probability on the mask surface. The following is chosen as a standard condition: mask pattern diameter/width of 20 nm, ion energy of 200 eV, and reflection probability of 0.5 on the mask surface.

4.3.1 Flux equilibrium

The goal of this first step is to obtain the converged potential, at each point on the dielectric surface, that equalizes time-averaged ion and electron fluxes. This criterion is the necessary condition for charging convergence. Figures 4.6(a) and 4.6(b) show time resolved flux of positive ion and electron onto the surfaces of the top and the bottom of the structure in the (a) hole and (b) trench, calculated under the standard condition with mask height of 40 nm. The positive ion fluxes onto the top in both hole and trench initially increase and reach almost the same amount of electron flux, while the ion fluxes onto the bottom increase initially, then drop rapidly, and again increase to almost the same amount of electron flux. The time to reach the equilibrium on the top of about 150 μs is shorter than the time on the bottom of about 400 μs in the hole and 300 μs in the trench. The time lag between the top and the bottom in both structures indicates that incident flux on the bottom is less than that on the top owing to geometrical shadowing from a point of view of flux equilibrium.

4.3.2 Potential Distribution

Figures 4.7(a) and 4.7(b) show two-dimensional potential distributions on the xz plane between the particle injection boundary and the bottom surface for the (a) hole and (b) trench, calculated under the standard condition with different mask heights H = 20, 40, 60, and 80 nm. Every figure shows that the potential increases linearly from the particle injection boundary of 0 V to the mask opening of about 350 V. The difference of potential distribution between the hole and the trench is observed inside the mask structure. The potentials are almost flat in the hole, while the potentials have its maximum at the mask opening and 50−100 V drop at the bottom in the trench. The difference of the potentials between the hole and trench can be due to the difference

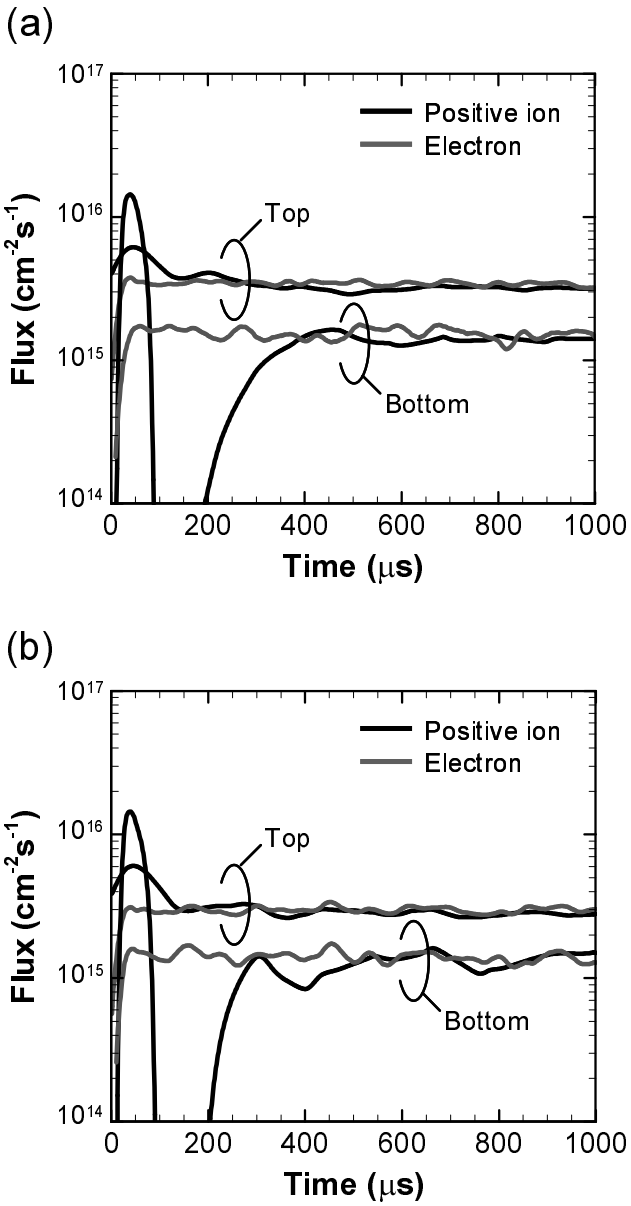

Fig. 4.6: Time resolved flux of positive ion and electron onto the surfaces of the top and the bottom in the (a) hole and (b) trench, calculated under the standard condition with mask height of 20 nm.

of mask pattern geometry.

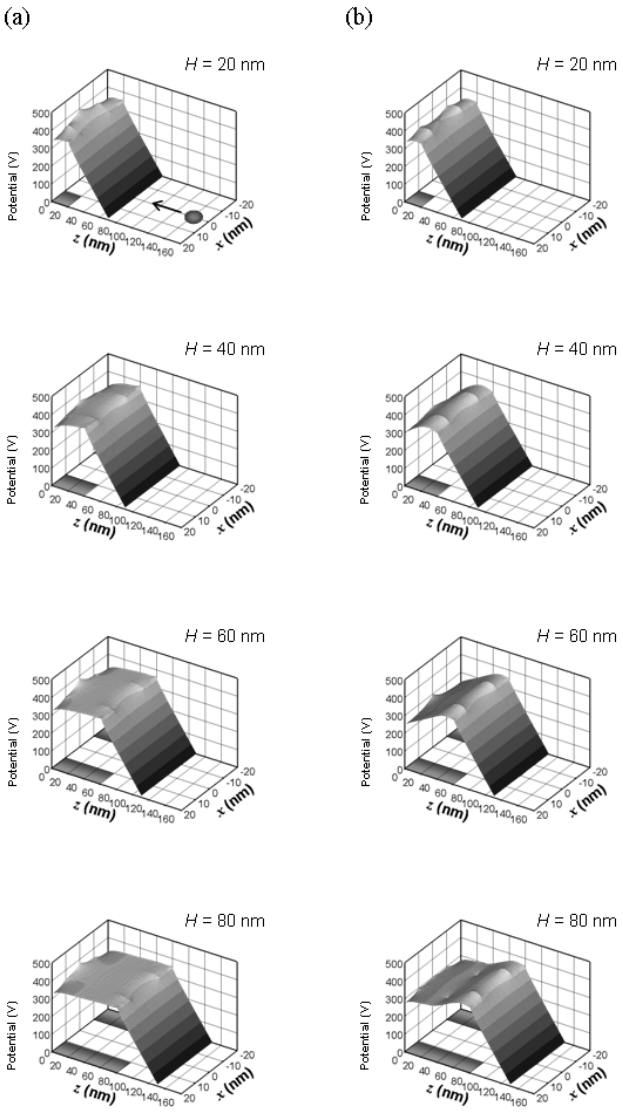

Fig. 4.7: Two-dimensional potential distributions on the *xz* plane from the particle injection boundary to the bottom surface for the (a) hole and (b) trench, calculated the standard condition with different mask heights H = 20, 40, 60, and 80 nm.

Here, a reason why there is potential drop at the bottom in the trench can be shown in Fig. 4.8, which shows normalized flux of positive ions and electron obtained by dividing the bottom flux Γ_B by the top flux Γ_T in the (a) hole and (b) trench, respectively, calculated under the standard condition with different mask heights H = 20, 40, 60, and 80 nm. The normalized fluxes of each ion and electron have a similar trend which decreases for higher mask heights,

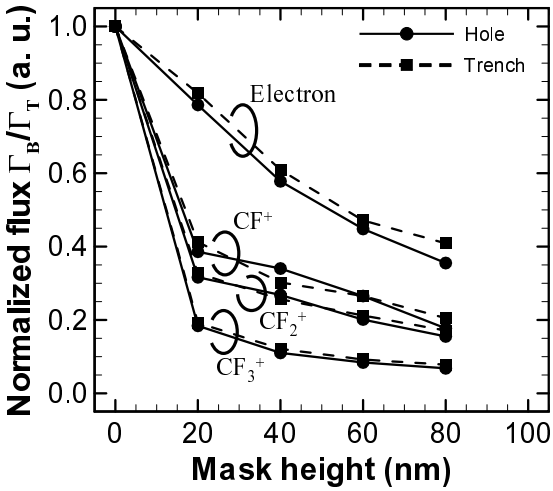

Fig. 4.8: Normalized flux of positive ions and electron obtained by dividing the bottom flux Γ_B by the top flux Γ_T in the (a) hole and (b) trench, calculated under the standard condition with different mask heights H = 20, 40, 60, and 80 nm.

where there is no significant difference between the hole and the trench. In both structures, fluxes of lighter-weight ions are more than those of heavier ions. The main reason is that incident energy of light-weight ions such as CF^+ and CF_2^+ has higher energy peak than that of heavier ions such as CF_2^+ and CF_3^+, respectively, as shown in Fig. 4.4; light-weight ions can easily pass through the potential barrier to the bottom surfaces owing to their own large part of the high energy in the distribution. The normalized flux of electron is higher than that of ions because electrons after passing the rf sheath can easily reach the top and bottom surfaces with support of the potential slope. The normalized flux of electron in the trench are larger than that in the hole because there is less electron shadowing effect in the trench for geometrical reason, indicating that the equilibrium charging density is lower in the trench than in the hole. This is a big possible reason the bottom potentials are lower in the trench than in the hole.

Figures 4.9(a) and 4.9(b) show impact energy distribution functions of CF_3^+ ions and electrons on the bottom surface in the (a) hole and (b) trench, calculated under the standard condition with different mask heights H = 20, 40, 60, and 80 nm. Impact energy distributions of CF_3^+ ion have a peak at 20−40 eV, while those of electron at 340−360 eV in every mask height in the hole. By comparing the distributions with those in Fig. 4.4, CF_3^+ ions lose energy through

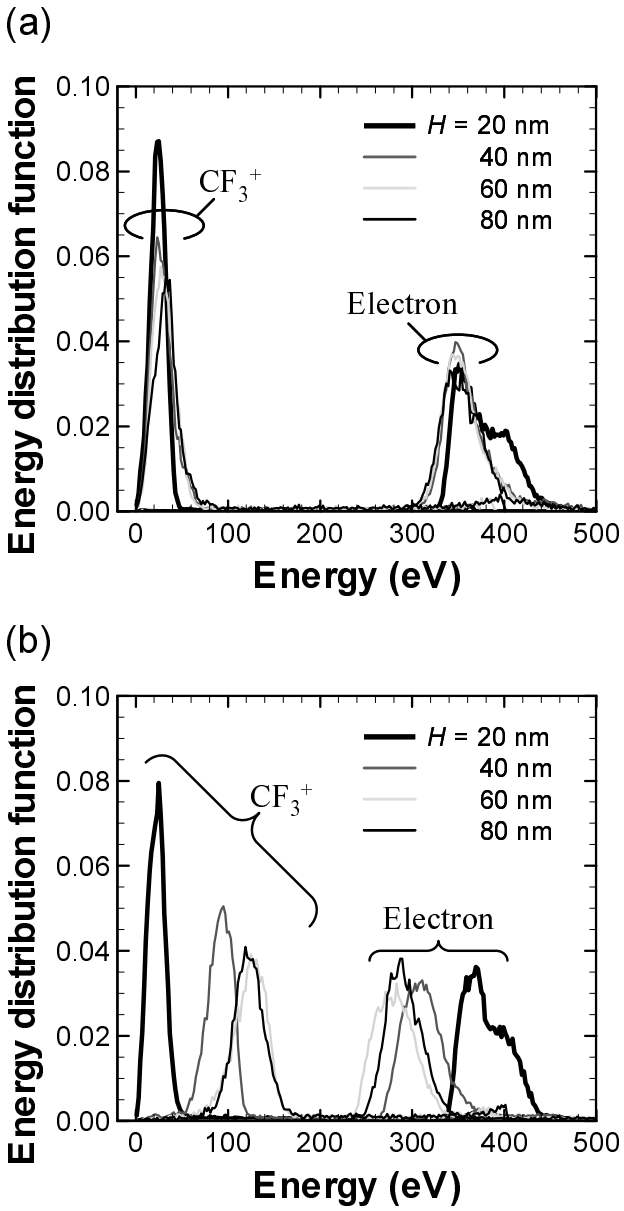

Fig. 4.9: Impact energy distribution functions of CF_3^+ ions and electrons on the bottom surface in the (a) hole and (b) trench, calculated under the standard condition with different mask heights H = 20, 40, 60, and 80 nm.

the potential, while electrons gain energy. On the other hand, in the trench, some energy peaks of CF_3^+ ion and electron are shifted towards each other. The peak shifts are attributed to the potential drop of the bottom in the trench as shown in Fig. 4.7(b).

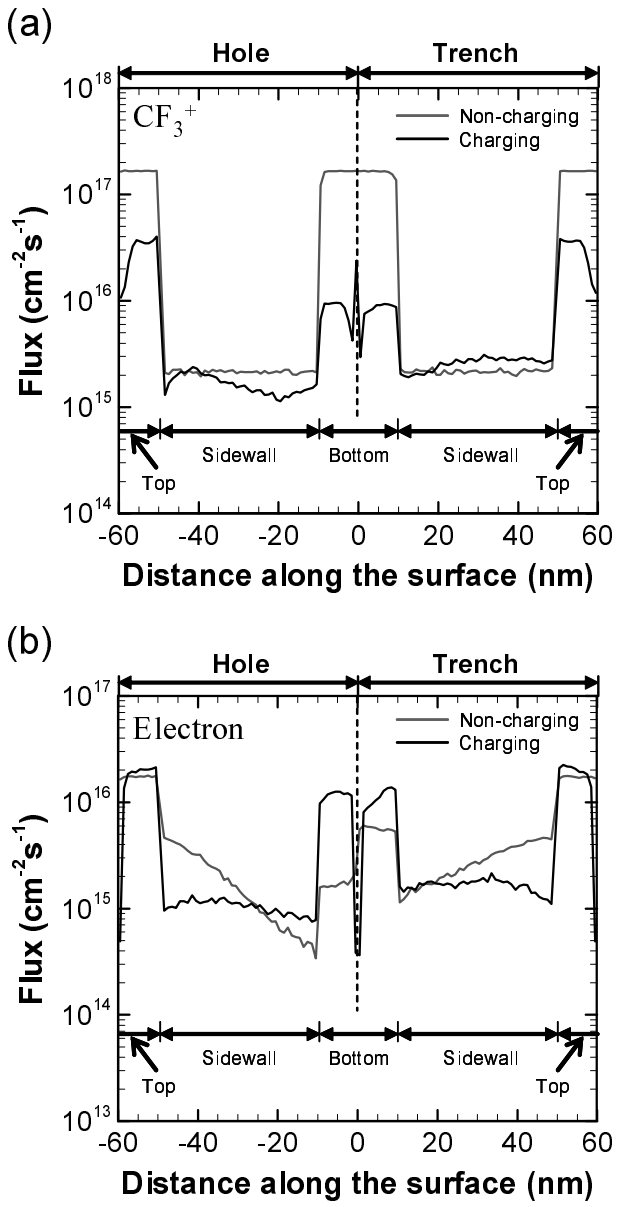

Fig. 4.10: Distributions of fluxes incident to the surfaces of (a) CF_3^+ ion and (b) electron under the charging and non-charging conditions with the mask height $H = 40$ nm, where the left side of the figure indicate fluxes for the hole and the right side for the trench.

Figures 4.10(a) and 4.10(b) show distributions of fluxes incident to the surfaces of (a) CF_3^+

ion and (b) electron under the charging and non-charging conditions with the mask height H = 40 nm, where the left side of the figure indicates fluxes for the hole and the right side for the trench. Both CF_3^+ ion fluxes are almost the same on all surfaces in the hole and trench under the non-charging condition, while the fluxes on the sidewall is higher in the trench than that in the hole under the charging condition. Furthermore, the CF_3^+ ion fluxes in both structures are significantly less under the charging condition than those under the non-charging condition. On the other hand, the electron fluxes have a large difference even in the non-charging condition owing to the geometrical shadowing between the hole and trench. In the charging condition, the electron fluxes on the bottom are almost the same amount between the hole and trench; the electron flux on the sidewall in the trench is still twice more than that in the hole.

4.3.3 Ion trajectory

The trajectories of "cold" CF_3^+ ions of different ion energies E_i = 200, 400, 800 eV after the equilibrium with the mask height H = 40 nm are shown in Figs. 4.11(a) and 4.11(b), for the (a) hole and (b) trench, respectively. All trajectories inside the structure are bend toward the center. Ions in both geometries are impossible to reach the bottom at 200 eV, while they reach the bottom at 800 eV. However, ions at 400 eV are quite different; the trajectories do not reach the bottom but the sidewall in the hole, while they reach the bottom in the trench because the potential drop assists CF_3^+ ions.

Figures 4.12(a) and 4.12(b) show two-dimensional angular distributions of the CF_3^+ ion flux incident to the bottom SiO_2 surfaces for the (a) hole and (b) trench with different mask heights H = 20, 40, 60, 80 nm. The angular distributions of incident CF_3^+ ions onto the bottom have a center peak with a circular- or isotropic-distribution skirt in the hole. However, those in the trench have a narrow distribution in y-axis and a broad distribution in x-axis with two splits. The trend are stronger in the higher mask height. Here, two-dimensional angular distributions of the CF_3^+ ion flux incident to bottom SiO_2 surfaces with different reflection probabilities of 0.1−0.9 on the mask with a height H = 40 nm are shown in Figs. 4.13(a) and 4.13(b) for the (a) hole and (b) trench, respectively. In the trench, distributions at lower reflection probabilities are strongly split. The results indicate that the split distribution are mainly attributed to ions incident directly to the bottom.

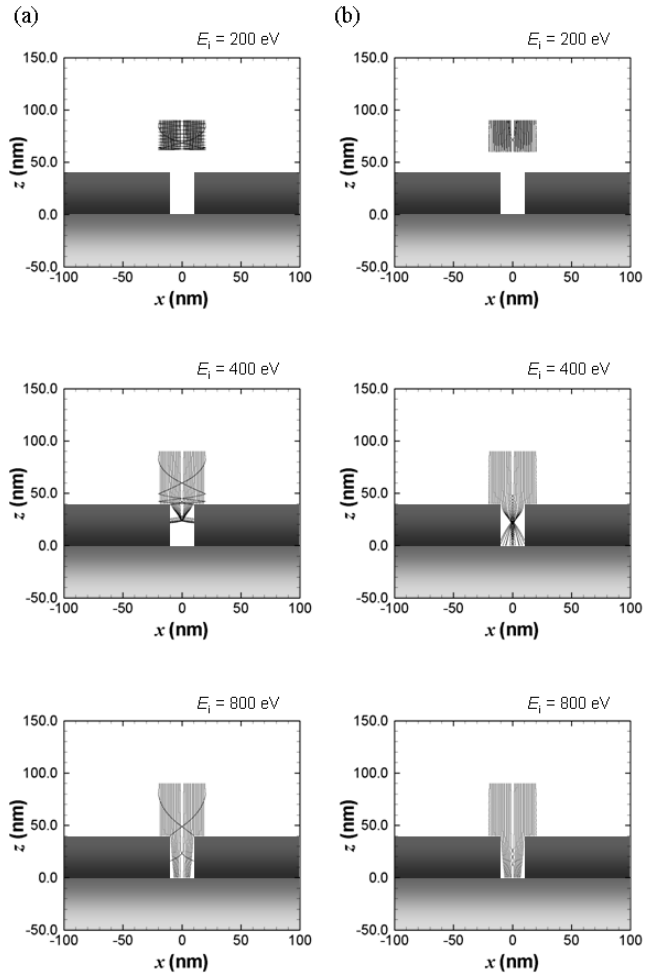

Fig. 4.11: Trajectories of CF_3^+ ions of different ion energies E_i = 200, 400, 800 eV for the (a) hole and (b) trench with the mask height H = 40 nm.

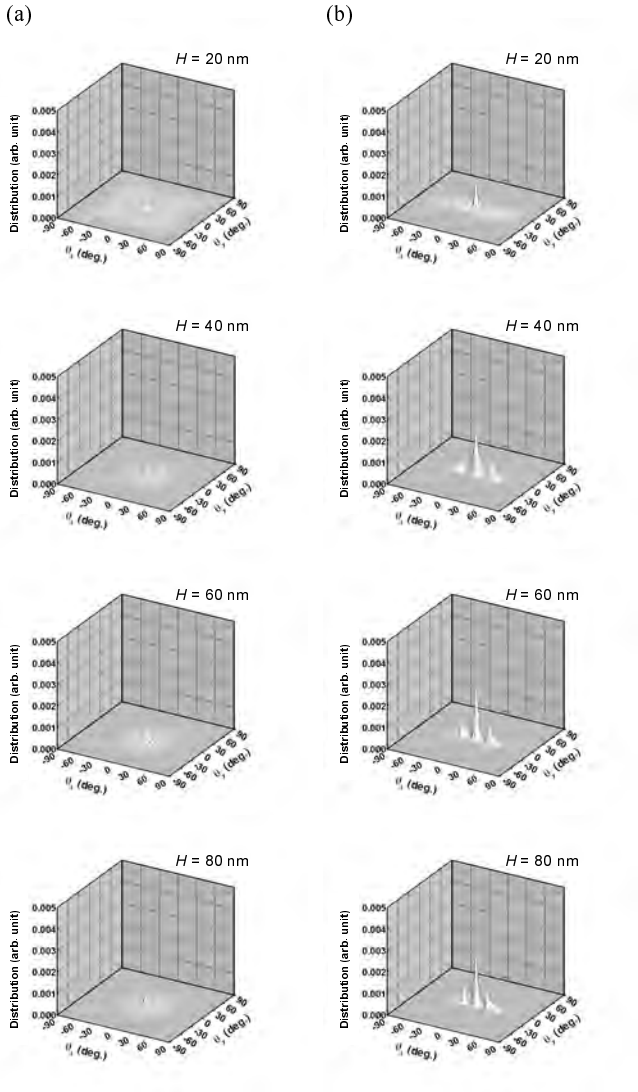

Fig. 4.12: Two-dimensional angular distributions of the CF_3^+ ion flux incident to the bottom SiO_2 surfaces for the (a) hole and (b) trench with different mask heights $H = 20$, 40, 60, 80 nm.

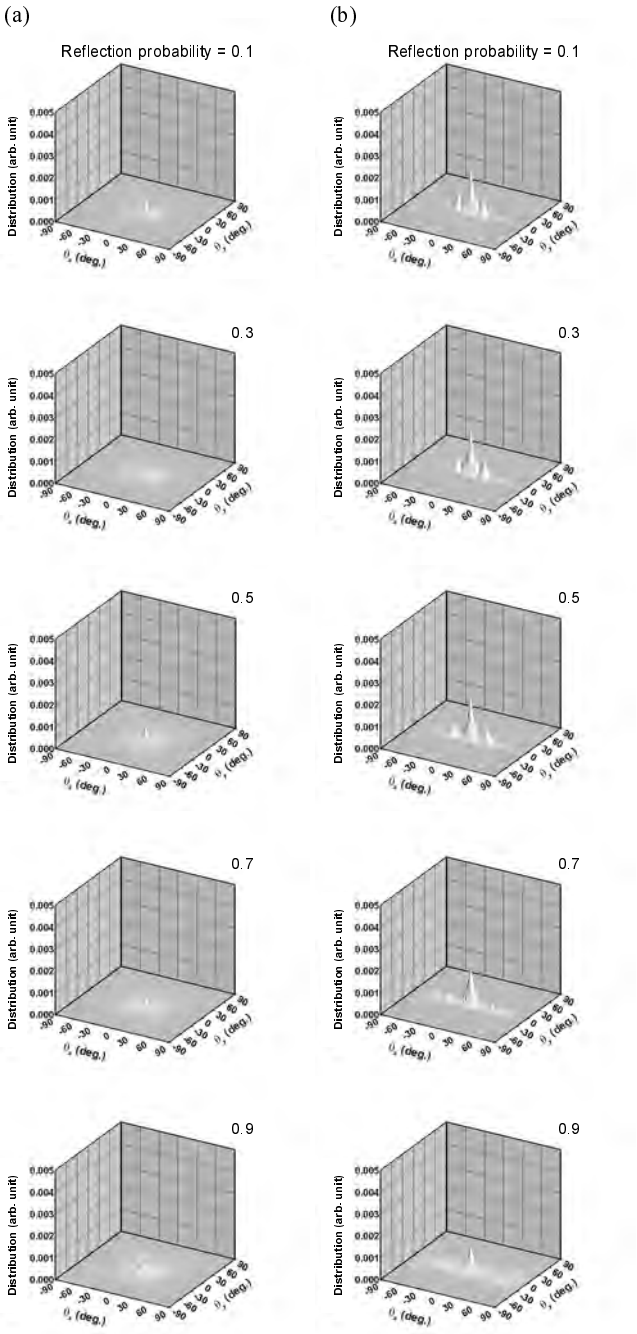

Fig. 4.13: Two-dimensional angular distributions of the CF_3^+ ion flux incident to the bottom SiO_2 surfaces for the (a) hole and (b) trench with different reflection probabilities of 0.1−0.9 at $H = 40$ nm.

4.4 Conclusions

Two-dimensional potential distribution was calculated to investigate the effects of mask pattern geometry on ion and electron fluxes during SiO_2 etching in CF_4 plasmas. The model included the particle transport of ions and electrons through rf sheath, surface kinetics, charge accumulation, and potential calculation for an axisymmetric hole and an infinitely long trench. Charging effects and the resulting potential changed flux of ions and electrons incident to the surfaces. Ion flux incident to the structure bottom were significantly reduced under charging condition compared to the ion flux under the non-charging condition. Moreover, numerical results showed that the difference of potential distribution inside the structure between the hole and trench; the potential drop at the structure bottom was observed in the trench compared to the potential distribution in the hole. The potential difference from mask pattern geometry also changed ion trajectories. The results indicates that etched feature profile is affected by mask pattern geometry.

References

[1] H. Ohtake, B. Jinnai, Y. Suzuki, S. Soda, T. Shimmura, and S. Samukawa: J. Vac. Sci. Technol. A **24** (2006) 2172.

[2] J. Matsui, K. Maeshige, and T. Makabe: J. Phys. D: Appl. Phys. **34** (2001) 2950.

[3] T. Nozawa, T. Kinoshita, T. Nishizuka, A. Narai, T. Inoue, and A. Nakaue: Jpn. J. Appl. Phys. **34** (1995) 2107.

[4] T. Kinoshita, M. Hane, and J. P. Mcvittee: J. Vac. Sci. Technol. B **14** (1996) 560.

[5] H. Ootera, T. Oomori, M. Tuda, and K. Namba: Jpn. J. Appl. Phys. **33** (1994) 4276.

[6] S. Samukawa and T. Mukai: J. Vac. Sci. Technol. B **18** (2000) 166.

[7] P. Berruyer, F. Vinet, H. Feldis, R. Blanc, M. Lerme, Y. Morand, and T. Poiroux: J. Vac. Sci. Technol. A **16** (1998) 1604.

[8] T. Ohiwa, A. Kojima, M. Sekine, and I. Sakai: Jpn. J. Appl. Phys. **37** (1998) 5060.

[9] S. C. McNevin and M. Cerullo: J. Vac. Sci. Technol. A **16** (1998) 1514.

[10] T. Tatsumi, Y. Hikosaka, S. Morishita, M. Matsui, and M. Sekine: J. Vac. Sci. Technol. A **17** (1999) 1562.

[11] A. D. Bailey III and R. A. Gottscho: Jpn. J. Appl. Phys. **34** (1995) 2083.

[12] R. A. Gottscho, C. W. Jurgensen, and D. J. Vitkavage: J. Vac. Sci. Technol. B **10** (1992) 2133.

[13] T. Akimoto, H. Nanbu, and E. Ikawa: J. Vac. Sci. Technol. B **13** (1995) 2390.

[14] M. F. Doemling, N. R. Rueger, and G. S. Oehrlein: Appl. Phys. Lett. **68** (1996) 10.

[15] G. S. Hwang and K. P. Giapis: IEEE Trans. Plasma Sci. **27** (1999) 102.

[16] G. S. Hwang and K. P. Giapis: J. Vac. Sci. Technol. B **15** (1997) 1839.

[17] N. Fujiwara, T. Maruyama, M. Yoneda, K. Tsukamoto, and T. Banjo: Jpn. J. Appl. Phys. **33** (1994) 2164.

[18] K. Hashimoto: Jpn. J. Appl. Phys. **33** (1994) 6013.

[19] J. C. Arnold and H. H. Sawin: J. Appl. Phys. **70** (1991) 5314.

[20] T. Ohmori, T. K. Goto, T. Kitajima, and T. Makabe: Jpn. J. Appl. Phys. **44** (2005) L1105.

[21] S. Sakamori, T. Maruyama, N. Fujiwara, and H. Miyatake: Jpn. J. Appl. Phys. **37** (1998) 2321.

[22] G. S. Hwang and K. P. Giapis: J. Vac. Sci. Technol. B **15** (1997) 70.

[23] K. Hashimoto: Jpn. J. Appl. Phys. **32** (1993) 6109.

[24] G. S. Hwang and K. P. Giapis: J. Appl. Phys. **82** (1997) 566.

[25] A. P. Mahorowala and H. H. Sawin: J. Vac. Sci. Technol. B **20** (2002) 1084.

[26] G. S. Hwang and K. P. Giapis: Appl. Phys. Lett. **71** (1997) 2928.

[27] G. S. Hwang and K. P. Giapis: J. Appl. Phys. **84** (1998) 683.

[28] G. S. Hwang and K. P. Giapis: J. Electrochem. Soc. **144** (1997) L285.

[29] G. S. Hwang and K. P. Giapis: J. Electrochem. Soc. **144** (1997) L320.

[30] G. S. Hwang and K. P. Giapis: Phys. Rev. Lett. **79** (1997) 845.

[31] K. P. Giapis, G. S. Hwang, and O. Joubert: Microelectron. Eng. **61/62** (2002) 835.

[32] H. S. Park, S. J. Kim, Y. Q. Wu, and J. K. Lee: IEEE Trans. Plasma Sci. **31** (2003) 703.

[33] T. Lee, S. S. Kim, Y. S. Jho, G. Park, and C. S. Chang: Phys. Plasmas **14** (2007) 103501.

[34] M. A. Vyvoda, M. Li, and D. B. Graves: J. Vac. Sci. Technol. A **17** (1999) 3293.

[35] J. Matsui, N. Nakano, Z. L. Petrović, and T. Makabe: Appl. Phys. Lett. **78** (2001) 883.

[36] G. S. Hwang and K. P. Giapis: Jpn. J. Appl. Phys. **37** (1998) 2291.

[37] M. Schaepkens and G. S. Oehrlein: Appl. Phys. Lett. **72** (1998) 1293.

[38] G. S. Upadhyaya, J. L. Shohet, and J. B. Kruger: Appl. Phys. Lett. **91** (2007) 182108.

[39] K. H. A. Bogart, F. P. Klemens, M. V. Malyshev, J. I. Colonell, V. M. Donnelly, J. T. C. Lee, and J. M. Lane: J. Vac. Sci. Technol. **18** (2000) 197.

[40] G. S. Hwang and K. P. Giapis: Appl. Phys. Lett. **74** (1999) 932.

[41] S. G. Ingram, J. Appl. Phys. **68** (1990) 500.

[42] K. P. Giapis and G. S. Hwang: Jpn. J. Appl. Phys. **37** (1998) 2281.

[43] G. S. Hwang and K. P. Giapis: Appl. Phys. Lett. **70** (1997) 2377.

[44] H. Fukumoto, I. Fujikake, Y. Takao, K. Eriguchi, and K. Ono: Plasma Sources Sci. Technol. **18** (2009) 045027.

[45] H. Fukumoto, K. Eriguchi, and K. Ono: Jpn. J. Appl. Phys. **48** (2009) 096001.

[46] M. A. Lieberman and A. J. Lichtenberg: *Principles of Plasma Discharges and Materials Processing* (Wiley, 2005, Hoboken, NJ) 2nd ed., p. 37.

[47] D. K. Bhattacharya: Phys. Rev. A **43** (1991) 761.

[48] M. J. Kushner: J. Appl. Phys. **58** (1985) 4024.

[49] G. S. Hwang and K. P. Giapis: Appl. Phys. Lett. **71** (1997) 1942.

[50] E. A. Edelberg, A. Perry, N. Benjamin, and E. S. Aydil: J. Vac. Sci. Technol. A **17** (1999) 506.

[51] S. Takagi, K. Iyanagi, S. Onoue, T. Shinmura, and M. Fujino: Jpn. J. Appl. Phys. **41** (2002) 3947.

Chapter 5

Conclusions

5.1 Concluding remarks

This thesis described analyses of SiO_2 etching in fluorocarbon plasmas. There were two approaches to clarify SiO_2 etching phenomena: a macroscopic plasma gas phase model and a microscopic plasma-surface interaction model. The former or macroscopic model consists of a inductively coupled CF_4 plasma source generated, gas-phase reactions in the chamber, reactions between plasma and substrate surfaces or chamber wall, taking into account transport of ions and radicals. The latter or microscopic model consists of a module of particle transport inside microstructure and a module of surface reactions.

In Chapter 2, a two-dimensional fluid model has been developed to study plasma chemical behavior of etch products as well as reactants during SiO_2 etching by using inductively coupled CF_4 plasmas. The plasma fluid model consisted of Maxwell's equations, continuity equations for neutral and charged species including gas-phase and surface reactions, and an energy balance equation for electrons. The surface reaction model assumed Langumiur adsorption kinetics with the coverage of fluorine atoms, fluorocarbon radicals, and polymers on SiO_2 surfaces. Numerical results indicated that etch product species occupy a significant fraction of reactive ions as well as neutrals in the reactor chamber during etching, which in turn led to a change of plasma and surface chemistry underlying the processing. In practice, the density of SiF_4 was typically about 10% of that of the feedstock CF_4, being comparable to that of the most

abundant fluorocarbon radical CF_2; moreover, the density of SiF_3^+ was typically about 5% of that of the most abundant fluorocarbon ion CF_3^+. The density and the distribution of such product species in the reactor chamber were changed by varying the ion bombardment energy on substrate surfaces, gas pressure, mass flow rate, and coil configuration, which arose in part from gas-phase reactions depending on plasma electron density and temperature. Surface reactions on the chamber walls and on substrate also affected the product density and distribution in the reactor; in particular, the surface reactions on the SiO_2 dielectric window as well as substrate surfaces were found to largely affect the product density and distribution.

In Chapter 3, two-dimensional etching profile evolution in two different geometries, namely an axisymmetric hole and an infinitely long trench, has been simulated with the cellular algorithm, to clarify the effects of geometrically different structures on etching profile evolution. The simulation assumed SiO_2 etching using CF_4 plasmas, owing to the widely employed fluorocarbon plasmas for the fabrication of contact and via holes. Numerical results indicated that the two mask pattern geometries gave some differences in profile evolution, depending on condition parameters such as ion energy, mask pattern size, mask height, and reflection probability on mask surfaces. The profile evolution was slower and more anisotropic in a hole than in a trench; in practice, the profile of a trench tended to have prominent lateral etches such as an undercut and a bowing on sidewalls. Moreover, the reactive ion etching lag was less significant for a hole than for a trench. These differences were ascribed to the geometrical shadowing effects of the structure for neutrals, where the incident flux of neutrals was more significantly reduced in a hole than in a trench. The differences were also attributed to the anisotropy of the velocity distribution of neutrals; in effect, the velocity distribution was more anisotropic in a hole, because more particles interact with mask sidewalls to adsorb or reflect thereon in a hole, so that more anisotropic neutrals were transported onto bottom surfaces after passing mask features.

In Chapter 4, effects of mask pattern geometry on potential distribution and ion trajectories were investigated using surface charge continuity and Poisson's equation. Two geometrical mask patterns of a hole and a trench were considered to clarify the effects of geometrically different structures on potential distribution and ion trajectories. The simulation assumed SiO_2 etching using CF_4 plasmas, owing to the widely employed fluorocarbon plasmas for the fabrication of contact and via holes. Charging effects and the resulting potential changed flux of ions and electrons incident to surfaces. The ion flux incident to the structure bottom were sig-

nificantly reduced under charging condition compared to the ion flux under the non-charging condition. Moreover, numerical results showed that the difference of potential distribution inside the structure between the hole and trench; the potential drop at the structure bottom was observed in the trench, while no significant potential drop was observed in the hole. The potential difference derived from mask pattern geometry also changed ion trajectories. The results indicates that etched feature profile is affected by mask pattern geometry.

5.2 Future work

Summarizing the paper, the author describes the further development of plasma etching model developed in this study. The macroscopic plasma gas phase model and the microscopic microstructure flux model have been developed separately. Development of design and process of semiconductor devises will be promoted faster by integrating the previous two models because input of process parameters bring directly the prediction of process results. Recently, semiconductor devices are increasingly commoditized, while they have been integrated densely and become smarter. In other words, the semiconductor industries are no longer exclusively advanced industries with few foundries. The advanced foundries are required to shorten the development period to avoid price competition with follower foundries. On the other hand, approaches to capture the phenomena involved in plasma etching are academically important, where different scale phenomena must be modeled separately. The gas phase model is required to determine optimum apparatus configurations such as power input position, gas inlet position, and mass flow rate with experimental verification to obtain uniform plasma sources according to growth of wafer size. The process model in microstructures must focus on the existence of atoms and molecules of plasmas and surface materials because process dimensions are approaching atomic scale. Therefore, first principle approach like molecular dynamics will become important rather than an empirical approaches.

In addition, the current society systems manage to save their consumption energy, where there is strong demand for power semiconductors for efficient power distribution and electrification of transportation systems. In the future, research and practical applications of gallium nitride, silicon carbide, and diamond will be actively conducted for replacing silicon semiconductors. Therefore, the development of new plasma sources is required to process the new

alternative semiconductors [1–4].

References

[1] R. J. Trew, J.-B. Yan, and P. M. Mock: Proc. IEEE **79** (1991) 598.

[2] S. J. Pearton, A. Katz, F. Ren, and J. R. Lothian: Electron. Lett. **28** (1992) 822.

[3] J. J. Wang, E. S. Lambers, S. J. Pearton, M. Ostling and C.-M. Zetterling, J. M. Grow, F. Ren, and R. J. Shul: J. Vac. Sci. Technol. A **16** (1998) 2204.

[4] M. Willander, M. Friesel, Q.-U. Wahab, and B. Straumal: J. Mater. Sci.: Mater. Electron. **17** (2006) 1.

List of Publications

Journal publications

1. K. Eriguchi, A. Ohno, D. Hamada, M. Kamei, **H. Fukumoto**, and K. Ono: *"Quantitative Characterization of Plasma-Induced Defect Generation Process in Exposed Thin Si Surface Layers*", Jpn. J. Appl. Phys. **47** (2008) 2446.

2. **H. Fukumoto**, I. Fujikake, Y. Takao, K. Eriguchi, and K. Ono: *"Plasma Chemical Behaviour of Reactants and Reaction Products during Inductively Coupled CF_4 Plasma Etching of SiO_2"*, Plasma Sources Sci. Technol. **18** (2009) 045027.

3. **H. Fukumoto**, K. Eriguchi, and K. Ono: *"Effects of Mask Pattern Geometry on Plasma Etching Profiles*", Jpn. J. Appl. Phys. **48** (2009) 096001.

4. **H. Fukumoto**, K. Eriguchi, Y. Takao, and K. Ono: *"Evolution of Surface Charging during Plasma Etching in Different Mask Pattern Geometries*", (Submitted to Journal of Applied Physics).

International conference publications

1. **H. Fukumoto**, K. Ono, and K. Takahashi: *"Plasma Chemical Behavior of Inductively Coupled Fluorocarbon Plasmas*", Proceedings of 17th International Symposium on Plasma Chemistry (ISPC 17), No. D14, Toronto, Canada, Aug. 2005.

2. **H. Fukumoto**, K. Ono, and K. Eriguchi: *"Modeling of Contact Hole Etching Profile in Two Geometrically Different Ways*", Abstracts of American Vacuum Society 53rd International Symposium & Exhibition (AVS 53), PS2-TuM12, San Francisco, CA, Nov. 2006.

3. K. Eriguchi, K. Nakamura, M. Kamei, D. Hamada, **H. Fukumoto**, and K. Ono: *"A Comprehensive Characterization of the Silicon Substrate Surfaces Damaged by Plasma Processes and the Impacts on Future Scaled Devices*", Abstracts of American Vacuum Society 53rd International Symposium & Exhibition (AVS 53), PS2-TuM13, San Francisco, CA, Nov. 2006.

4. **H. Fukumoto**, K. Eriguchi, and K. Ono: *"Effects of Geometrically Different Microstructures on Etching Profiles*", Proceedings of 18th International Symposium on Plasma Chemistry (ISPC 18), p. 602, Kyoto, Japan, Aug. 2007.

5. M. Kamei, K. Eriguchi, **H. Fukumoto**, and K. Ono: *"Plasma Source-Dependent Charging Damage Polarities in the Performance Degradation of MOSFETs with Hf-based High-k Gate Dielectrics*", Abstracts of American Vacuum Society 54th International Symposium & Exhibition (AVS 54), PS-MoA10, Seattle, WA, Oct. 2007.

6. K. Eriguchi, D. Hamada, M. Kamei, **H. Fukumoto**, and K, Ono: *"Quantitative Characterization of Ions and Si Surface Interactions - Estimation of Plasma-Induced Defect Generation Probability*", Abstracts of American Vacuum Society 54th International Symposium & Exhibition (AVS 54), PS2-WeM5, Seattle, WA, Oct. 2007.

7. **H. Fukumoto**, K. Eriguchi, and K. Ono: *"Geometrical Effects on Etching Profile Evolution*", Abstracts of American Vacuum Society 54th International Symposium & Exhibition (AVS 54), PS1-ThM6, Seattle, WA, Oct. 2007.

8. **H. Fukumoto**, K. Eriguchi, and K. Ono: *"Effects of Etching-Mask Geometry and Charging on Etching Profile Evolution*", Abstracts of American Vacuum Society 55th International Symposium & Exhibition (AVS 55), PS-TuP24, Boston, MA, Oct. 2008.

Domestic conference publications

1. **福本 浩志**, 斧 高一, 高橋 和生: "誘導結合型フルオロカーボンプラズマの解離・再結合特性", プラズマ科学シンポジウム 2005 ／第 22 回プラズマプロセシング研究会 プロシーディングス (PSS-2005/SPP-22), pp. 107-108, Nagoya, Aichi, Jan. 2005.

2. **福本 浩志**, 斧 高一, 高橋 和生: ”誘導結合フルオロカーボンプラズマの気相反応解析”, 第 52 回応用物理学関係連合講演会 講演予稿集, p. 165, Saitama, Saitama, Mar. 2005.

3. **福本 浩志**, 斧 高一, 高橋 和生: ”コンタクトホール内の粒子の挙動とエッチング形状進展のモデル化”, 第 53 回応用物理学関係連合講演会 講演予稿集, p. 187, Tokyo, Tokyo, Mar. 2006.

4. **福本 浩志**, 江利口 浩二, 斧 高一: ”ホールおよびトレンチ側壁へのイオンエネルギーフラックスの解析”, 第 67 回応用物理学会学術講演会 講演予稿集, p. 183, Kusatsu, Shiga, Aug. 2006.

5. **福本 浩志**, 江利口 浩二, 斧 高一: ”ホールおよびトレンチ構造のエッチング形状シミュレーション”, 第 24 回プラズマプロセシング研究会 プロシーディングス (SPP-24), pp. 401-402, Toyonaka, Osaka, Jan. 2007.

6. **福本 浩志**, 江利口 浩二, 斧 高一: ”微細構造内の反応性粒子の挙動とエッチング形状の解析”, 第 54 回応用物理学関係連合講演会 講演予稿集, p. 208, Sagamihara, Kanagawa, Mar. 2007.

7. **福本 浩志**, 江利口 浩二, 斧 高一: ”マスクの形状および表面状態がプラズマエッチングに及ぼす影響”, 第 68 回応用物理学会学術講演会 講演予稿集, p. 198 Sapporo, Hokkaido, Sep. 2007.

8. **福本 浩志**, 江利口 浩二, 斧 高一: ”エッチング形状進展におけるマスクパターン依存性”, 第 25 回プラズマプロセシング研究会 プロシーディングス (SPP-25), pp. 267-268, Yamaguchi, Yamaguchi, Jan. 2008.

9. **福本 浩志**, 江利口 浩二, 斧 高一: ”マスクパターンおよびチャージングがプラズマエッチングに及ぼす影響”, 第 55 回応用物理学関係連合講演会 講演予稿集, p. 234, Funahashi, Chiba, Mar. 2008.